High Temperature Vibration Fatigue Life Prediction and High Strain Rate Material Characterization of Lead-Free Solders

by

Geeta Limaye

A thesis submitted to the Graduate Faculty of
Auburn University
in partial fulfillment of the
requirements for the Degree of
Master of Science

Auburn, Alabama
May 05, 2013

Keywords: Pb-free, Vibration, Fatigue, Innolot, Temperature, High Strain Rate

Approved by

Pradeep Lall, Chair, T. Walter Professor of Mechanical Engineering
Jeffrey Suhling, Quina Distinguished Professor and Chair of Mechanical Engineering
George Flowers, Professor of Mechanical Engineering and Dean of the Graduate School

Abstract

Current trends in the automotive industry warrant a variety of electronics for improved control, safety, efficiency and entertainment. Many of these electronic systems like engine control units, variable valve sensor, crankshaft-camshaft sensors are located under-hood. Electronics installed in under-hood applications are subjected simultaneously to mechanical vibrations and thermal loads. Typical failure modes caused by vibration induced high cycle fatigue include solder fatigue, copper trace or lead fracture. The solder interconnects accrue damage much faster when vibrated at elevated temperatures. Industry migration to lead-free solders has resulted in a proliferation of a wide variety of solder alloy compositions. Presently, the literature on mechanical behavior of lead-free alloys under simultaneous harsh environment of high-temperature vibration is sparse. In this research, a test vehicle representative of an engine control unit has been used. The reduction in stiffness of the PCB with temperature has been demonstrated by measuring the shift in natural frequencies with temperature. The test vehicle has been tested to failure by subjecting it to two elevated temperatures and harmonic vibrations at the corresponding first natural frequency. PCB deflection has been shown to increase with increase in temperature. The full field strain has been extracted using high speed cameras operating at 100,000 fps in conjunction with digital image correlation. Material properties of the PCB at elevated test temperatures have been measured using Dynamic Mechanical Analyzer (DMA).

FE simulation using global-local finite element models is then correlated with the system characteristics such as modal shapes, natural frequencies and displacement amplitudes for every temperature. The solder level stresses have been extracted from the sub-models. Stress amplitude versus cycles to failure curves are obtained at all the three test temperatures. Temperature dependent terms have been added to the Basquin power law to predict the high cycle fatigue life of SAC305 solder at elevated temperatures.

In the second part of the thesis, the effect of aging and high strain rates on a newly developed high-temperature, high-performance lead-free substitute called Innolot by InnoRel^{TM} targeting the automotive electronics segment has been studied. Innolot contains Nickel (Ni), Antimony (Sb) and Bismuth (Bi) in small proportions in addition to Sn, Ag and Cu. Recent studies have highlighted the detrimental effects of isothermal aging on the material properties of SAC alloys. This phenomenon has posed a severe design challenge across the industry and remains a road-block in the migration to Pb-free. This research includes the high strain rate material characterization of Innolot as the alloy ages at an elevated temperature of 50^{0}C. The strain rates chosen are in the range of 1-100 per-second which are typical at second level interconnects subjected to drop-shock and vibration environments. The strain rates and elevated aging temperature have been chosen also to facilitate comparison with tests conducted on SAC105 and SAC305 alloys at CAVE3 by other researchers. Ramberg-Osgood non-linear model parameters have been determined to curve-fit through the experimental data. The parameters have been implemented in Abaqus FE model to obtain full-field stresses which correlates with contours obtained experimentally by Digital Image Correlation (DIC).

Acknowledgments

I would like to express my deep gratitude to my research advisor Professor Pradeep Lall for giving me the opportunity to work under his guidance and mentorship at the NSF Center for Advanced Vehicle and Extreme Environment Electronics (CAVE3) as a Graduate Research Assistant at Auburn University. I would also like to thank my other committee members, Professor George Flowers and Professor Jeffrey Suhling, for their support and guidance while completing this research and thesis.

I would like to thank my parents, Mr. Shrikant Limaye and Dr. Mrs. Lalita Limaye, my elder sister Mukta Limaye, and all my family members for having faith in me and providing endearing love, encouragement and moral support. I gratefully acknowledge the support extended by the following people during my Masters program - Brad Palmer, John Marcell, Sandeep Shantaram, Ryan Lowe, Mahendra Harsha, Kewal Patel, Vikalp Narayan, Kazi Mirza, Shantanu Deshpande, Arjun Angral Mandar Kulkarni and Mayur Golatgaonkar.

Table of Contents

List of Figures

List of Tables

CHAPTER 1

INTRODUCTION

1.1. Overview of Microelectronic Packaging

An integration of several circuits or components on a single chip is defined as an integrated circuit (IC). Packaging is the bridge that interconnects the ICs and other components into a system-level board to form electronic products. It is the portion of an electronic structure that protects an electronic/electrical element and its environment from each other [Ulrich 2006]. Traditionally defined as the back-end-of-the-line process that transforms ICs into functional assemblies, packaging brings together the fundamentals of Mechanical Engineering, Physics and Electronics towards the development of highly functional computing devices. The package must provide a structure to physically support the chip, a housing to protect the chip from the environment, some means to dissipate the heat generated by the system, electrical connections to allow flow of signal and power to and from the chip, and a wiring structure to provide an interconnection between the chips of an electronic system. These four major functions of electronic packaging are illustrated in Figure 1

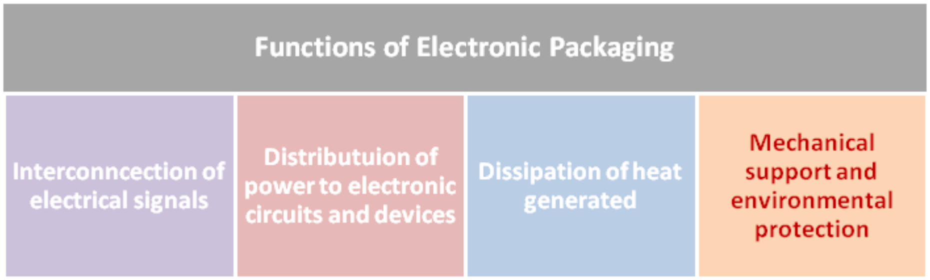

Figure 1: Functions of Electronic Packaging

In addition to the basic functions described above an electronic package must be of high quality, reliable, safe and economical. In order to meet these requirements, a lot of emphasis has been laid on the development and characterization of reliable materials for packaging. Historically, packaging has always been a substantial fraction of the price of an IC (10 to 50%). In general, packaging costs are driven by the materials and fabrication requirements associated with the actual manufacturing and by the testing and rework associated with manufacturability. There are various levels of hierarchy in the packaging of electronic systems as shown in Figure 2. A chip housed in a chip carrier comprises of the first level of packaging. The chip is diced from a wafer of silicon and fabricated using a photolithographic process. Several packages or chip carriers mounted on a printed wire board or substrate constitute the second level of electronic packaging. Edge connectors on PCB which are inserted into back panel contacts form third level of packaging.

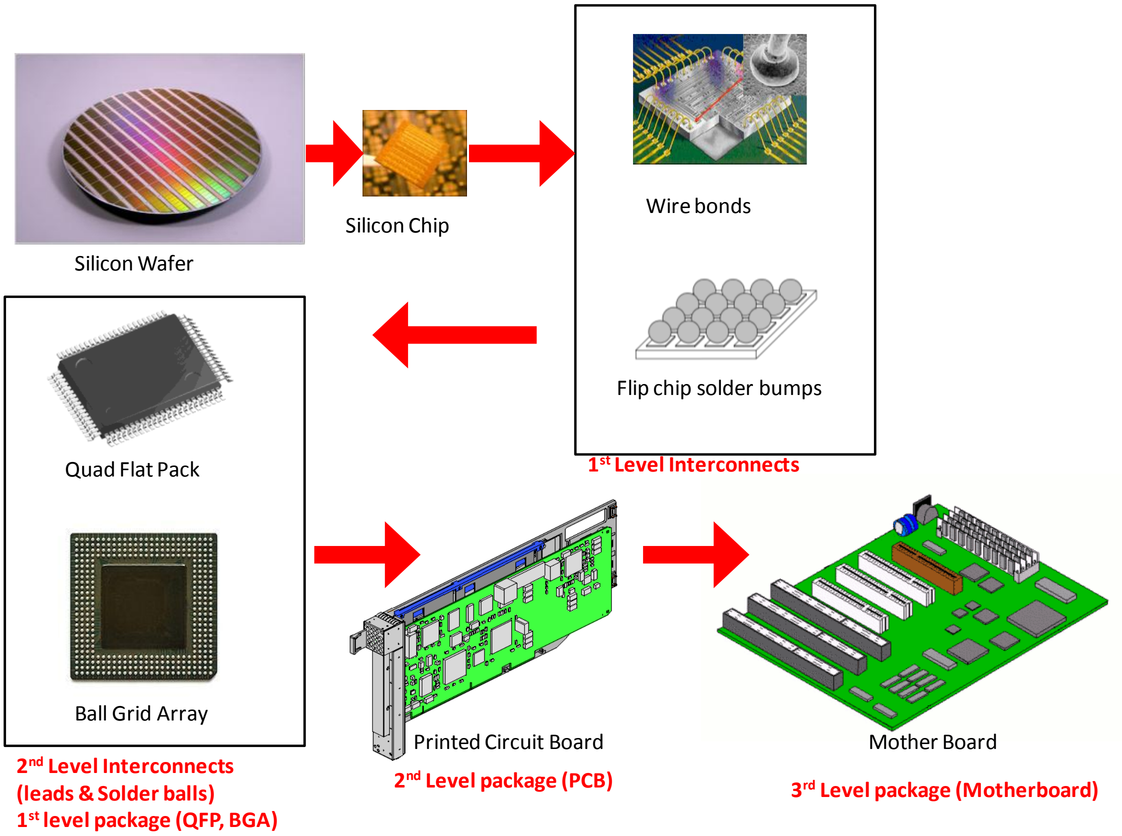

Figure 2: Hierarchy in Packaging of Electronic Systems [Adapted from 'Mechanical Design of Electronic Systems' by Dally, Lall and Suhling 2008]

Electronic Packaging Systems can be broadly classified either on the basis of the technology used for their assembly as:

1) Surface Mount Components

2) Through Hole Components

Alternatively, they can be classified based on the type of package as:

1) Hermetically packaged

2) Plastic encapsulated packages.

The former classification of electronics packaging is the most widely accepted. The through hole technology is more or less obsolete and the surface mount components are the most common packages in the electronics systems of the day.

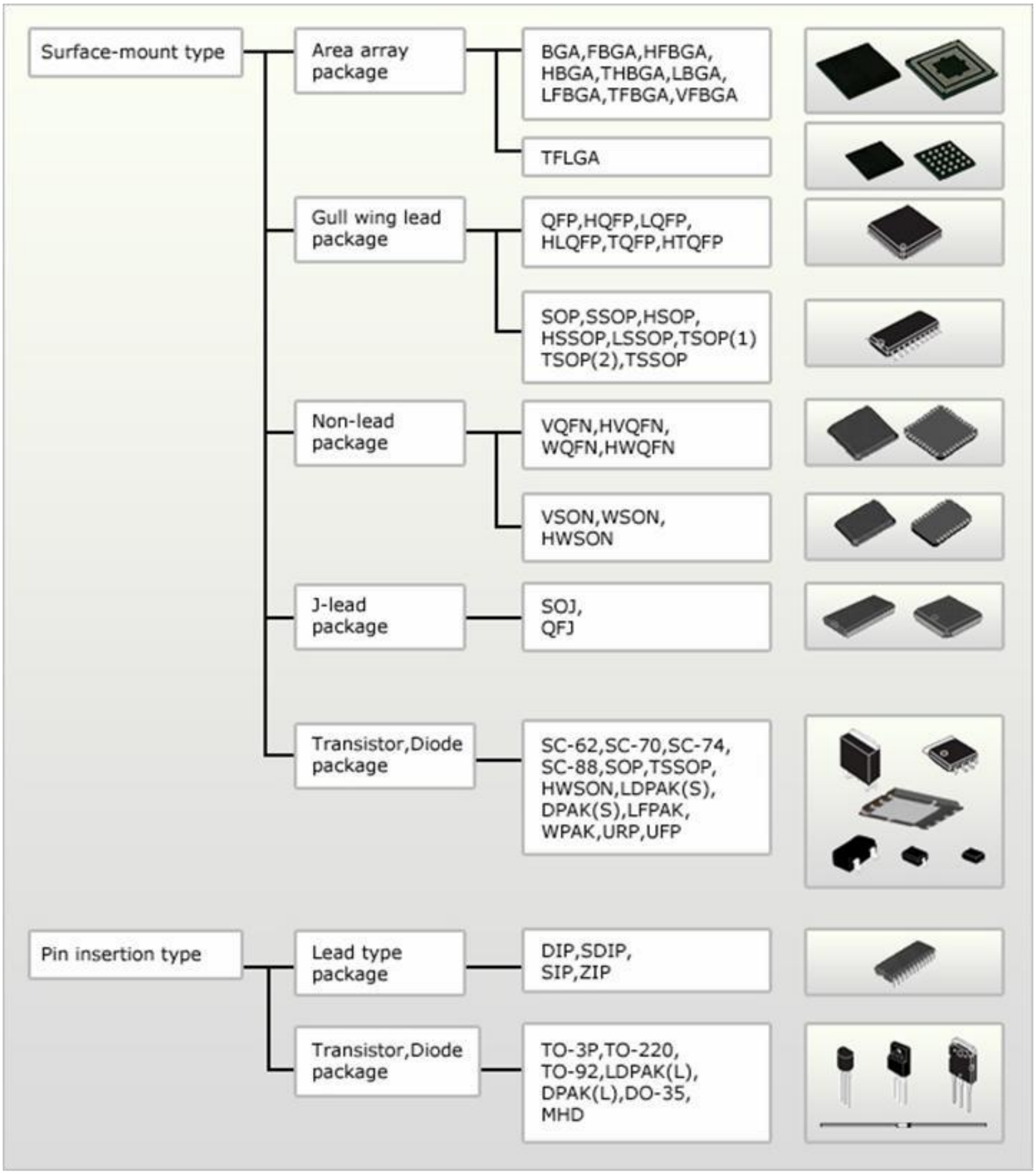

Figure 3: Classification of Electronic Packages [Ref: http://am.renesas.com/products/package/variation/index.jsp]

Driven by the trends towards miniaturization and increased functionality of electronic systems, there is a desire to make smaller and more complex electronic components. With the help of novel upcoming packaging technologies like System-on-Chip (SoC), System-in-Package(SiP), Multi-Chip-Modules (MCM) and 3D packaging technologies like PoP and Stacked-Die components, the complexity of packaging architectures has exponentially increased. With the increase in the interconnect counts and decrease in the pitch between them, the susceptibility to failure has increased. Reliability of electronic packages has therefore gained a lot of significance and is of utmost importance in the highly competitive electronics market. A typical electronic package comprises of different materials that have vastly different material properties [Figure 4]

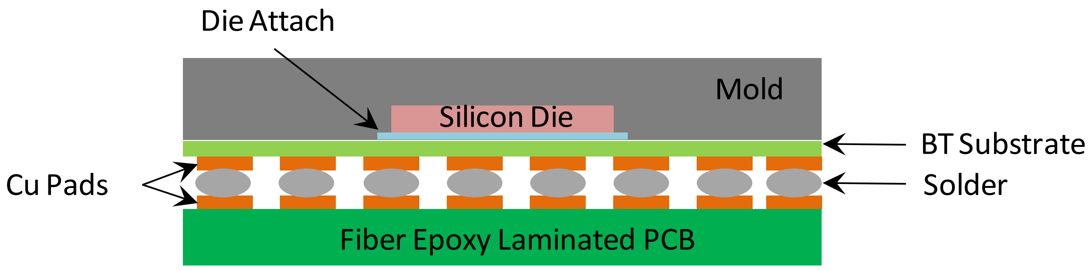

Figure 4: Ball Grid Array Architecture

Table 1: Thermal and mechanical properties of packaging materials

Material	Elastic Modulus (GPa)	Coefficient of Thermal Expansion (CTE) (10^{-6} 1/K)
Mold	23.5	15
Silicon Die	162.7	2.5
Die Attach	6.8	52
Substrate	18	12.4
Solder	30.5	24.5
PCB	17	14.5

For accurate reliability quantification, it is important to have a clear understanding of how all these constituent materials of a component interact with each other during the products operational life. For example, automotive electronic components such as Engine Control Unit (ECU) housed near the engine may experience harsh thermal cycling during their operational life. These extreme thermal conditions lead to severe expansion and contraction of the components. Due to a high degree of mismatch between the coefficients of thermal expansion (CTE) of the constituent materials in a package, high shear stresses will occur at the interface of two materials as one tries to expand and the other resists expansion. This can often lead to delamination between layers and shearing of interconnects.

The field of electronic packaging has been regularly evolving and adapting to meet the ever accelerating demands of the consumer electronics market. Electronic Packaging is development and characterization of reliable materials for packaging and establishment of interconnections between different layers of an electronic component has remained the cornerstone of leading research in electronic packaging for the past few decades. In the light of growing environmental concerns, the Restriction of Hazardous Substances (RoHS) and the Environmental Preservation Agency have created stringent restrictions on the use of leaded solders. Disposed electronics often dumped as land-fills likely to contaminate ground water resources due to the lead content in the solders. Lead-free and halogen-free solder alloy materials in particular have attracted great research attention. Industry migration to lead-free solders has resulted in a proliferation of a wide variety of solder alloy compositions. The most popular amongst these are the Tin-Silver-Copper (Sn-Ag-Cu or SAC) family of alloys like SAC105, SAC305 etc. Recent studies have highlighted the detrimental effects of isothermal aging on the material properties of these alloys. SAC alloys have shown up to 50% reduction in their initial elastic modulus and ultimate tensile strength within a few months of elevated temperature aging. This phenomenon has posed a severe design challenge across the industry and remains a road-block in the migration to Pb-free. Multiple compositions with additives to SAC have been proposed to minimize the effect of aging and creep while maintaining the melting temperatures, strength and cost at par with SAC. But, much waits to be explored as the reliability concerns associated with these novels materials have started to surface.

Electronic systems are present in all walks of life in today’s world. The applications of these systems range from communication, education, entertainment, transportation, research, health care, defense, manufacturing, finance etc. Electronic components thus enable core functionality of the devices that encompass them. With electronic components residing at the heart of most of the mission-critical systems the reliability of these systems has gained tremendous significance. Unlike mechanical constituents, of any system, electrical components generally do not wear out. The failure of electrical systems is often undetectable prior to occurrence. The main reliability concerns associated with electronic components are associated with the following causes:

1. Thermal stresses from exposure to elevated operating temperatures
2. Mechanically stresses from transportation and handling
3. Residual stresses from manufacturing processes
4. Electro-migration, transient static discharge and other electrically induced failures

The solder interconnects are the most likely sites of occurrence of failure in case of thermo-mechanical and mechanical stresses. The primary reason for solders to be the site of failure under thermal stresses is the large CTE mismatch between solder and PCB or substrate. The solder interconnects are also amongst the most vulnerable sections under mechanical loading. As the failure of a solder interconnect can result in an open circuit, the failure of a single solder joint can result in drastic failure of the whole component and the electronic system leading to sudden downtime. Further, the electronics in certain applications like the underhood automotive electronics are simultaneously subjected to thermal and mechanical loads. This thesis researches the reliability of second level solder interconnects under this type of harsh environment.

1.2. Vibration Reliability of Electronics [Steinberg 1998]

Electronic equipments get subjected to various forms of vibrations over their life cycle. The source of vibration can be the association with vibrating machinery during usage or merely vibration loads associated with transportation or handling of the equipment. The form of vibration can range over a wide frequency band and acceleration levels. Many failures can occur due to vibrations and therefore it is necessary to understand the kind of vibration loads and the response of the electronic system to these loads. In automotive applications, the source of vibrations is mainly due to the rough surfaces over which the vehicles are used. In ships, submarines and airplanes, water buffeting and air buffeting as well as the engines are the main causes of vibration. In missiles in subsonic flight, the sound field developed by the rocket causes vibrations.

Electronic systems commonly make use of Printed Circuit Boards (PCB) which can easily be plugged in to or removed from modular type assemblies for service and replacement. There is a variety of PCB material and manufacturing processes in the industry. The most extensive are the PCBs made out of fiber glass reinforced epoxy with laminated layers of copper to form electrical conductors. PCB thickness varies from 0.006 inch to 0.125 inch and the typical form factor in automotive application is rectangular. PCBs that have high power dissipating components, are often bonded to copper or aluminum heat sinks. The heat sink can be cast integrated with ribs that protect the PCB from severe vibration and shock. Ribs increase the stiffness of the circuit board and hence the resonant frequency. This reduces the PCB deflections and consequent component level stresses. Ribs can be made of aluminum, steel or epoxy fiberglass. Screws or quick release clamps are used to install the circuit boards onto modular assemblies. The way in which PCB is supported is an important factor that determines its response to the vibrations. A system subjected to severe vibrations and shock should not have a loose fit even if it eases the connector engagement. This is because a loose circuit board will develop high acceleration and loads which will lead to deflections and stresses in the components of the PCB. Board edges are supported with guides made of beryllium copper or molded plastics. The grip of such guides prevents the rotation or translation of edges which increases the natural frequency of the board. A firm grip causes dissipation of energy due to vibration in the form of friction loss thus reducing the transmissibility of the PCB under resonant conditions. Other factors that affect the board transmissibility include board material, number and type of laminations, natural frequency, type of mounting, types of components on the board, acceleration levels, conformal coating, connectors and shape of board. When more energy is dissipated in the form of heat then there is less energy remaining and the transmissibility is lower. For rectangular PCB, the transmissibility will normally range from 0.5 to 2.0 times the square root of natural frequency. For resonant conditions, the dynamic bending stresses in a uniformly loaded circuit board can be determined by considering a sinusoidal load variation in the over the board surface when the edges are simply supported. This follows from the relative dynamic deflections which will be maximum at the center and zero at the edges. Sinusoidal vibrations often arise from rotating or oscillating machinery like engines, gears, wheels, motors etc. Sinusoidal vibrations are very useful for diagnostic purposes to evaluate the dynamic characteristics of electronic equipments like examining the resonant frequency, damping etc. The approximate fatigue life of a vibrating system can often be estimated from the fatigue characteristics of the various members that carry the major structural loads. These fatigue properties are usually obtained from controlled stress cycle tests performed on many parts that have been manufactured from the same material, with close dimensional tolerances. These parts are stress tested to failure, then the data points are plotted on log-log paper, with stress on the vertical axis and number of cycles to failure on the horizontal axis. A straight line that represents the best average material properties is drawn through the scattered data points. The equation for the sloped portion of the curve can be expressed as follows [Steinberg 1998]:

$$N_1S_1^b=N_2S_2^b \tag{1}$$

where N = number of stress cycles to produce fatigue failure

S = Stress level at which these failures occurred

b = Fatigue exponent related to the slope of the line

The exponent b is related to the fatigue life of the structure, and it is useful in predicting the fatigue life of other structures fabricated of the same material and exposed to the similar environments. In order to reflect the real structural properties of these materials, a stress concentration factor K must be included in the evaluation of exponent b. A typical stress concentration factor for an electronic box structure for a PCB within the box is about 2. For linear systems, the fatigue cycles will be directly related to time, so the time T can be used to replace the number of cycles (N). Also, the stress S will be directly related to the acceleration G and to the displacement Z. The dynamic can also be included if desired. These relations can be written as follows: [Steinberg 1998]

$$T_1G_1^b=T_2G_2^b \tag{2}$$

$$N_1G_1^b=T_2G_2^b \tag{3}$$

$$N_1Z_1^b=N_2Z_2^b \tag{4}$$

The components mounted on electronic systems that are used in a vibration and shock environment often experience amplified or attenuated levels of vibrations depending the dynamic characteristics of the system. The resonant frequencies of PCB may get excited and cause it to bend back and forth. The component level stresses depend on the geometry of the second level interconnects.

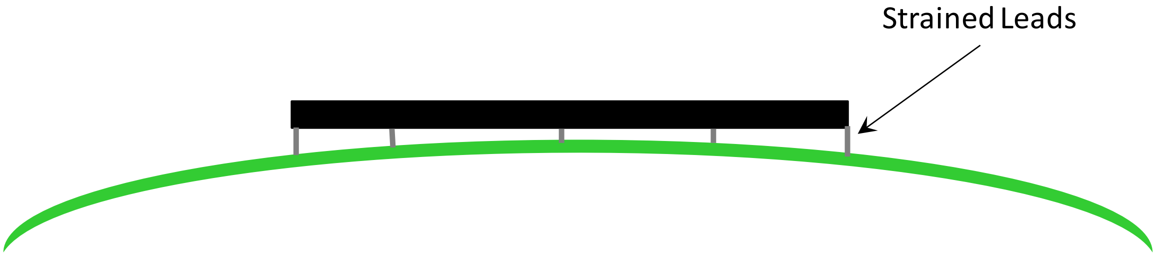

Figure 5: Lead strains due to relative motion between component and circuit board

For leaded packages, for a particular environment and particular PCB resonant frequency, the stresses on solder interconnects can be reduced by reducing the spring rate of the lead wires. This appears contradictory to the usual approach, where the failure of structure is prevented by making the structure more stiff. It can be explained as follows:

$$F=kx \tag{5}$$

Where F is the force, k is the stiffness and x is the displacement. If the displacement is constant, the only way to reduce the force can be reduced is by reducing k. This is the same condition that exists in the component lead wires for a specific dynamic displacement generated by the resonant frequency and acceleration level. Under resonant conditions, the stiffness of the lead wires that bend back and forth can be related to the following parameters: [Steinberg 1998]

$$K_{wire} = EI/L^3 \tag{6}$$

This shows that to reduce the stiffness of the lead wire, the length has to be increased. When the wire length is doubled, the stiffness will reduce by a factor of 1/8 due to the inverse cubic relation. Likewise, the moment of inertia can be reduced to reduce the stiffness. This can be achieved by reducing the height or thickness of the lead wire. Coining the lead wire, i.e squeezing it into a flat metal strip reduces the thickness without changing the cross-sectional area. Thus the stiffness, force and stress in the lead wire can be reduced. In lead-less components like Ball Grid Arrays (BGA), the above relation applies to the shear stiffness of the solder that bonds the component to the PCB. The stiffness in this case can be expressed as: [Steinberg 1998]

$$K_{\text{shear, solder}} = AG/L \tag{7}$$

where A = cross-sectional area of the solder in in^2

L=height of solder joint

G=shear modulus of the solder.

The shear stiffness can be decreased by reducing the cross-sectional area, reducing the shear modulus or increasing the height of the solder joint. In Steinberg's work based on sinusoidal vibrations of a single component PCB, the fatigue life of 10 million stress reversal cycles can be achieved if the peak single amplitude displacement of the PCB is limited to the value below: [Steinberg 1998]

$$Z = \frac{0.00022B}{Chr\sqrt{L}} \tag{8}$$

where B=length of PCB edge parallel to component , in

L=length of electronic component, in

h=height or thickness of PCB, in

C=constant for different types of components

r=relative position factor for components

The peak single-amplitude displacement expected at the center of a PCB can be estimated by assuming the PCB acts like a single-degree of freedom system at its resonant condition, [Steinberg 1998]

$$Z = \frac{9.8G}{f_n^2} = \frac{9.8G_{in}Q}{f_n^2} \tag{9}$$

The displacement value obtained from the above relation will be little less than the correct value obtained from the actual dimensions of the PCB plate geometry. Since PCB is approximated as a single degree of freedom system, the displacement will be of the centroid of PCB and not of the PCB itself.

The size, location and orientation of a component on the PCB are important factors that affect the life of the component. The most critical location for large components is the center of PCB where the displacements are maximum. The curvature reduces as the component moves away from the center. This reduces the forces and stresses on solder joints.

In automotive applications, a combined harsh environment of high temperature and vibrations is prevalent at many locations. Current trends in the automotive electronics industry warrant the use of several electronic systems for safety, enhanced operator control and fuel efficiency and passenger entertainment. These include engine control units, crank-shaft / cam-shaft sensors, wheel speed sensors, exhaust gas sensors, cylinder pressure sensors, combustion sensors etc which are located underhood. The desire to place engine control units on the engine and transmission control units either on or in the transmission has pushed the ambient temperature above 125°C. High-temperature electronics used in automotive systems continue to grow, as fast as the cost and reliability issues are addressed. In the near future, hybrid electric vehicles and fuel cell vehicles will drive the demand for higher temperature power electronics. In the case of hybrid electric and fuel cell vehicles, the high temperature will be due to power dissipation. The use of lead (Pb) in solders for electronic connections is now extensively restricted in Europe, with its use likely to be phased out completely in the medium term. Although Pbfree solders have been the subject of much research, little investigation has been carried out into their reliability for applications exposed to vibration in service. Aerospace applications, which have service lives measured in decades, are of particular pertinence. The present work shows the development and validation of a method for testing small, model solder joints in high-cycle fatigue. The tests are conducted using common equipment yet provide fast results and objective comparisons between solders without the influence of PCBs or components, which typically obscure the solders' intrinsic contribution. S-N diagrams are presented which compare the performance of traditional Sn-Pb solder to that of Pb-free alloys at room and high temperatures and with copper and nickel substrates. It is found that in all situations the Pb-free alloys offer lower lifetimes to failure than the traditional Sn-Pb, an unexpected result when considering the inferior mechanical properties of the latter. The large disparity at room temperatures and with copper substrates is significantly reduced by elevated temperatures and by soldering to nickel substrates. In order to investigate these results, a number of techniques are employed. In addition to extensive fractography, the damping capacity of the solders is investigated and a scanning acoustic microscope is used in conjunction with resonant decay tracking of specimens to study the crack propagation paths prior to complete failure. The analysis of results focuses on the possible causes for this performance difference, drawing on existing soldering literature and wider engineering principles. It is concluded that the overall pattern of results presents contradictory evidence for the contribution of various factors, such as yield strength or interfacial adhesion, which are hard to reconcile. It is thought likely that more numerous fatigue initiation sites in the Pb-free alloys are responsible to some degree for their lower cycles to failure, although more research into the effect of substrate and interfacial intermetallics is necessary to determine the mechanism by which these influence the results, in the absence of relevant fractographic evidence.

1.3. FEA Procedures for Vibration Analysis [Abaqus 6.10 Documentation]

It is essential to be able to numerically extract the the eigenvalues and modes of an electronic system subjected to vibrations in order to evaluate the response of that system to the possible vibration loads. There are several response evaluation methods that are computationally inexpensive and provide useful insight into the structure's dynamic behavior. Some of these methods provided in Abaqus/Standard and are described in this section. The eigenvalue problem for natural modes of small vibration of a finite element model is: [Abaqus 6.10 Theory Manual, Modal Dynamic Analysis]

$$\left(\mu^2[M] + \mu[C] + [K]\right)\{\phi\} = 0 \tag{10}$$

where [M] is the mass matrix which is symmetric and positive definite in the problems of interest here [C] is the damping matrix, [K] is the stiffness matrix, which may or may not be positive definite or symmetric, μ is the eigenvalue and ϕ is the eigenvector or the mode of vibration. The eigenvalues and eigenvectors of a system can be real or complex. But if [K] is assumed to be symmetric and [C] is neglected during the frequency extraction step, the system will have real squared eigenvalues μ^2 and real eigenvectors only. For such symmetric eigenproblems, [K] is also assumed to be positive semidefinite. In this case μ becomes an imaginary eigenvalue, μ=iω where ω is the circular frequency, and the eigenvalue problem can be written as: [Abaqus 6.10 Theory Manual, Modal Dynamic Analysis]

$$-\left(\omega^2[M]+[K]\right)\{\phi\}=0 \tag{11}$$

Lanczos eigensolver is a powerful method to solve this symmetrized eigenvalue problem. The Lanczos procedure in Abaqus/Standard consists of a set of Lanczos "runs," in each of which a set of iterations called steps is performed. For each Lanczos run the following spectral transformation is applied: [Abaqus 6.10 Theory Manual, Modal Dynamic Analysis]

$$[M]\left(-\sigma[M]+[K]\right)^{-1}[M]\{\phi\}=\theta[M]\{\phi\} \tag{12}$$

where σ is the shift, θ is the eigenvalue and ϕ is the eigenvector. This transformation allows rapid convergence to the desired eigenvalues. The eigenvectors of the symmtrized problem and the transformed problem are identical, while the eigenvalues of the original problem and the transformed problem are related in the following manner: [Abaqus 6.10 Theory Manual, Modal Dynamic Analysis]

$$\omega^2=\frac{1}{\theta}+\sigma \tag{13}$$

A Lanczos run will be terminated when its continuation is estimated to be inefficient. Followed by the frequency extraction procedure, is the modal dynamic analysis procedure. This procedure provides time history analysis of linear systems. The excitation to the system is input as a function of time by defining an amplitude curve. It is assumed that in between two points specified in the amplitude curve, the magnitude of excitation varies linearly. When the model is projected onto the eigenmodes used for its dynamic representation, the following set of equations at time t are obtained: [Abaqus 6.10 Theory Manual, Modal Dynamic Analysis]

$$\ddot{q}_{\beta} + C_{\beta\alpha}\,\dot{q}_{\alpha} + \omega^{2} q_{\beta} = (f_{t})_{\beta} = f_{t-\Delta t} + \frac{\Delta f}{\Delta t}\Delta t \qquad (14)$$

where α and β indices span the eigenspace, $C_{\alpha\beta}$ is the projected viscous damping matix, q_{β} is the generalized coordinate of mode β (the amplitude of the response in this mode), $\omega_{\beta} = \sqrt{k_{\beta}/m_{\beta}}$ is the natural frequency of the undamped mode β (obtained as the square root of the eigenvalue in the eigenfrequency step that precedes the modal dynamic time history analysis), $(f_{t})_{\beta}$ is the magnitude of the loading projected onto this mode (the "generalized load" for the mode) and Δf is the change in f over the time increment Δt. If the projected damping matrix is diagonal, this equation becomes the following uncoupled set of equations: [Abaqus 6.10 Theory Manual, Modal Dynamic Analysis]

$$\ddot{q}_{\beta} + 2\xi_{\beta} C_{\beta\alpha}\omega_{\beta}\,\dot{q}_{\beta} + \omega_{\beta}^{2} q_{\beta} = (f_{t})_{\beta} \qquad (15)$$

where ξ_{β} is the critical damping ratio given by the relation [Abaqus 6.10 Theory Manual, Modal Dynamic Analysis]:

$$2\xi_\beta \omega_\beta = \frac{c_\beta}{m_\beta} \qquad (16)$$

where c_β is the modal viscous damping coefficient and m_β is the modal mass in mode β. The solution to the uncoupled equations is obtained readily as a particular integral for the loading and a solution to the homogeneous equation (with no right-hand side). These solutions can be combined and written in the general form: [Abaqus 6.10 Theory Manual, Modal Dynamic Analysis]

$$\begin{Bmatrix} q_{t+\Delta t} \\ \dot{q}_{t+\Delta t} \end{Bmatrix} = \begin{bmatrix} a_{11} & a_{12} \\ a_{21} & a_{22} \end{bmatrix} \begin{Bmatrix} q_t \\ \dot{q}_t \end{Bmatrix} + \begin{bmatrix} b_{11} & b_{12} \\ b_{21} & b_{22} \end{bmatrix} \begin{Bmatrix} f_t \\ f_{t+\Delta t} \end{Bmatrix} \qquad (17)$$

where a_{ij} and b_{ij} are constants, since it is assumed that the loading only varies linearly over the time increment (that is Δf/Δt is constant). Depending on whether the damping in the modal equilibrium equation is greater than, equal to, or less than critical damping this equation is solved using the corresponding a_{ij} and $b_{ij.}$

1.4. Effect of High Temperature on the Reliability of Electronics [Lall 1997]

Reliability is the ability of a system to perform and maintain its functions under normal usage conditions as well as corner conditions. Reliability failures occur due to damage caused by internal or external stresses. Most of the times, one failure mechanism dominates leading to the failure of the system. Failure mechaniscm may be initialted due to operating conditions outside the prescribed specifications. Steady state temperature, temperature cycles, temperature gradients and time-dependent temperature changes all have the potential to affect the reliability of modern electronic devices and equipments [Lall 1997]. Current methodologies in reliability prediction under the influence of temperature are derived from the activation energy based models proposed by Savante Arrhenius in which the steady state temperature dependence of the rate of chemical reaction was described in the form: [Lall 1997]

$$r_r = r_{r-ref} \times e^{-E_{a-chrt}/K_B T} \tag{18}$$

where r_r is the reaction rate (moles/meter^{2}second), $r_{r\text{-}ref}$ is the reaction rate at a reference temperature (moles/meter^{2}second), $E_{a\text{-}chrt}$ is the activation energy of the chemical reaction (eV), K_B is the Boltzmann's constant (8.617 x 10-5 eV/K) and T is the steady-state temperature (Kelvin). This model has been reformulated to predict the influence of steady state temperature on electronic device reliability. In this case, the MTF (hours), for a given steady state temperature is represented as: [Lall 1997]

$$MTF = MTF_{ref} \times e^{-E_{a-dev}/K_B T} \tag{19}$$

where MTF_{ref} is the mean time to failure at a specified reference temperature and $E_{a\text{-}dev}$ is the device activation energy (eV). Often implicit in the test strategy is the assumption that the failure mechanism active at higher temperatures are also active in the equipment operating range, and that the Arrehenius relationship holds.

1.5. Thesis Layout

This thesis presents the characterization of Pb-free solder alloys under various harsh environments that are particularly prevalent in the automotive electronics. The aim of this research is to develop a methodology to characterize the high cycle fatigue life of solders subjected to high temperature and vibrations. Using a combination of experimental and FE based numerical methods, the S-N curve characterizing the high cycle fatigue life of SAC305 solder alloy has been obtained at various temperatures. Temperature dependent terms have been introduced in the Basquin Power law based fatigue life estimation for SAC305. It has been shown that the fatigue life of SAC305 decreases as the temperature increases. Further, this research explores the fundamental material properties like the Elastic modulus and Ultimate Tensile strength of a newly developed Pb-free solder alloy called Innolot. This alloy has been developed targeting the automotive industry and is designed to resist the detrimental effects of exposure to elevated temperatures. In this study, the effect of elevated temperature aging and high strain rates has been studied on the material properties of Innolot and a comparison with SAC105 and SAC305 solders has been presented.

Chapter 2 presents literature survey on solder material characterization. Experimental and FE based methods used in studying the reliability of electronic packaging subjected to vibrations by prior researchers has been covered in this chapter. A major portion of this work deals with reliability of second level interconnects. This chapter highlights the state of art work that has been conducted by researchers till date in order to differentiate the work presented in this thesis. Board level reliability studies carried out on test vehicles have been emphasized. Previous work pertaining to the vibration for leaded and lead-free alloys has been presented. The later part of the literature review covers the work done by researchers in the field of investigation of solder constitutive behavior. The research on effect of isothermal aging, strain rates and solder alloy composition on the mechanical properties of Pb-free solders has been given special emphasis. This highlights the uniqueness of the research covered in the later part of the thesis pertaining to the study of constitutive behavior of Innolot and the effects of high strain rate and isothermal aging on its constitutive behavior.

Chapter 3 presents a methodology development to evaluate the characteristic high cycle fatigue life S-N curve of solder at various test temperatures. The automotive harsh environment of high temperature and vibration levels has been simulated in the laboratory by mounting an isothermal chamber on the existing electrodynamic shaker. The chapter contains a detailed description of the test set-up, test vehicle and test cases used for this study. Further, the FE based simulation techniques and the correlation obtained with the experimental results have been covered. SAC305 high cycle fatigue characterization based on the Basquin Power law (S-N curve) is illustrated for every test temperature. The temperature dependence of the fatigue strength coefficient and the fatigue exponent has been evaluated and implemented in the power law. Thus the last section of this chapter presents a modified equation relating the SAC305 solder stress amplitude and the fatigue life at a given temperature.

In the next chapter, Chapter 4, the constitutive behavior of a newly developed Pb-free substitute for high temperature and high performance applications has been evaluated. This alloys is called Innolot and is developed InnoRel^{TM} targeting the automotive electronics segment. Innolot contains Nickel (Ni), Antimony (Sb) and Bismuth (Bi) in small proportions in addition to Sn, Ag and Cu. It is reported to perform better in thermal cycling as compared to the SAC alloys. In this research a novel test equipment capable of testing the solder material properties in the strain rate range of 1-100 per second has been used to evaluate the constitutive behavior of Innolot. Further the effect of elevated temperature isothermal aging on the constitutive behavior of Innolot has been studied. Finally a comparison of Innlot with SAC105 and SAC305 alloys conducted by other researchers has been presented. The last Chapter 5 summarizes the purpose and findings of the thesis and briefly discussed the scope for future work.

CHAPTER 2

LITERATURE REVIEW

2.1. Vibration Analysis of Electronics

Electronic components in automotive applications get exposed simultaneously to high temperature and dynamic loads during their life cycles. Studies on automotive temperature extremes have recorded continuous maximum temperatures upto 140C and vibration level up to 10G RMS [Johnson et. al. 2004]. The significance of studying reliability under this type of environment is even more consequential for off-road automotives like construction and agricultural machinery. Both high temperature and vibrations contribute to the failures in such system [Barker et. al. 1990, 1992, Basaran et. al. 2002, Qi et. al. 2004]. The reliability of electronic products can be improved through a thorough understanding of the weakest link in the electronic systems which is the solder interconnects. There is a lack of fundamental understanding of reliability of electronic systems subjected to extended period of vibrations at elevated temperature. Most of the research is focused on reliability of solder interconnects subjected exclusively to vibrations [Steinberg 1988, Henderson et. al. 1995, Hu et. al. 1995, Wong et. al. 1997, Lall et. al. 2005, Lall et. al. 2007] or thermal cycling. Relatively few researchers have studied the reliability in the simultaneous environment of thermal cycling and vibration [Barker et. al. 1990, 1992, Basaran et. al. 2002, Qi et. al. 2004]. In this paper, the authors have characterized the high cycle fatigue S-N curves of lead-free solder at various constant temperatures.

Most of the prior research in the area of reliability of solder joints is focused on thermal cycling which includes low cycle fatigue failure modes. Researchers have developed the theory and life prediction models for solder fatigue subjected to thermal cycling [Tavernelli 1962]. Similarly, the theory for life prediction and accelerated testing under random vibrations is also well formalized for leaded solders [Steinberg 1988, Hu 1995, Henderson et al 1995]. Typical failures under vibration loads are due to high cycle fatigue occurring after several million cycles [Wong 1997] and may demonstrate multiple failure modes of solder fatigue, copper trace or lead fracture. Finite element modeling approaches for PCBs [Pittaresi 1990, Pittaresi et. al. 1991, 1993, Lall et. al. 2004, 2005] and stress analysis for component and solder joint reliability under random vibration can also be found in current literature [Lau 1991, Upadhyayul et. al. 1997, Li 1999, 2001]. Prior studies on the effect of concurrent thermal cycling and dynamic loading on electronic components have suggested incremental damage superposition approach for predicting solder joint reliability [Barker et. al. 1990, 1992, Basaran et. al. 2002, Qi et. al. 2004]. The behavior of 63Sn/37Pb solder under in-plane vibration at high temperature has been studied [Zhao et. al. 1999].

Second level solder interconnect stress investigation under dynamic loads has largely relied on FE based simulations. The purpose of the investigation presented in this paper is to study the behavior of SAC305 solder joints under out of plane vibration at elevated temperature. The test vehicle has been tested to failure subjecting it to out of plane harmonic vibrations at its first natural frequency inside an isothermal chamber. Digital Image Co-relation (DIC) has been used to measure full field displacement and deformation gradient on the PCB. Previously, DIC has been used to accurately measure deformations in electronic assemblies subjected to drop and shock [Lall et. al. 2007b, Miller et. al. 2007, Park et. al. 2007a,b, 2008]. Global-local sub-modeling has been used to predict the solder joint stresses. The component deformation is governed by the PCB deflection. Material properties of PCB change with increase in the test temperature even below the glass transition temperature. This has been demonstrated by measuring the change in natural frequency as a function of temperature. In this study, modal analysis has been conducted at each elevated test temperatures and PCB material properties have been determined using Dynamic Mechanical Analyzer through each test temperature. Dynamic characteristics of the system including the natural frequencies, mode shapes and the out of plane displacement have been used to correlate the global model with the test vehicle. Prior researchers have plotted S-N curves for SAC alloys using a combination of experimental and finite element modeling techniques [Al-Yafawi et. al. 2010]. In this paper the authors have developed a methodology to obtain the solder stresses at elevated test temperatures. Arrhenius theory has been used to develop a predictive model that would fit through the S-N curves at elevated temperature. Basquin power law for SAC305 solder has been modified by introducing temperature dependent fatigue coefficient and fatigue exponent terms.

2.2. Digital Image Correlation

Owing to the complexity of electronic assemblies, it is not feasible to place deformation measuring devices such as strain gages on them. Additionally, conventional deformation measuring techniques only evaluate localized values. With a multitude of components on a single test assembly, it is beneficial to have an estimate of full field deformations for subsequent evaluation of individual component response.

Digital Image Correlation (DIC) is a novel technique which works by tracking a geometric point on the specimen before and after deformation, thereby enabling full field strain and displacement measurement during a transient dynamic event. Geometric points on the test specimen are distinguished by speckle coating the surface of interest. Previous studies have established the effect of size, consistency and density of the speckle pattern on the accuracy of the method [Zhou et. al. 2001, Amodio et. al. 2003, Srinivasan et. al. 2005]. The DIC method has its merits over strain measurement by using strain gage, which measure strain only at localized points on the specimen. Furthermore, the technique does not involve contact with the specimen during the monitored event and specimen preparation is very quick and easy.

The Digital Image Correlation technique has been extensively used in this work to measure field quantities (deformation) and for subsequent calculation of their derivatives(strain). The technique has been employed in this work, in conjunction with high speed imaging systems to evaluate transient dynamic board response to JEDEC standard shock events as well as static bend tests.

High speed photography has previously been used to measure deformations in sheet metal forming, Automotive crash testing, rail vehicle safety[Kirkpatrick et. al., 2001], air- plane safety[Marzougui, 1999], modal analysis of turbine blades, high strain rate Split- Hopkinson bar tests, dynamic fracture phenomenon, and package hermiticity (MIL-STD- 883) tests. High-speed cameras measure impact speed, force, and deformation due to shock, and thermal loading. Previously, the measurement of derivatives of field quantities, such as strains, was limited to a specific physical locations or discrete target points in an electronic structure.

In the field of electronic packaging, DIC has been used to calculate full field deformations and deformation gradient in electronics [Lall et. al. 2007c, 2008b-d, 2009, Miller et. al. 2007, Park et. al. 2007a,b, 2008]. Previously, the DIC based strain measurements technique has been demonstrated to be useful for transient strain measurement in electronic assemblies, in the presence of rigid body motion Lall 2007 2008]. Digital image correlation also been employed to study deformations in printed circuit assemblies for mobile devices [Lall et. al. 2007, Miller et. al. 2007, Park et. al. 2007], material characterization [Park et. al. 2007] for evaluation of stresses and strain in flip-chip dies under thermal loading [Kehoe et. al. 2006] and for calculating stresses in solder interconnects of BGA packages under thermal loading conditions [Zhou et. al. 2001]. DIC has also been used for evaluating elastic modulus of underfill materials at elevated temperatures during four-point bending tests [Park 2007a, Shi 2007]. In conjunction with high resolution SEM, the method has also been used to study the stresses released at the component surface before and after ion milling [Vogel 2007].

Although the technique has been widely used in thermal analysis of electronic packaging, it has recently gained a lot of attention in the field of transient dynamics as well. DIC algorithms in conjunction with high speed imaging systems are now widely used as tools for acquisition and analysis of deformation images. The technique has been extensively used in this study for evaluation of test vehicle deformation during transient dynamic as well as static mechanical events.

2.3. High Strain Rate Solder Characterization

With the ROHS initiative on lead-free solder taking effect, the electronics industry has been presented with a wide array of lead-free options. Most of the Pb-free alloys in the industry today are plagued by aging and creep issues. Prior researchers have shown a deterioration of the material properties of SAC alloys with constant temperature aging [Lall 2012 et. al., Ma et. al. 2009, Zhang et. al. 2009, Darveaux 2005]. New developments in the Pb-free options have introduced small proportions of Ni, Zn, Co, Bi, Sb in the SAC alloys to increase resistance to aging and creep while maintaining the melting temperature and strength of the alloy comparable to SAC. Many researchers have shown enhanced material properties, microstructures and resistance to failures in thermal cycling due to the addition of rare earth elements in SAC alloys [Zhang et. al. 2009, Liu et. al.]. InnoRelTM have introduced a new Pb-free alloy- Innolot, which consists of Ni, Sb and Bi in its composition (Table 2). This alloy has a melting range between 206C to 218C. Increased creep strength is a result of solid solution hardening and dispersion hardening mechanisms achieved by Bi, Sb dissolution in Sn crystal matrix and intermetallic phases by Ni. Prior studies have shown that Innolot is more reliable in thermal cycling as compared to SAC alloys [Miric et. al. 2010].

The effects of aging on the microstructure and material properties of Pb-free alloys have been investigated at low strain rates less than 1/s [Chuang et. al. 2002, Coyle et. al. 2000, Darveaux 2005, Lee et. al. 2002, Pang et. al. 2004, Zhang et. al. 2009]. For high strain rate constitutive behavior investigation, researchers have relied on Split Hopkinson Pressure bar tests [Chan et. al. 2009, Siviour et. al. 2005]. The strain rates achievable with this equipment, range from 500/s to 3000/s. In practice, the typical strain rates observed on second level interconnects in consumer electronics drop impacts are within 1/s to 100/s. Neither the Split Hopkinson Pressure bars nor conventional pull tester can be easily used to obtain these strain rates. Very few researchers have characterized Pb-free solder properties at strain rates of 1/s to 100/s [Lall et. al. 2011, 12, Meier et. al. 2009, Wong et. al. 2008]. The authors of this paper have explicitly demonstrated the capability of an innovative tensile tester to repeatably obtain constant strain rates of 10/s, 35/s and 50/s. The effect of strain rate and aging on the material properties of SAC105 and SAC305 has been established through this work [Lall et. al. 2012]. In this paper, the same equipment and aging conditions have been used for two strain rates of 10/s and 35/s to characterize the constitutive behavior of Innolot. A comparison of the effects of strain rate and aging on Innolot and SAC alloys (SAC105 and SAC305) has been presented.

Non-linear Ramberg-Osgood model [Lall et. al. 2012, Nguyen et. al. 2011, Ohguchi et. al. 2006, Chen et. al. 2006, Muller et. al. 2005, Pang et. al. 2004, Park et. al. 2002, Lee et. al. 1997, Knecht et. al. 1990] and Anand's viscoplastic model [Mysore et. al. 2009, Bhate et. al. 2008, Yeo et. al. 2006, Pei et. al. 2005, Rodgers et. al. 2005, Wang et. al. 2005, Pang et. al. 2004, Wang et. al. 2001, Wilde et. al. 2000] are amongst the most popular models to describe solder stress-strain behavior. Prior researchers have used finite element analysis for modeling tensile tests [Lall et. al. 2012, Joun et. al. 2007, Niordson et. al. 2004, Cabezas et. al. 2004, Peng et. al. 2004, Koc et. al. 2004, Mirone 2004, Tang et. al. 2003, Inal et. al. 2002, Komori 2002, Nilsson 2001]. This research, uses Ramberg-Osgood model for its implementation in Abaqus based FE codes.

In the past, Digital Image Correlation (DIC) has been used for material characterization at low strain rate testing of composites [Gershon et. al. 2010, Srinivasan et. al. 2005, Grytten et. al. 2009] and high strain rates for lead-free solder characterization [Lall et. al. 2012, 2011, 2010, Tiwari et. al. 2005] to investigate full-field displacement and strain contours as the test specimen deforms and fractures. DIC has been implemented in this work to correlate Ramberg-Osgood FE models with the experimental data.

Table 2: Innolot Composition [Miric et. al. 2010]

Element	Min %	Max %
Sn	Balance (90.1-91.6)	
Ag	3.6	4.0
Cu	0.6	0.8
Ni	0.1	0.2
Sb	1.3	1.7
Bi	2.8	3.2

CHAPTER 3

HIGH CYCLE FATIGUE CHARACTERIZATION OF SAC305 INTERCONNECTS UNDER SIMULTANEOUS EXPOSURE TO HIGH TEMPERATURE AND VIBRATION

3.1 Introduction

Electronic components in automotive applications get exposed simultaneously to high temperature and dynamic loads during their life cycles. Studies on automotive temperature extremes have recorded continuous maximum temperatures upto 140C and vibration level up to 10G RMS [Johnson, 2004]. The significance of studying reliability under this type of environment is even more consequential for off-road automotives like construction and agricultural machinery. Both, high temperature and vibrations contribute to the failures in such system. The reliability of electronic products can be improved through a thorough understanding of the weakest link in the electronic systems which is the solder interconnects. There is a lack of fundamental understanding of reliability of electronic systems subjected to extended period of vibrations at elevated temperature. Most of the research is focused on reliability of solder interconnects subjected exclusively to vibrations or thermal cycling. Relatively few researchers have studied the reliability in the simultaneous environment of thermal cycling and vibration. In this paper, the authors have characterized the high cycle fatigue S-N curves of lead-free solder at various constant temperature. Most of the early research in the area of reliability of solder joints is focused on thermal cycling which includes low cycle fatigue failure modes. Researchers have developed the theory and life prediction models for solder fatigue subjected to thermal cycling [Tavernelli 1962]. Similarly, the theory for life prediction and accelerated testing under random vibrations is also well formalized [Steinberg 1988, Hu 1995, Henderson et al 1995]. Typical failures under vibration loads are due to high cycle fatigue occurring after several million cycles [Wong 1997] and include solder fatigue, copper trace or lead fracture. Finite element modeling approaches for PCBs [Pittaresi 1990, 1991, 1993, Lall 2004, 2005] and stress analysis for component and solder joint reliability under random vibration can also be found in current literature [Lau 1991, Upadhyayul 1997, Li 1999, 2001]. Prior studies on the effect of concurrent thermal cycling and dynamic loading on electronic components have suggested incremental damage superposition approach for predicting solder joint reliability [Barker 1990, 1992, Basaran 2002, Qi 2004]. The behavior of 63Sn/37Pb solder under in-plane vibration at high temperature has been studied [Zhao 2000].

Second level solder interconnect stress investigation under dynamic loads has largely relied on FE based simulations. Previously, global models have been investigated using equivalent layer models [Gu 2005], smeared property models [Clech 1997, Lall 2004, 2005]. The purpose of the investigation presented in this paper is to study the behavior of SAC305 solder joints under out of plane vibration at elevated temperature. The test vehicle has been tested to failure subjecting it to out of plane harmonic vibrations at its first natural frequency inside an isothermal chamber. Digital Image Co-relation (DIC) has been used to measure full field displacement and deformation gradient on the PCB. Previously, DIC has been used to accurately measure deformations in electronic assemblies subjected to drop and shock [Lall 2007b, Miller 2007, Park 2007a,b, 2008]. Global-local sub-modeling has been used to predict the solder joint stresses. The component deformation is governed by the PCB deflection. Material properties of PCB change with increase in the test temperature even below the glass transition temperature. This has been demonstrated by measuring the change in natural frequency as a function of temperature. In this study, modal analysis has been conducted at each elevated test temperatures and PCB material properties have been determined using Dynamic Mechanical Analyzer (DMA) through each test temperature. Dynamic characteristics of the system including the natural frequencies, mode shapes and the out of plane displacement have been used to correlate the global model with the test vehicle. Prior researchers have plotted S-N curves for SAC alloys using a combination of experimental and finite element modeling techniques [Al-Yafawi 2010].]. In this paper the authors have developed a methodology to obtain the solder stresses at elevated test temperatures. Arrhenius theory has been used to develop a predictive model that would fit through the S-N curves at elevated temperature. Basquin power law for SAC305 solder has been modified by introducing temperature dependent fatigue coefficient and fatigue exponent terms.

3.2 Test Vehicle

The test vehicle used for this study is a representative of engine control unit of an agricultural equipment. It has dimensions of 204mm x 129mm x 1.56mm. The test board has a variety of surface mount daisy chain packages including plastic ball grid array (PBGA), quad flat package (QFP), thin small outline package (TSOP), and small outline package (SOL) mounted on a high glass transition printed circuit board as shown in Figure 6. Each daisy chained package is traced across two connector pins. Both, the leaded and BGA packages have SAC305 lead-free solder interconnects. The test board surface finish is immersion silver. The mass of the test vehicle is 133.46 gram. The attributes for each package are tabulated in Table 3. Die sizes are measured by scaling the known dimensions on the X-ray images in Figure 7. BGA configurations have been modeled as seen in the X-rays.

Table 3:Package attributes

Package	**Pitch (mm)**	**Lead thickness or Ball diameter (mm)**	**Solder alloy system**	**I/O count**	**Mass (gram)**
QFP	0.65	0.33	SAC305	144	5.86
BGA	1.27	0.75	SAC305	46,272,388,	4.05
TSOP	0.5	0.254	SAC305	48	0.54
SOL	1.27	0.43	SAC305	16,24,32	0.85

Figure 6: Product form-factor test vehicle

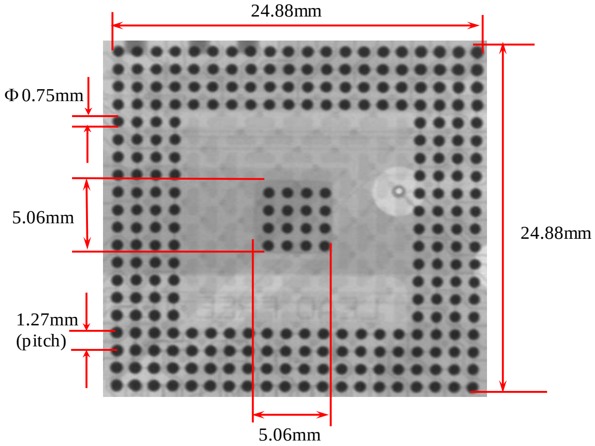

BGA 272

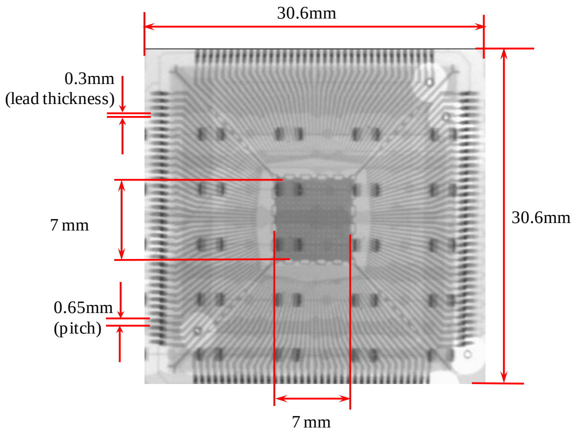

QFP 144

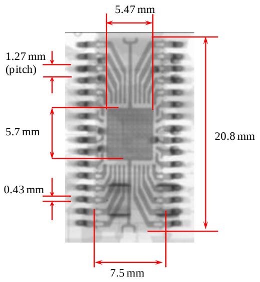

SOL 32

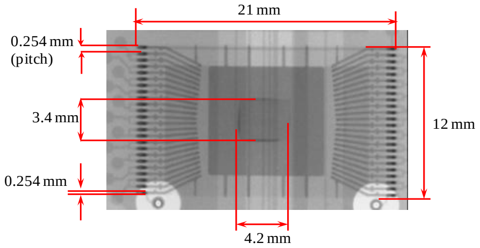

TSOP 48

Figure 7: X-ray images of components

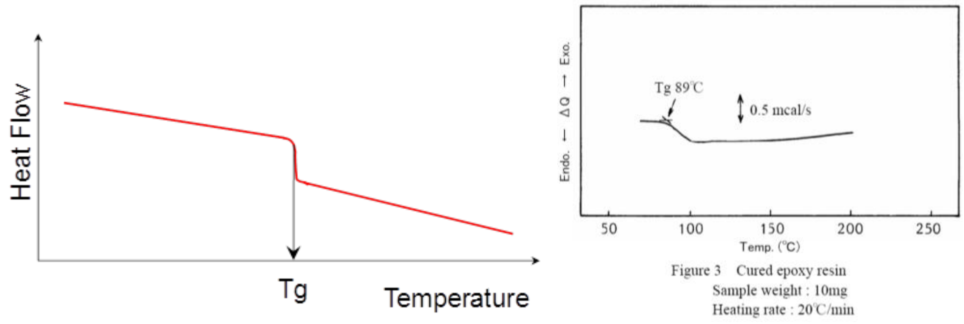

(a) (b)

Figure 8: a) Cartoon of Tg measurement using DSC [Adapted from: www.arlon-med.com] b) Tg using DSC of cured epoxy resin [http://www.siint.com/en/documents/technology/thermal_analysis/application_TA_008e.pdf]

Differential Scanning Calorimetry (DSC) is often used to identify the Tg of a composite. [Figure 8] shows a cartoon of a typical DSC plot. A stepwise decrease in the heat capacity of a specimen marks the glass transition temperature (Tg).

Differential Scanning Calorimetry (DSC) was conducted on a small sample of the PCB weighing 2.3mg. using the equipment shown in Figure 9 The heat flow vs temperature plot shown in Figure 10 does not show a sudden change in the heat flow through the sample during DSC which verifies that the glass transition temperature Tg of the PCB is well above the selected test temperatures. This test vehicle has a 4-layer FR4 laminated PCB designed for Pb-free components.

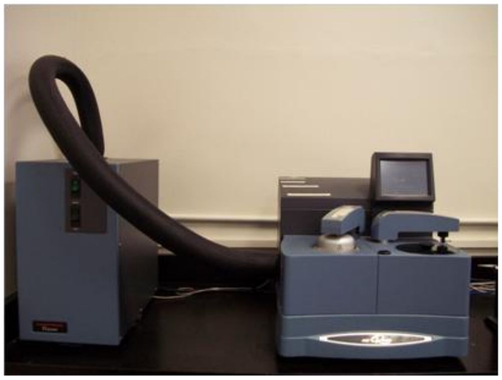

Figure 9: Differential Scanning Calorimeter from TA Instruments, model Q2000

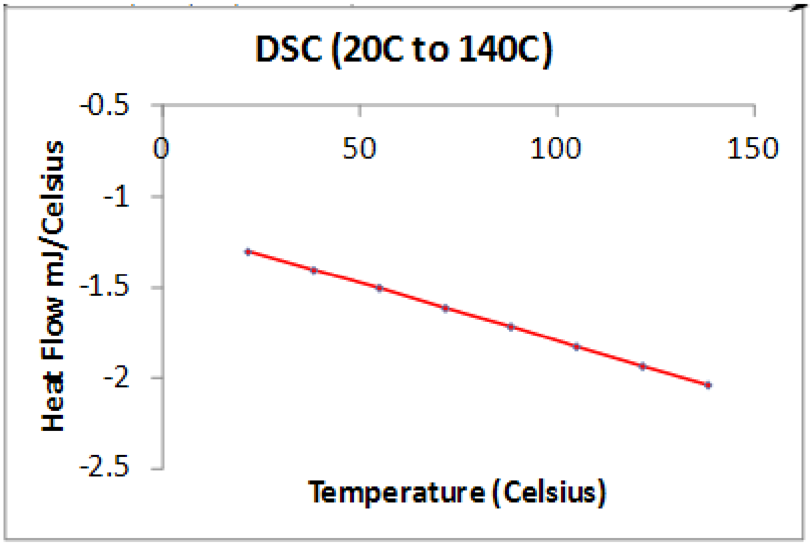

Figure 10: DSC plot for PCB sample, Tg>140C

3.3 Harmonic Vibration Testing at Elevated Temperature

The test vehicles have been randomly allotted to one of the case shown in the test matrix [Figure 11]. Baseline data is collected by setting the chamber temperature to 25C. Additionally, two elevated temperatures of 75C and 125C have been used. The test temperatures have been selected based on typical temperatures observed in automotive environment.

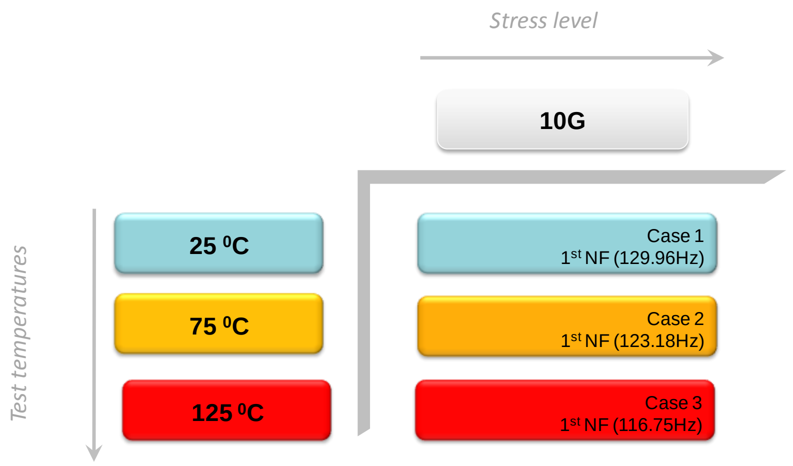

Figure 11:Test Matrix

An isothermal oven is mounted on the shaker to enable temperature control. It has a glass window on top to acquire high speed video of the PBC deformation. In each case, the board is subjected to harmonic vibration dwelling at the corresponding first natural frequency with amplitudes of 10G. The wires connected on the PCB are taken out of the chamber and given as input to the high speed data logger. The resistance across daisy chained packages U4, U5, U17, U18, U19, U20, U21 [Figure 12] have been monitored using this high speed data logger.

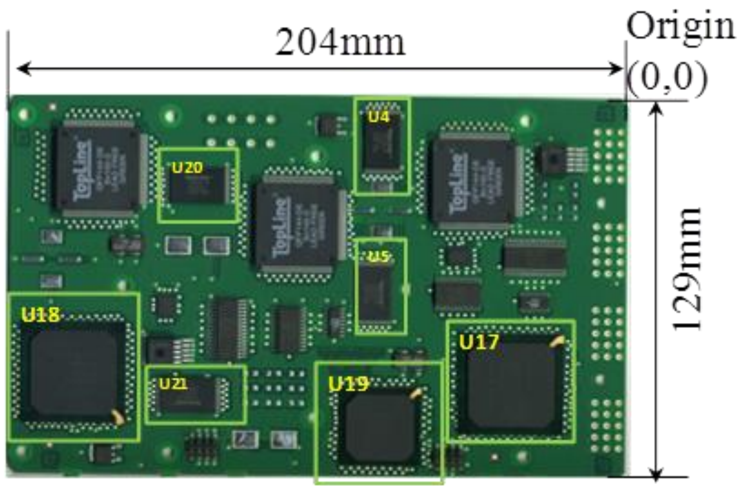

Figure 12:Packages selected for test to failure

For a data logger, the electrical discontinuity is defined as a 20% resistance increase from the initial resistance value and the failure of a solder joint is defined as the first such event within five or more consecutive scans. Note that less than 3 seconds per scan is required for a data logger. The test is continued till all the aforementioned packages have failed. The time to failure is calculated based on the difference between the time stamp of the start of test and failure event for every package. Since a input vibration is at a constant frequency, the time to failure is easily converted to cycles to failure. Figure 13 shows the complete test setup.

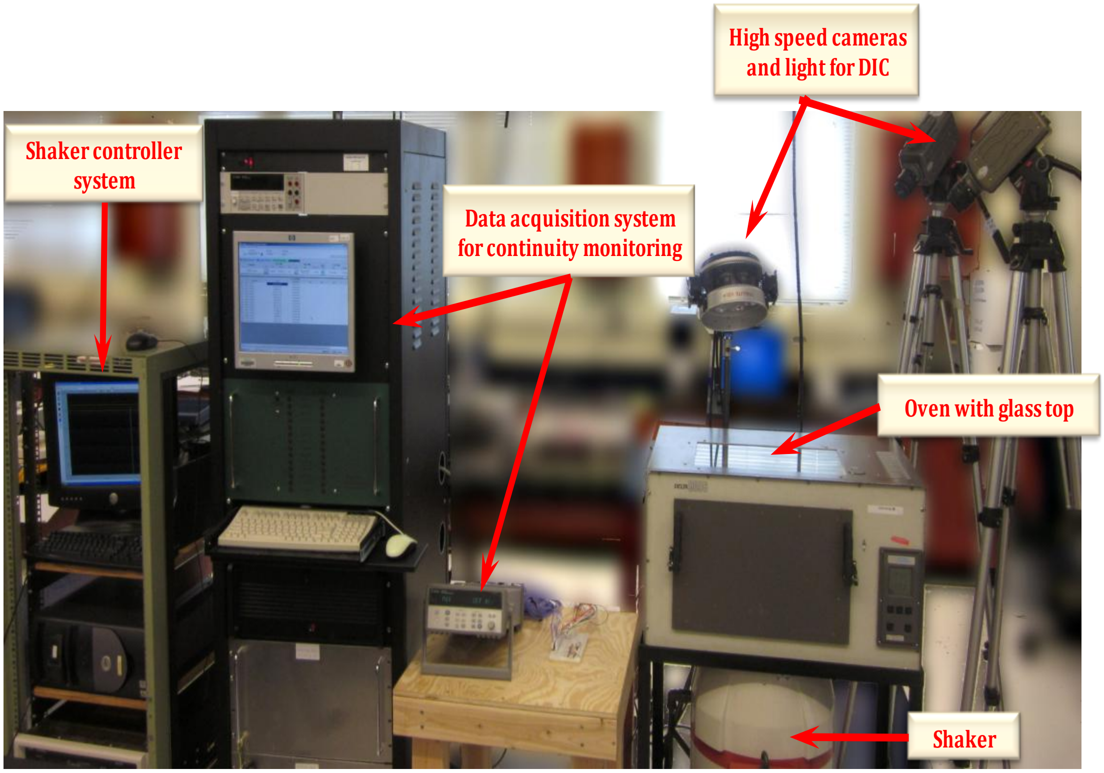

Figure 13:Test setup

3.4 Approach to Solder High Cycle Fatigue Life Prediction at elevated Temperature

The methodology used in this study is represented in the flow-chart depicted in

Figure 14. Experimental Modal Analyisis (EMA) is conducted on the test vehicle described in the previous section. Three temperatures: 25C, 75C and 125C have been used to conduct the EMA. The 1st natural frequency is located at each test temperature for subsequent tests to failure. Tests to failure have been conducted on the test vehicles by subjecting simultaneously to elevated temperature and sinusoidal vibrations at the corresponding 1st NF. High speed data acquisitions systems monitor the daisy chain resistance of each package to detect an increase in resistance leading to open event. Cycles to failure are counted based on time to failure. A smeared property global model of the test vehicle is constructed for FE based modal analysis. The PCB properties in this model are recursively updated to obtain a good correlation with EMA. Properties obtained by this technique are compared with PCB properties from conducting a dynamic mechanical analysis. Digital Image correlation is used to obtain full field displacement and strain contours of the board deformation. The deformations of the global model are correlated to further ensure good correlation between global model and the test vehicle. Dynamic explicit submodels of the failed components with temperature dependent PCB and solder properties give the solder level stresses at each temperature. S-N curve at the three test temperatures is obtained from cycles to failure and stress levels from sub models. Basquin power law is updated to incorporate the temperature dependence of the fatigue coefficient and exponent based on Arrhenius equation.

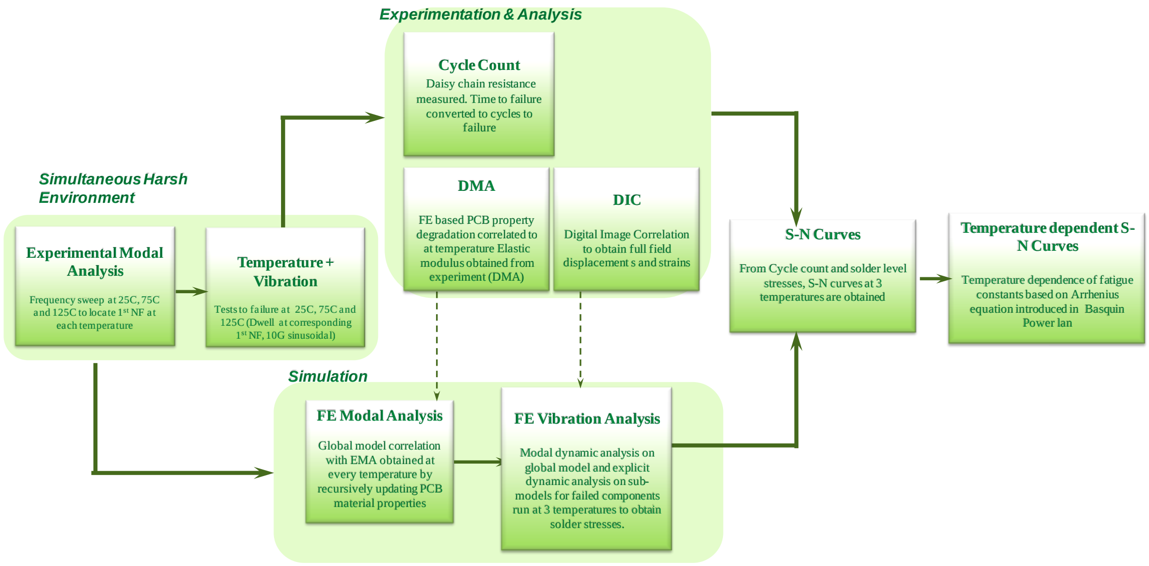

Figure 14: Approach to obtain elevated temperature S-N Curves

3.5 Correlation of Test Vehicle with Global FE Model

Solder stress characterization in dynamic analyses relies largely on finitely element analysis of well correlated FE models. However, a detailed model of the PCB is often very difficult to mesh and computationally inefficient to solve. In order to overcome this problem, it is necessary to build an equivalent FE model with equivalent material properties. Such a model is referred to as the global model. The detailed models of each component called sub-models, derive their boundary conditions at the local degrees of freedom from the global model. It is therefore essential to correlate the global model with the physical test vehicle.

Modal analysis is the base to measure the response of the test vehicle to dynamic loads. The mode shapes, natural frequencies and structural damping have been obtained from this analysis. A light weight accelerometer of 2.05 gram is adhered to the PCB at two different locations. Figure 15 shows the setup with accelerometer located at the center. The board is mounted using standoffs at four corners on the shaker table with its packages facing down. The top side of the board is coated with a black random speckle pattern on a white background coat. A sine sweep profile from 5Hz to 500Hz with constant amplitude of 10G is entered in the shaker controller. Accelerometer mounted on the shaker measures the excitation signal and the other accelerometer mounted on the PCB measures the response. A transmissibility plot is obtained from this test. The excitation frequency corresponding to every peak in the transmissibility plot denotes the natural frequency of the board. The plots obtained from mounting the response accelerometer at the two locations are over-laid to find the first four natural frequencies [Figure 17].

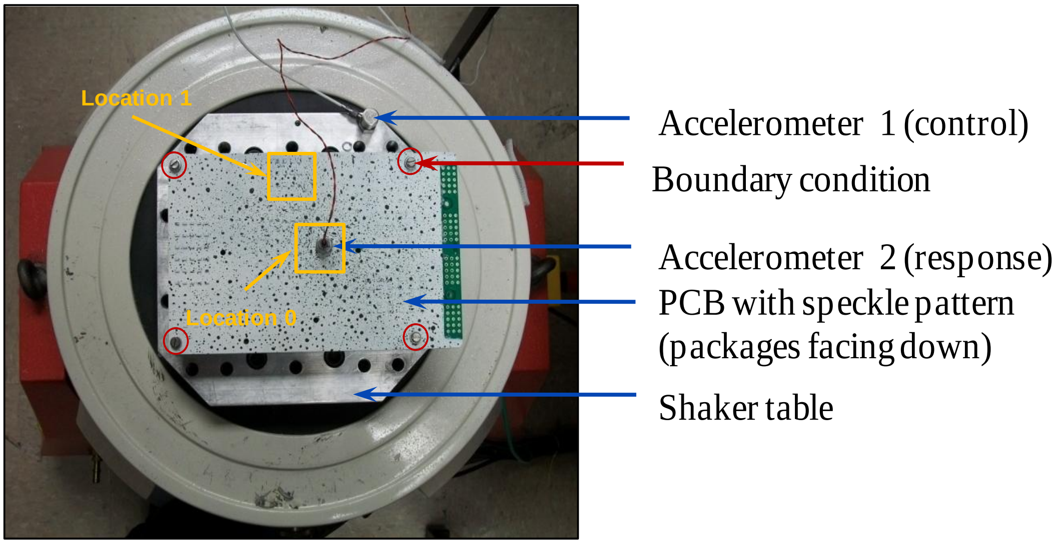

Figure 15:EMA setup

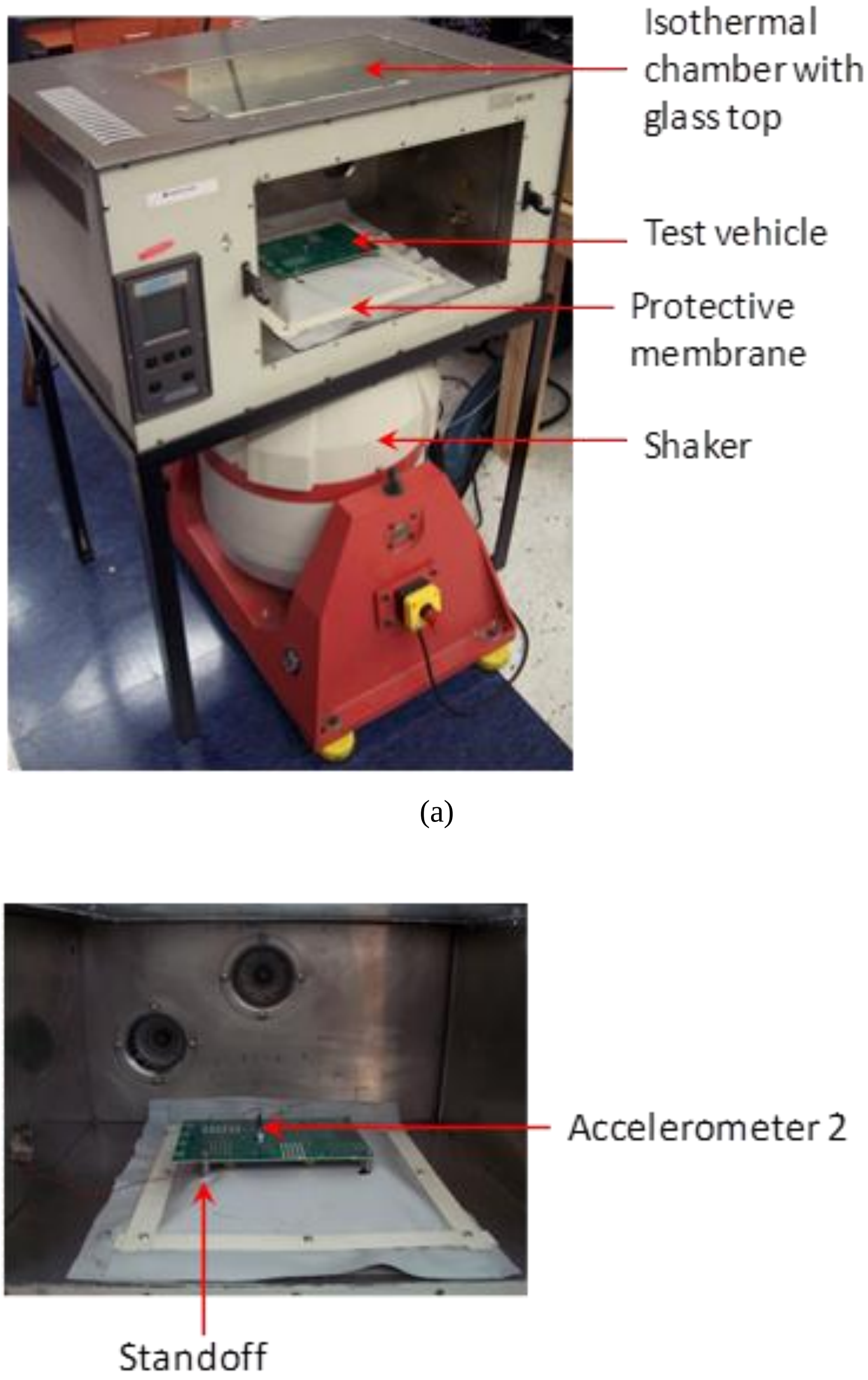

(a)

(b)

Figure 16: a) EMA Setup b) PCB inside the isothermal chamber

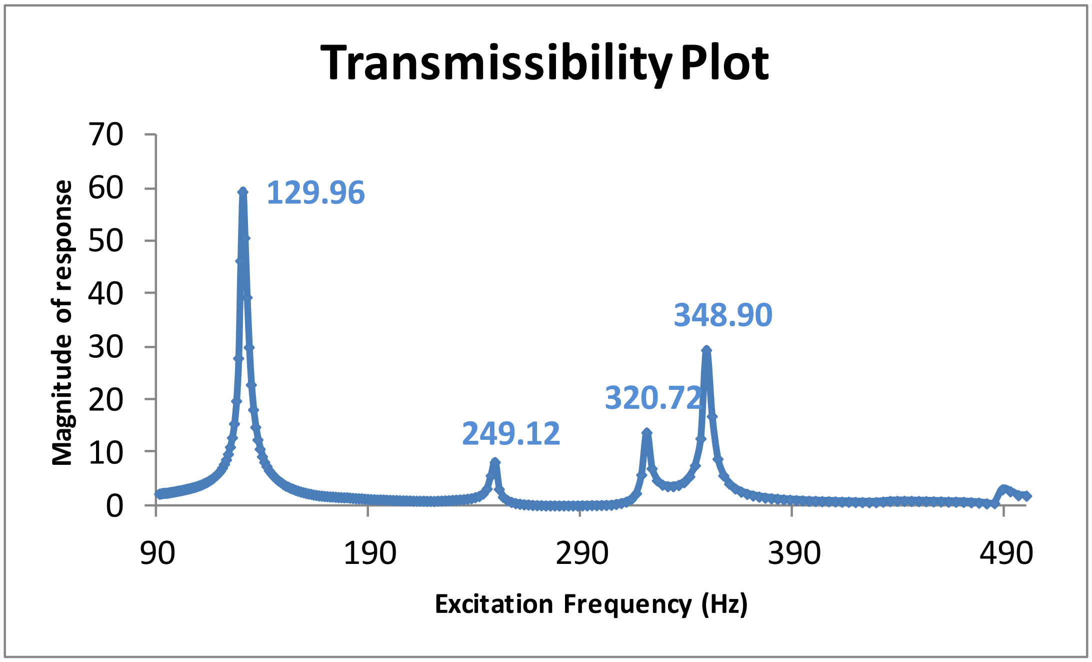

Figure 17:Acceleration response denoting natural frequencies

Dynamic characteristics have been evaluated at elevated temperatures of 50C, 75C, 100C and 125C. Figure 18 demonstrates the dependence of the first natural frequency of the test vehicle on the test temperature. The R2 value obtained for a straight line fit is 0.9978 which implies that the natural frequency decreases very linearly with increase in temperature.

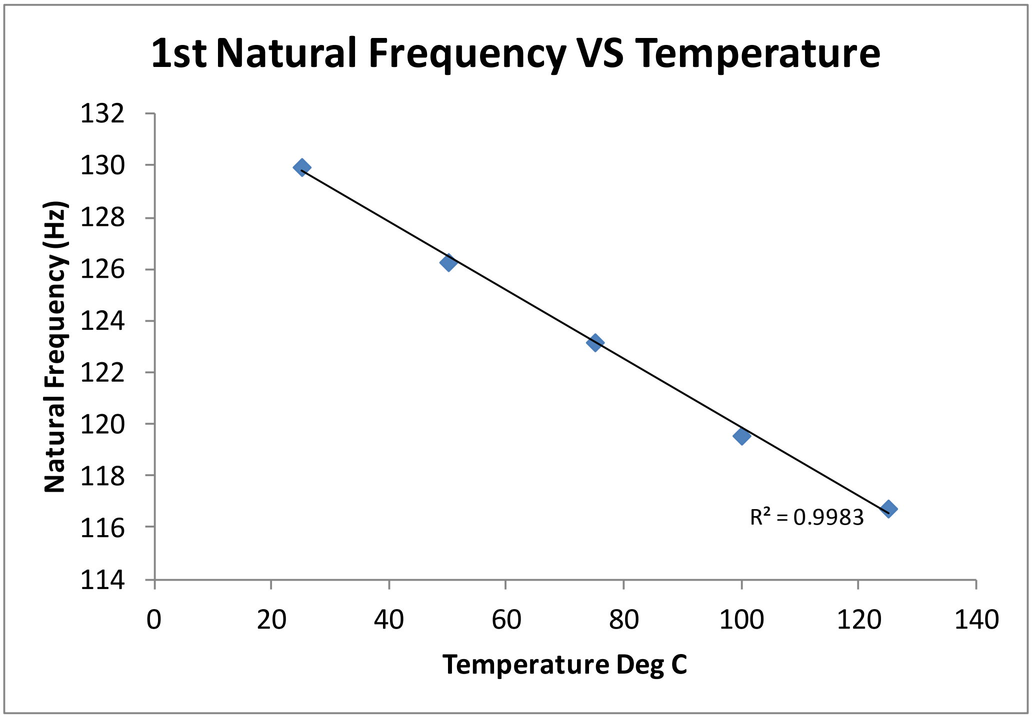

Figure 18: Change in 1st natural frequency as a function of temperature

For a system excited close to its resonant frequency, the damping ratio becomes a very critical dynamic characteristic. It enforces steady state of the response of the system. Half-power bandwidth method shown in Eq. (20) is used for lightly damped structures. Figure 19 shows the acceleration response from 100Hz to 150Hz. f_n=129.96Hz and Δf_n=3.5Hz at 25C for clarity. From Eq. (20), the damping ratio is calculated to be 0.013

$$\xi = \frac{\Delta f_n}{2 f_n} \tag{20}$$

where ξ is the damping coefficient, f_n is the natural frequency and Δf_n is the difference in half-power bandwidth frequencies. Figure 19 shows the acceleration response from 100Hz to 150Hz. f_n=129.96Hz and Δf_n=3.5Hz at 25C for clarity. So the damping ratio is 0.013.

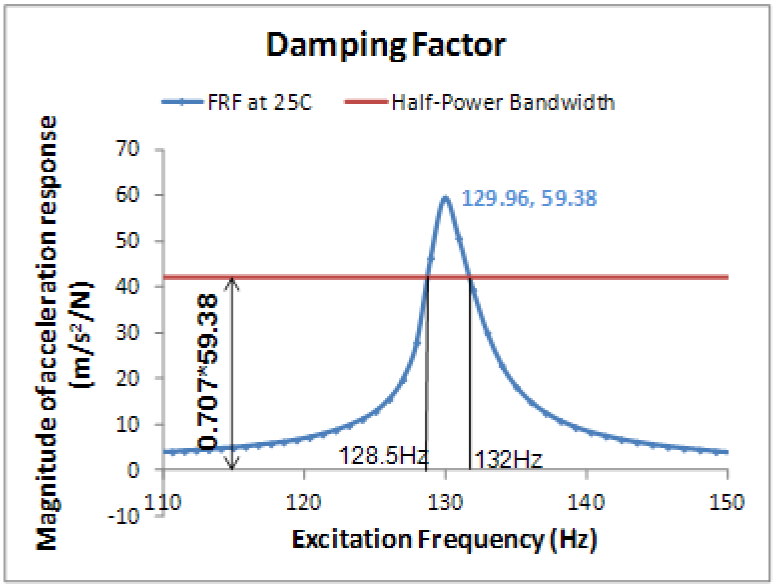

Figure 19:Experimental mode shape at 1st natural frequency

The damping coefficient can further be split into Raleigh coefficients - mass damping coefficient and stiffness damping coefficient. [Papagiannaopoulos et. al.2011]

$$\alpha = \xi \frac{2\omega_1\omega_2}{\omega_1 + \omega_2} \tag{21}$$

where α is the mass damping coefficient. Substituting for the terms on the RHS of Eq. (21):

$$\alpha = 0.013 \frac{2 \times 2\Pi(132 \times 128.5)}{132 + 128.5} \tag{22}$$

$$\alpha = 10.64 \tag{23}$$

The stiffness damping coefficient is given by: [Papagiannaopoulos et. al.2011]

$$\beta = \xi \frac{2}{\omega_1 + \omega_2} \tag{24}$$

$$\beta = 0.013\frac{2}{2\Pi(132+128.5)} \tag{25}$$

$$\beta = 1.59\times10^{-6} \tag{26}$$

It can be seen by comparing Eq.(23) and Eq.(26) that the mass damping is higher than the stiffness damping for this structure.

The global model built for FE simulations is shown in Figure 20. The mass of this model is 134.3 gram and uses smeared properties for the packages. Table 4 shows the comparison of actual masses with simulation. Lanczos algorithm is used for Eigen frequency extraction of the global model.

(a)

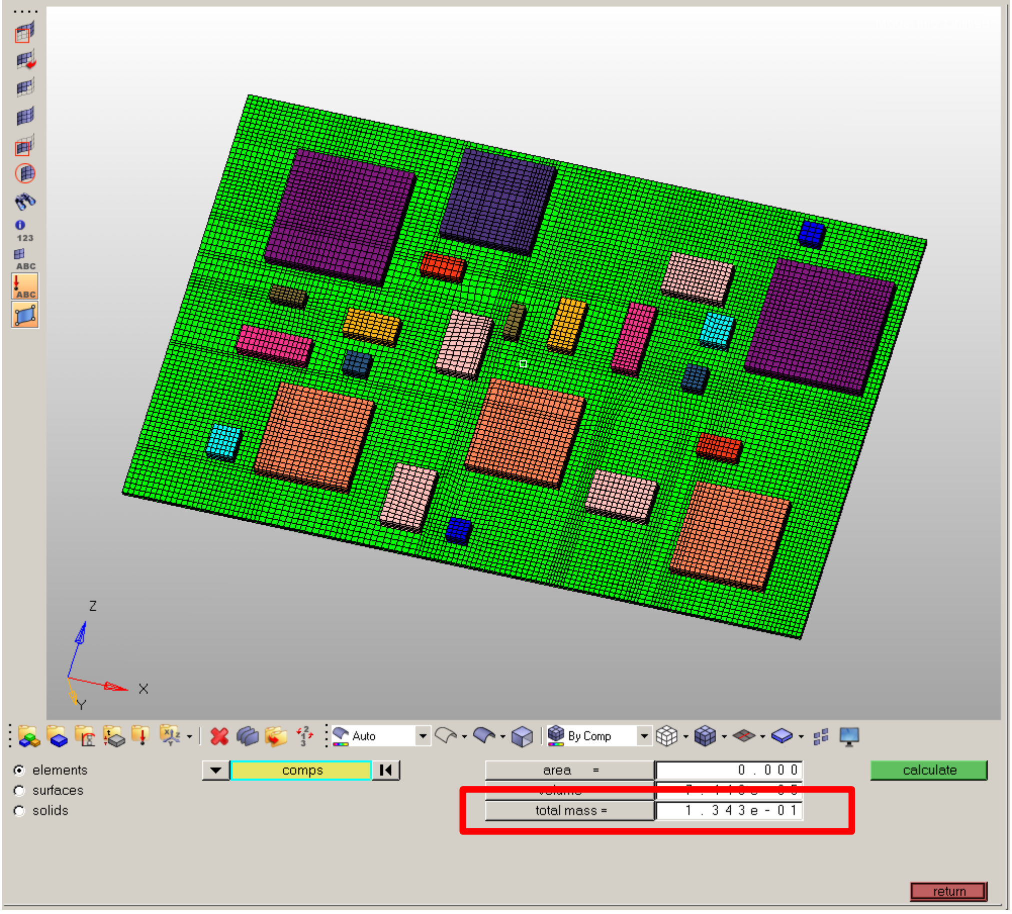

● elements
○ surfaces
○ solids

area = 0.000

total mass = 1.343e-01

(b)

Figure 20:a) Global model for modal dynamic analysis to simulate board deflection

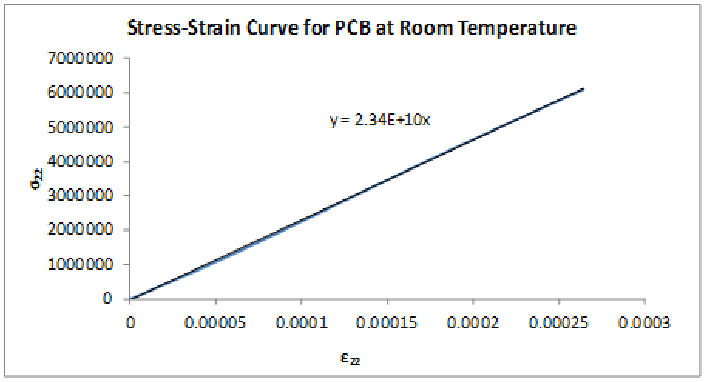

Figure 21:Linear Region of stress-strain curve of PCB

PCB deflections govern the component level stresses and strains. The deflection of PCB for the same input vibration profile can change with change in temperature [Lall 2011]. It is therefore essential to use accurate material properties of PCB at elevated temperatures and use them for the high temperature simulations. Tensile test is conducted to obtain the elastic modulus of PCB. Several samples along various in-plane directions have been used for tensile test. Figure 21 shows one of the representative stress-strain curves. Based on these tests, the PCB modeled as linear elastic isotropic with elastic modulus of 23.8GPa. The degradation in elastic modulus with temperature is assumed to be of the same rate as that obtained from DMA. A dynamic mechanical analysis has been run below the glass transition temperature of the PCB [Figure 22]. At 25C, the modulus is approximately 22GPa. It reduces to 21.1GPa at 75C. The room temperature values obtained in DMA is slightly higher than the value obtained in the average value in tensile test that is used in FE (23.8GPa). But the change in the elastic modulus with temperature is adapted from DMA. A 5.82% drop from 25C values is used for 75C and 14.28% drop from 25C elastic modulus is used for 125C. It should be noted that [Figure 23] for this test vehicle, the dependence of elastic modulus from DMA on temperature can be better described by a quadratic equation: $y = -196099x^2 + 459911x + 2E+10$ ($R^2 = 0.9965$) as compared to a linear equation ($R^2=0.9701$). A quadratic dependence of the Elastic modulus on temperature is inline with the prior observation of linear dependence on temperature of the 1st natural frequency [Figure 18]. Table 7 compares shows the PCB elastic modulus values for FE simulation.

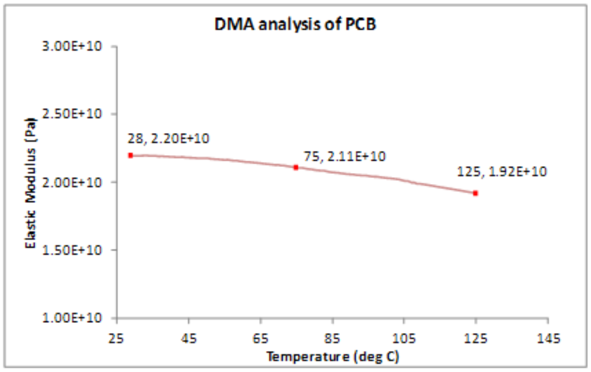

Figure 22: DMA analysis of test vehicle

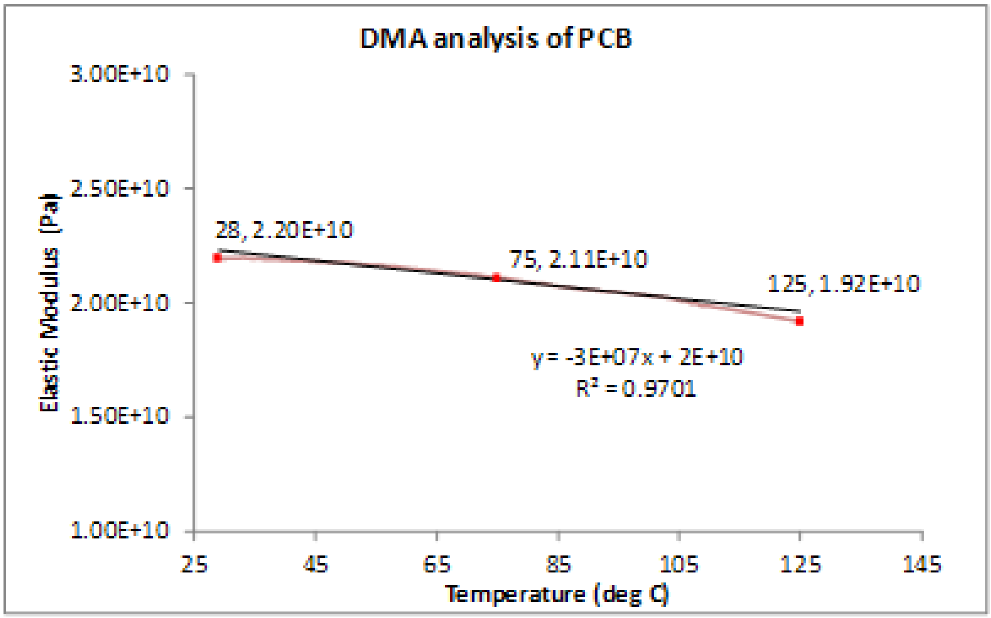

(a)

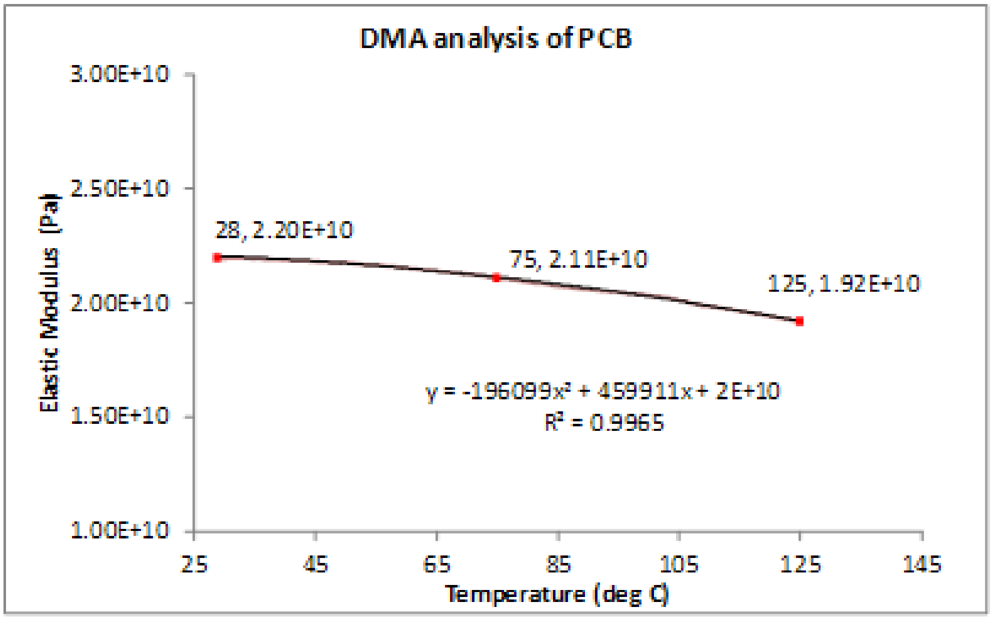

(b)

Figure 23: Dependence of E on temperature a) Linear trend line b) Quadratic trend line

Table 4: Comparison of actual and FE model mass

COMPONENT	ACTUAL WEIGHT (GRAM)	MODEL WEIGHT (GRAM)
BGA 272	2.15	2.13
BGA 388	4.05	3.94
QFP 144	5.86	6.07
TSOP 48	0.54	0.53
SOL 32	0.85	0.85

Smeared properties are used for the components on the global model. In this approach, the component is modeled as block like structure omitting the geometric and material details. The component is then assigned equivalent material properties based on the multi-layer structure of the component.

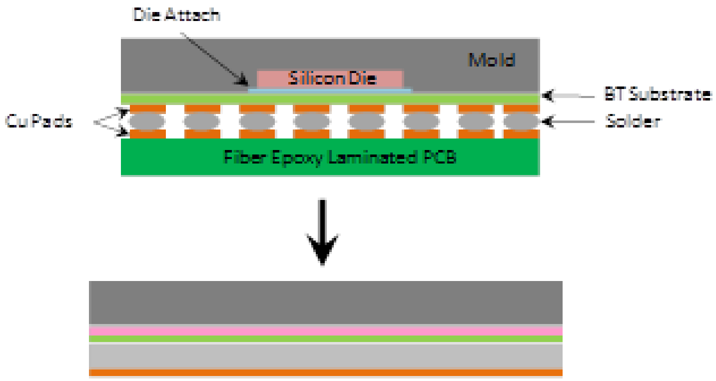

Figure 24: Smeared property model

Eq.(27) gives the effective Poisson’s ratio based on the rule of mixtures widely applied in composite materials [Clech 1997]. The effective Young’s Modulus is obtained by Eq. (28) using the additive property of the bending property of individual layers of the component. The equivalent density in Eq. (29) is the volumetric average of the densities of the layers. Table 5 lists the calculated properties for the components. The temperature effect on the solder property deterioration has a noticeable impact on the effective Young’s Modulus of PBGAs. [Clech 1997]

$$\upsilon_{eff} = \sum_{i}^{n} \upsilon_i h_i \Big/ \sum_{i}^{n} h_i \qquad (27)$$

ν_{eff} is the effective Poisson’s ration of the component ν_i and h_i are the Poisson’s ratios and heights of the layers of the multi-layer stack. [Clech 1997]

$$\frac{E_{eff}\,h^3{}_{eff}}{12(1-\upsilon_{eff})} = \sum_i^n \frac{E_i h_i^3}{12(1-\upsilon_i)} \frac{\Delta f_n}{2f_n} \qquad (28)$$

E_{eff} and h_{eff} are the effective Elastic Modulus and height of the component E_i is the Elastic Modulus of each i layers of the multi-layer stack. [Clech 1997]

$$\rho_{eff} = \sum_i^n \rho_i V_i \Big/ \sum_i^n V_i \qquad (29)$$

ρ_{eff} and is the effective density and V_i is the volume of each of the i layers of the multi-layer stack.

Table 5: Smeared Properties

Component	ρ_{eff} (kg/m^3)	ν_{eff}	E_{eff} (GPa)
BGA 272 U19	2118.51	0.27	4.962 @ 25C 4.96 @ 75C 4.958 @ 125C
BGA 388 U17, U18	1987.34	0.39	4.366 @ 25C 4.365 @ 75C 4.364 @ 125C
QFP 144 U1, U2, U3	1976.42	0.25	12.706
TSOP 48 U4, U5, U2	1962.12	0.27	8.294
SOL 32	1997.76	0.26	9.3

Eigen frequencies are extracted from the global model. The average error in the predicted natural frequency from FE and from EMA is given by Eq. (30). The average error is the mean of the absolute error in the first four natural frequencies obtained by EMA and FEA.

$$RE = \sum_{i=1}^{n} \frac{\left| f_{EMA}(i) - f_{FEA}(i) \right|}{f_{EMA}(i) \times n} \tag{30}$$

where $f_{EMA}(i)$ is the i^{th} NF from EMA and $f_{FEA}(i)$ is the i^{th} NF from FEA and n=4 when considering first four NFs. This procedure is repeated for every test temperature: 25C, 75C and 125C.

Table 6 displays the material properties used for PCB. The PCB is modeled as linear elastic isotropic. Tensile test is conducted at room temperature to measure the elastic modulus. The degradation in elastic modulus is assumed to be of the same rate as the the storage modulus obtained from dynamic mechanical analysis. Hence the percent reduction in modulus from the room temperatures values have been adapted from DMA. Table 7 displays the comparison between EMA and FE results using PCB properties from Table 6. There is a good correlation between natural frequencies obtained by FEA and EMA. Note that the error in 1st natural frequency for all three test temperatures is less than 4%, average error is less than 5% and maximum error is less than 7%.

Table 6: PCB Material properties at temperature

Temperature (deg C)	E from tensile test	E from DMA (GPa)	D MA based % Drop in E wrt E @ 25C	E used in FE (GPa)
25	23.8	22.4	0	23.8
75	-	21.096	5.82	22.41
125	-	19.2	14.28	20.4

Table 7: RE at temperature

25C Properties	EMA	FEA	%error
E1 = 23.8	129.96	129.19	0.59249
	249.12	247.7	0.570006
	320.72	305.68	4.689449
	348.9	327.75	6.061909
		RE	**2.978464**

75C Properties	EMA	FEA	%error
E1 = 22.4	123.18	125.66	2.013314
	237.94	241.53	1.508784
	309	297.37	3.763754
	338.38	318.97	5.736155
		RE	**3.255502**

125C Properties	EMA	FEA	%error
E1 = 20.4	116.75	120.39	3.117773
	225.52	232.32	3.015254
	299.37	285	4.80008
	328.17	305.86	6.798306
		RE	**4.432853**

The frequency extraction step normalizes the peak displacement. Therefore it cannot be used directly for displacement correlation. Instead modal dynamic procedure is used to obtain full field displacement histories of the global model. [Figure 25] shows that the displacement at a randomly selected point on the PCB changes from transient to steady state in about 0.5seconds. A phase shift of 90 degrees can be observed between the excitation and response.

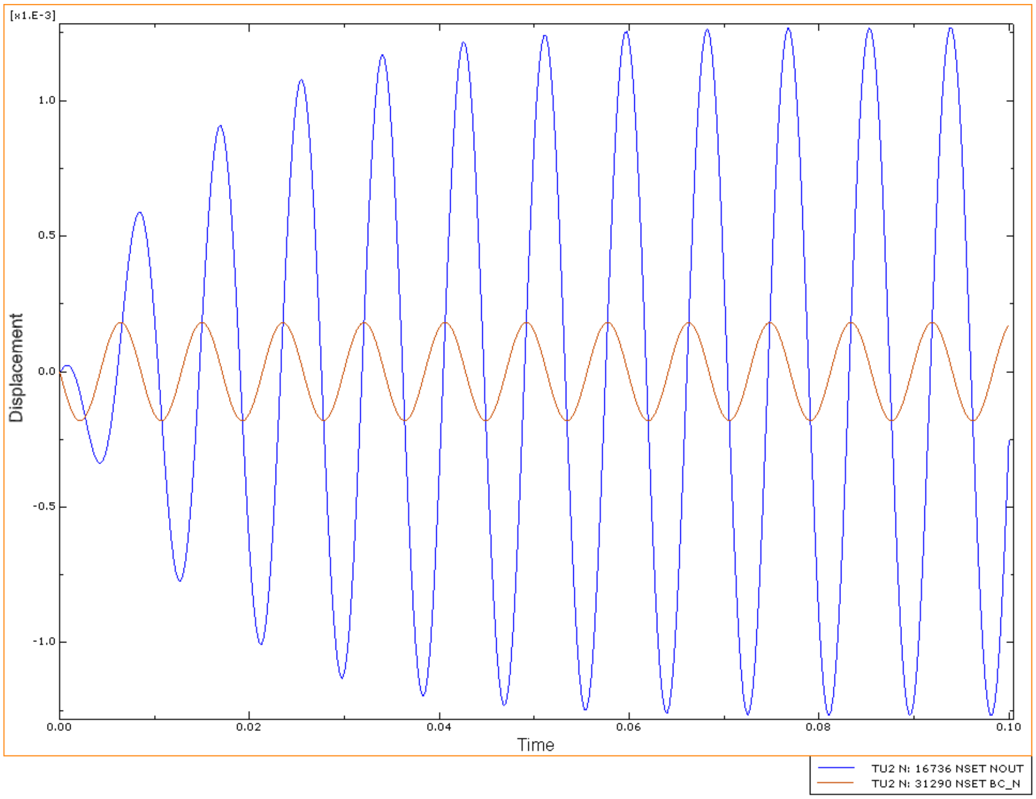

Figure 25:Base excitation and PCB response

Digital Image correlation has been used in conjunction with high speed imaging to correlate the mode shape and the full field displacements of the FE model. Digital image correlation (DIC) is an optical method to measure full-field deformation and the derivatives of deformation on the surface of a loaded structure. Previously, the feasibility of using DIC for transient strain measurement in electronic assemblies, in the presence of rigid body motion has been demonstrated [Lall 2007a-e, 2008a-d]. The technique involves the application of speckle pattern on the surface of the printed circuit board assembly and tracking a geometric point on the speckle patterned surface before and after loading and using it to compute both in-plane as well as out-of-plane deformations in the structures.

Displacement field quantities are obtained by tracking a geometric point before and after deformation [Zhou 2001,Amodio 2003, Srinivasan 2005, Kehoe 2006, Lall 2007c, 2008c,d]. The tracking is achieved using digital image processing of speckle pattern on the specimen surface. Figure 26 shows the principle of DIC in a three-dimensional case. The sub image before deformation is referred as I1 (r) and the one after impact is referred as I2 (r) respectively.

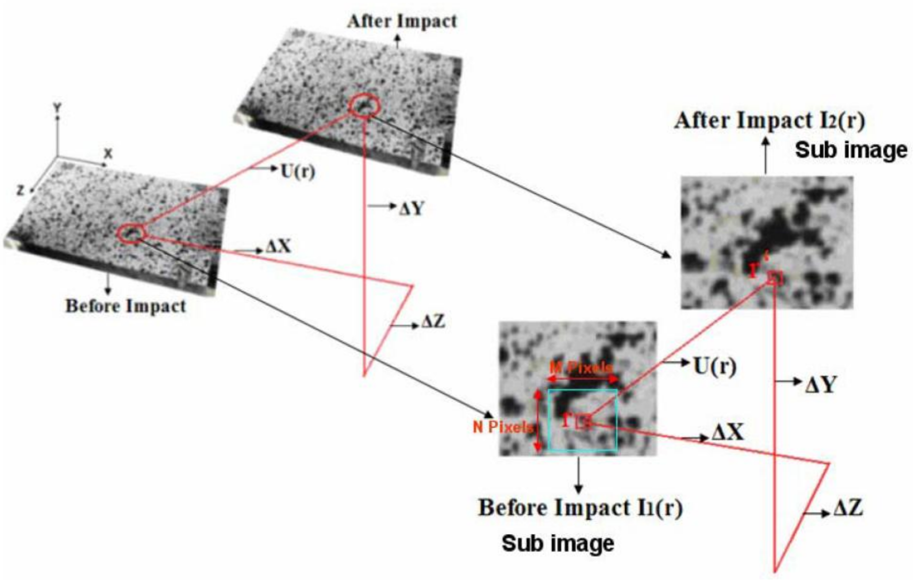

Figure 26:3D-Digital Image Correlation measurements in Printed Circuit Assembly [Lall 2004^{a-d}, 2005^{a-b}, 2006^{a-f}, 2007^{a-e}, 2008^{a-f}, 2009^{a-d}, 2010^{a-j}, 2011, 2012]

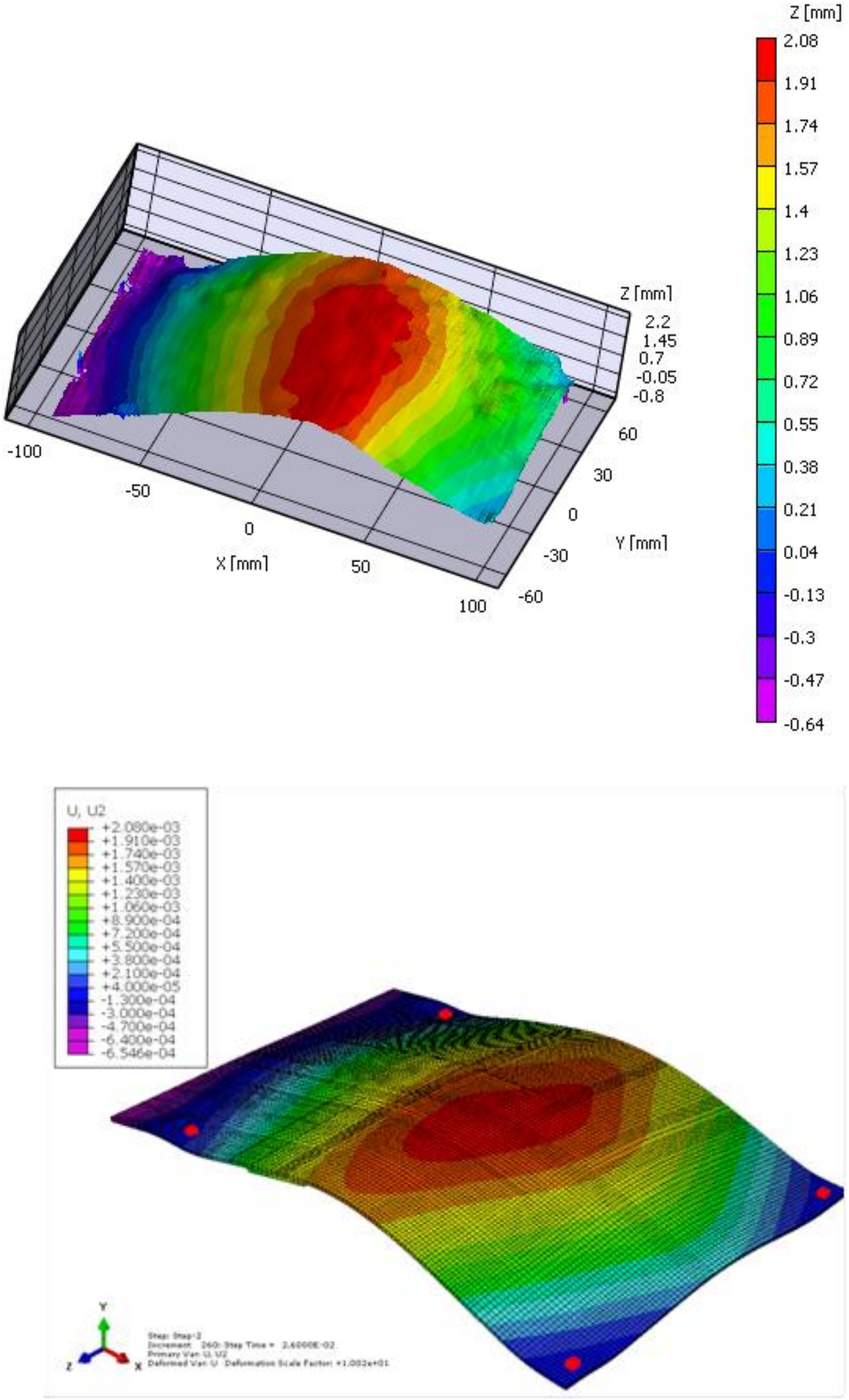

Figure 27:a) Experimental mode shape and full field out of plane displacement contour at 1st natural frequency b)FE mode shape and full field out of plane displacement contour at 1st natural frequency

Figure 27 compares the full field out of plane displacement from DIC and model, both conducted at 25C, 10G and first natural frequency. The mode shape in the two cases resembles closely. Displacement field ranges from -0.06mm to 2mm in DIC and -0.065mm to 2mm in modal dynamic analysis. PCB out of plane displacement and in-plane strain along the length captured by DIC correlate well with those predicted by FEA at the same point A(50,60) at all the test temperatures [Figure 28]. The FE predictions for displacement and strain are slightly lower in amplitude that the DIC values in all the cases. This can be attributed by the higher stiffness predict by FEA.

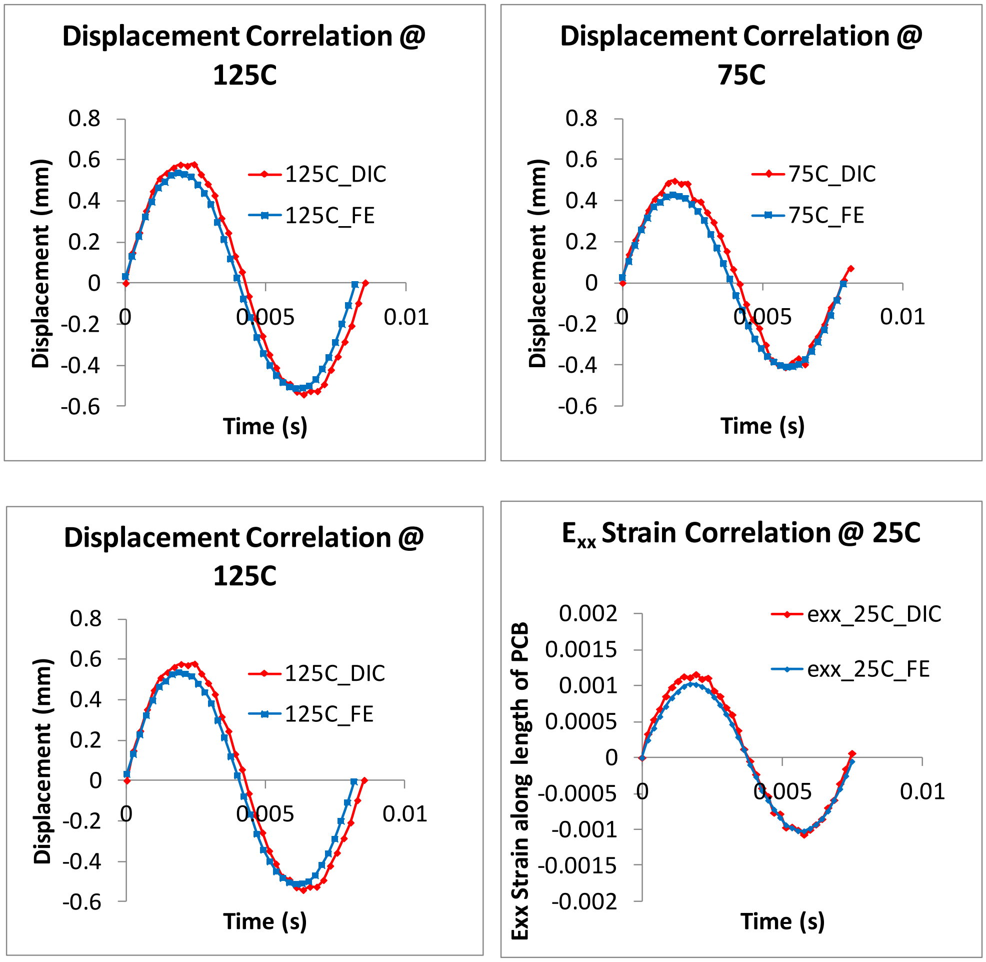

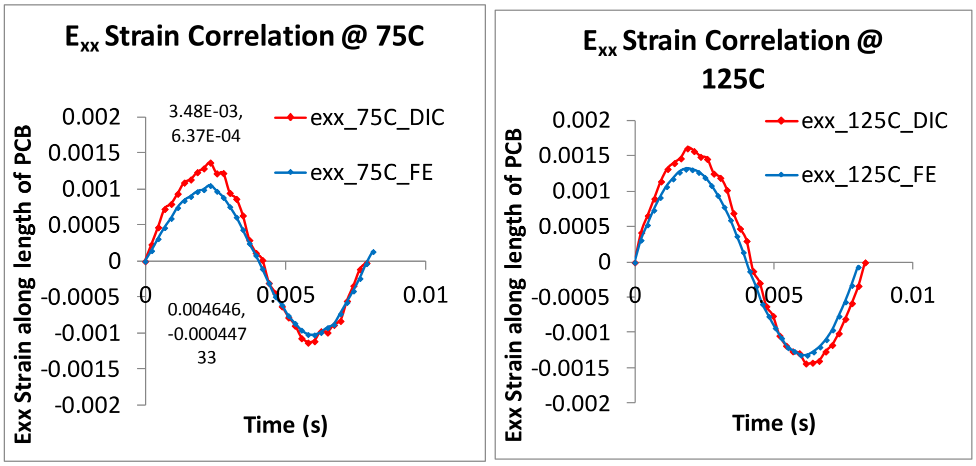

Figure 28: Correlation of PCB Out of plane displacement and in-plane strain

From the comparison of natural frequencies, mode shape out of plane displacements and in-plane strains, the global model can be said to correlate well with the test vehicle.

3.6 Failure modes

Typical failure modes observed on quad flat packages (QFPs) are lead deformation and lead cracking. This alludes to the fact that the weakest link in QFPs is the copper leads where the packages fail most frequently. FE results for QFP also indicate high stresses in the corner as well as mid-side leads [Figure 33]. The study is meant to investigate solder failures, therefore QFP failures have been disregarded. The TSOPS have failed at the solder joints without significant lead cracking though some lead deformation is observed in the corner leads. This indicates that TSOPs leads have high structural strength and the weakest link is the solder joint. Cross-sectioning of PBGAs reveals solder failure at corner balls. Figure 29 contains optical microscopic images of these failure modes.

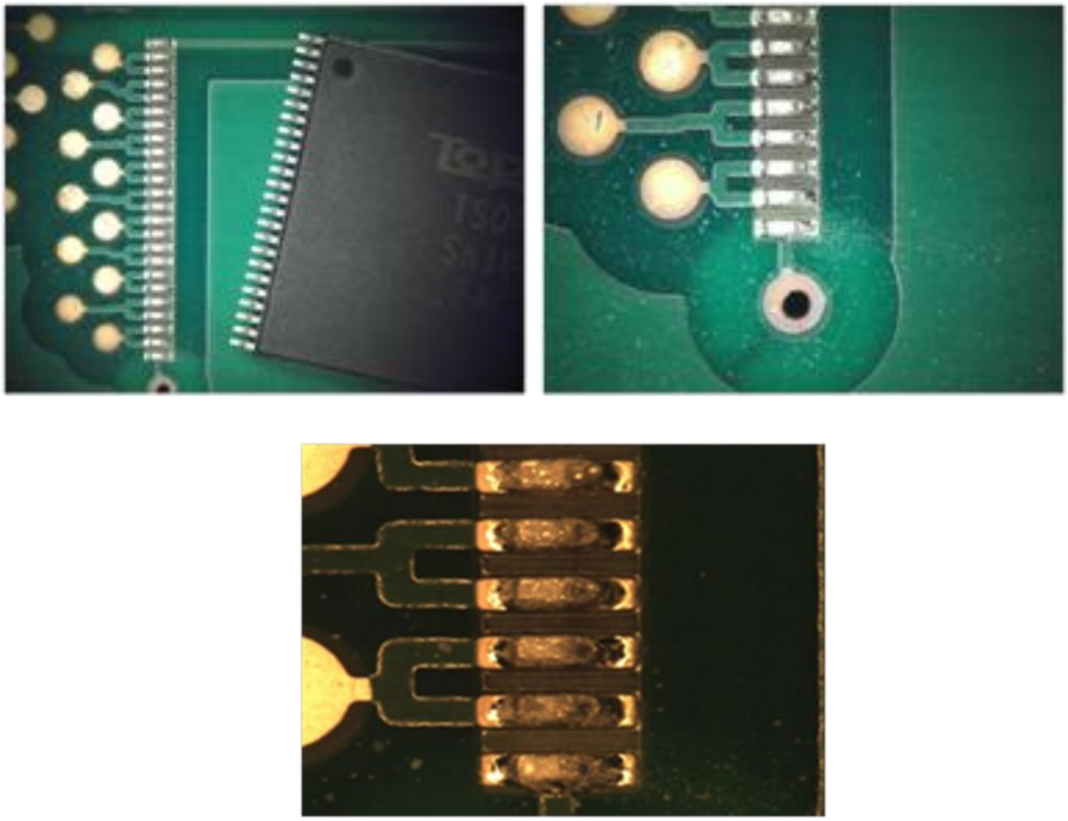

(a)

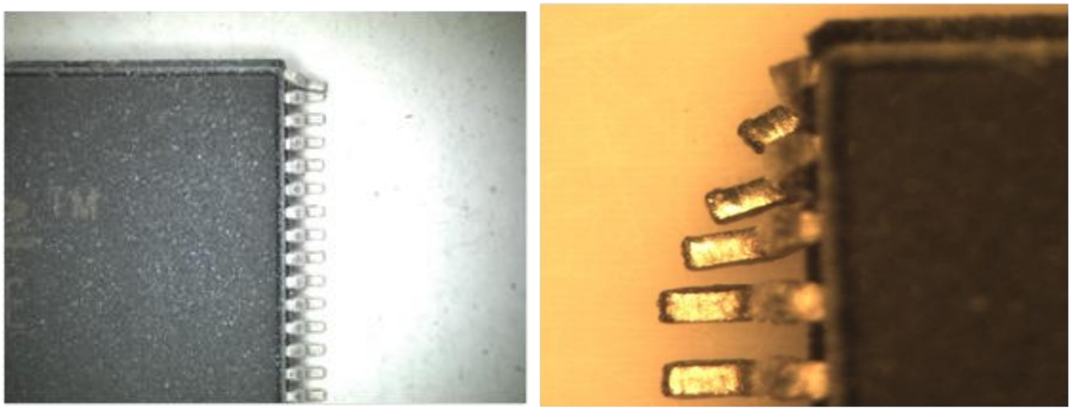

(b)

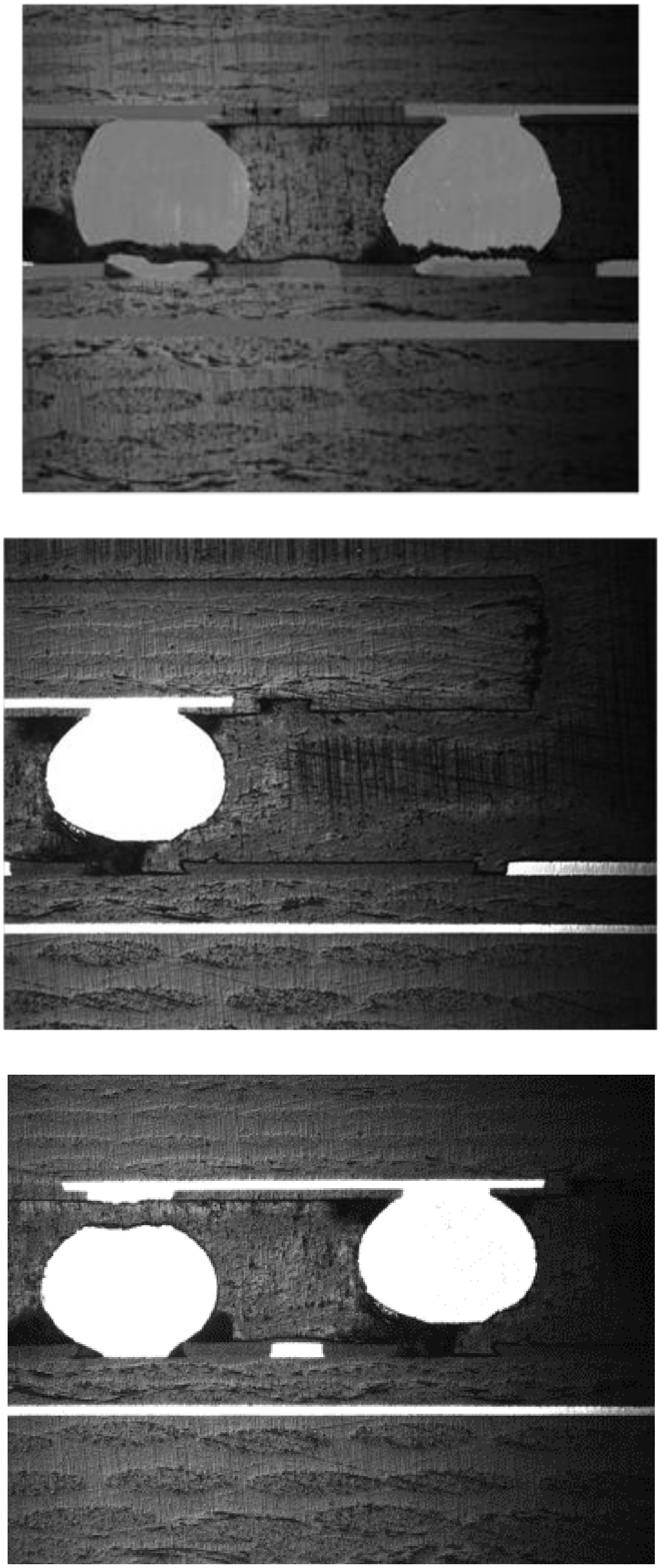

(c)

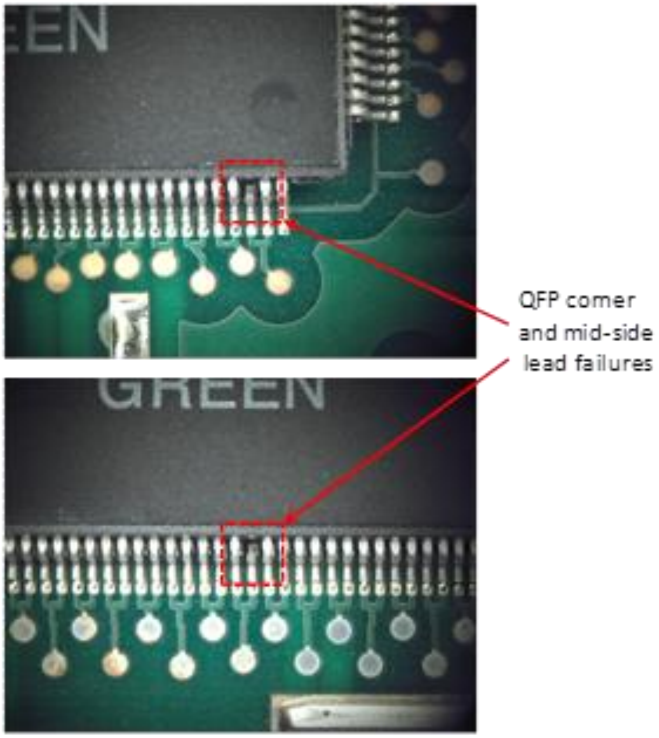

(d)

Figure 29: a)TSOP solder failure b)TSOP corner lead deformation c)Failure in BGA (corner solder failure) d)QFP lead failures

Cycles to failure differ for every package because it experiences different strain levels based on its location on the test board. The cycles to failure have been calculated by multiplying the time to failure by frequency of base excitation which is constant throughout the test. Typical resistance vs time plots are shown in Figure 30. Cycles to failure for each package as a function of test temperature are plotted in Figure 31. There is a difference in mean cycles to failure as the temperature is increased from 25C to 125C. Since the test vehicles were assigned randomly to a test case, the difference in mean cycles to failure can be attributed to test temperature.

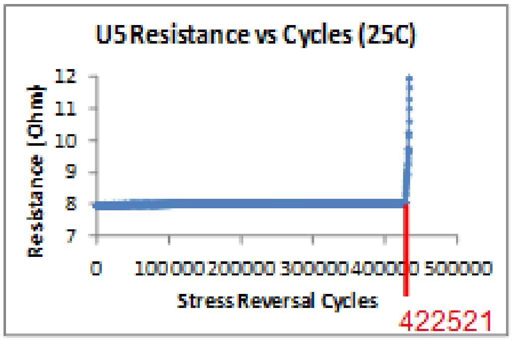
U5 Resistance vs Cycles (25C)
Resistance (Ohm)
12
11
10
9
8
7
0
100000
200000
300000
400000
500000
Stress Reversal Cycles
422521

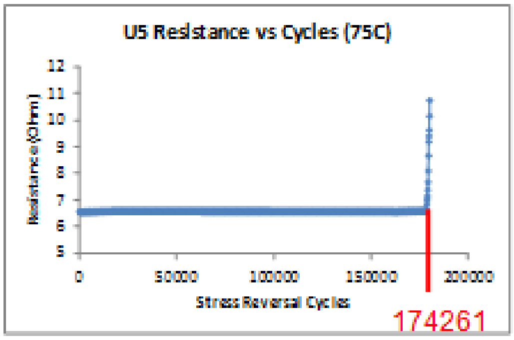
U5 Resistance vs Cycles (75C)
Resistance (Ohm)
12
11
10
9
8
7
6
5
0
50000
100000
150000
200000
Stress Reversal Cycles
174261

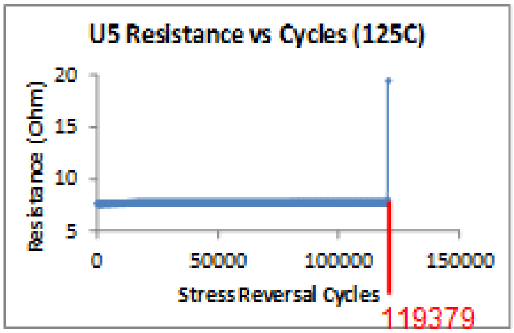
U5 Resistance vs Cycles (125C)
Resistance (Ohm)
20
15
10
5
0
50000
100000
150000
Stress Reversal Cycles
119379

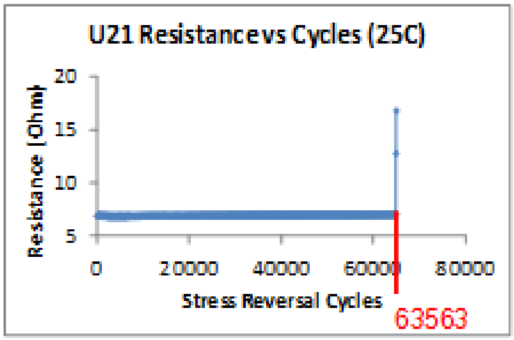
U21 Resistance vs Cycles (25C)
Resistance (Ohm)
20
15
10
5
0
20000
40000
60000
80000
Stress Reversal Cycles
63563

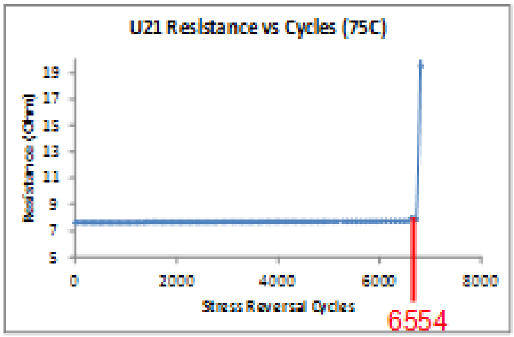
U21 Resistance vs Cycles (75C)
Resistance (Ohm)
19
17
15
13
11
9
7
5
0
2000
4000
6000
8000
Stress Reversal Cycles
6554

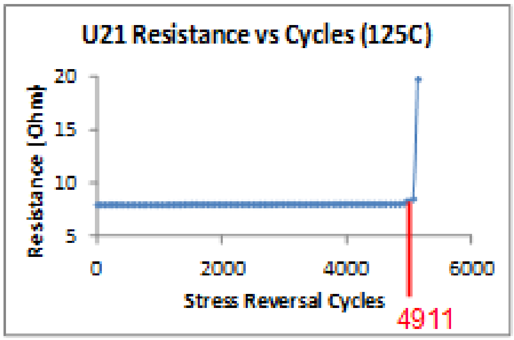
U21 Resistance vs Cycles (125C)
Resistance (Ohm)
20
15
10
5
0
2000
4000
6000
Stress Reversal Cycles
4911

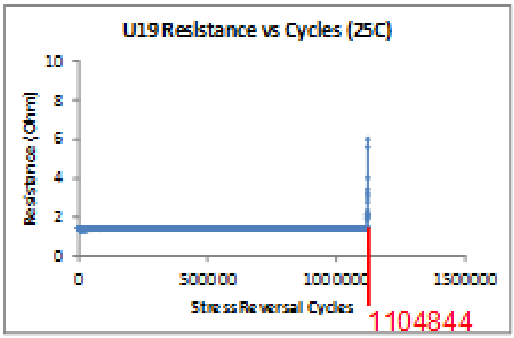
U19 Resistance vs Cycles (25C)
Resistance (Ohm)
10
8
6
4
2
0
0
500000
1000000
1500000
Stress Reversal Cycles
1104844

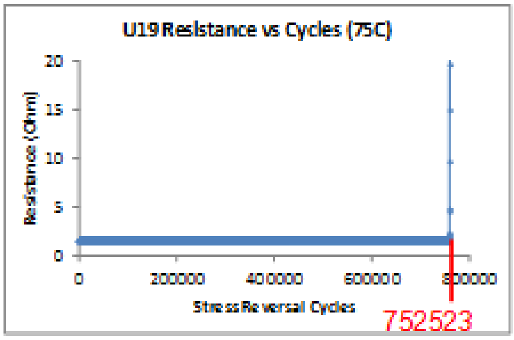
U19 Resistance vs Cycles (75C)
Resistance (Ohm)
20
15
10
5
0
0
200000
400000
600000
800000
Stress Reversal Cycles
752523

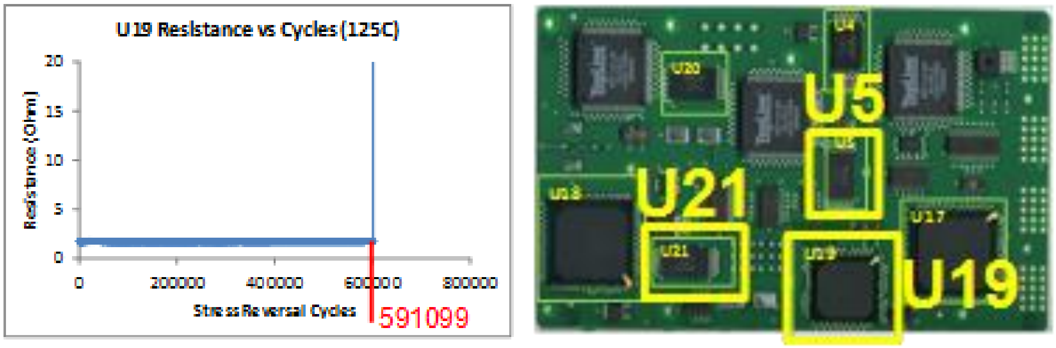

Figure 30: Resistance vs Cycles to failure

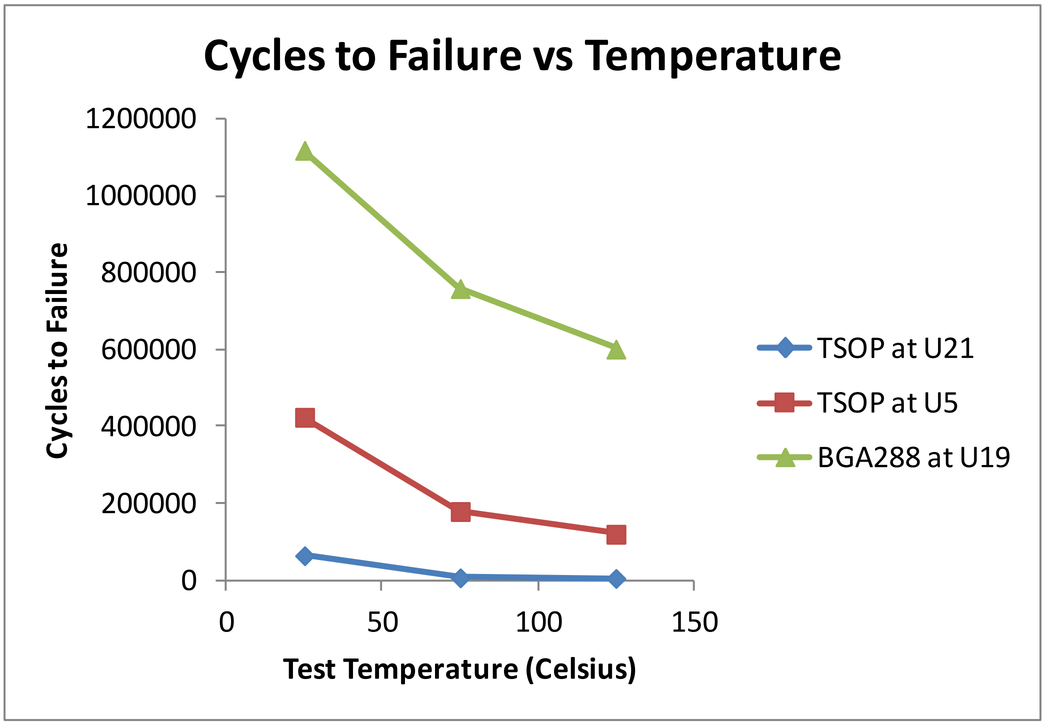

Figure 31: Difference in means of cycles to failure due to change in test temperature

3.7 Solder Stress Estimation from Explicit Sub-models

Explicit finite element models have been developed to model the vibration of the test boards. Model predictions have been used to determine the interconnect strain histories. Reduced integration elements have been used for computational efficiency, since the internal load vector scales with the number of integration points. Computational time of the dynamic event is reduced by incorporating reduced integration elements in the analysis because these element types use fewer integration points to form the element stiffness matrices. Lower order elements have been implemented since they perform better when the strain is large or very high strain gradient is expected during vibration cycle. Three-dimensional continuum elements C3D8R have been used to model the components layers of printed circuit board, substrate, mold, leads, lead-frame, solder, corner solder balls, die, die paddle and copper pad. In PBGAs, except the four corner interconnects, all remaining interconnects have been modeled as Timoshenko beam elements. Displacement boundary conditions of the sub-models are derived from the global model. Explicit dynamic analysis is conducted to obtain solder stresses. Solder material properties at the three test temperatures are tabulated in Table 8. The degradation in material properties is assumed to be in-line with other SAC alloys.

Table 8: Solder material properties

TEMPERATURE (CELSIUS)	ELASTIC MODULUS (GPA)	UTS (MPA)
25C	40	100
75C	30	90
125C	20	80

The solder interconnects experience tension-compression as well as shear stress in a vibration test. For fatigue life prediction, an equivalent stress of the solder interconnects needs to be considered. Therefore an equivalent stress called Von Mises stress is used for constructing the S-N curve. shows the stress contour in solder balls of BGA and TSOP. Volumetric average stress value is used in the region of solder/PCB interface so that mesh density does not have a significant effect on stress distribution. Solder stress levels for BGA and TSOP reduce with increase in temperature. High stresses are observed in corner solder ball at the PCB side. Similarly, high stresses are observed in corner leads and solder underneath these leads in TSOPs. The failure mode in BGA and TSOP obtained during tests is captured well in the simulation. [Figure 35, Figure 36]. is used to derive volume averaged stress.

$$\sigma_{avg} = \frac{\Sigma\sigma \times V}{\Sigma V} \tag{31}$$

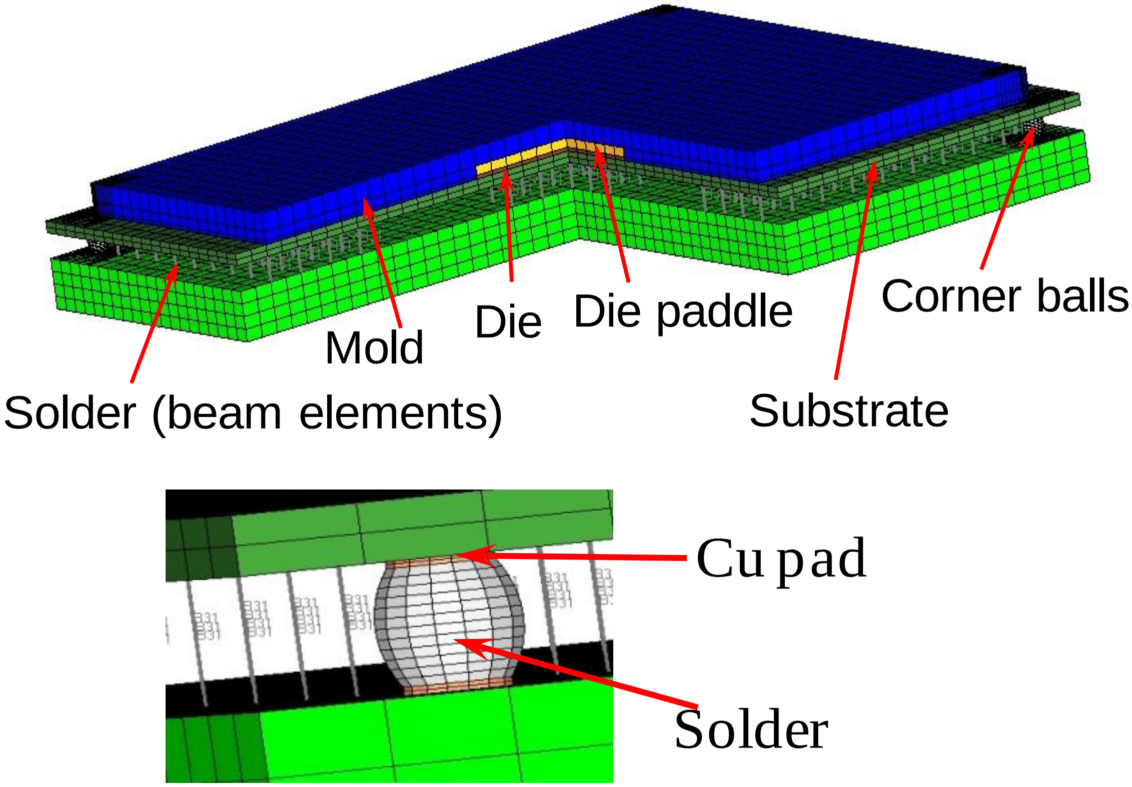

(a)

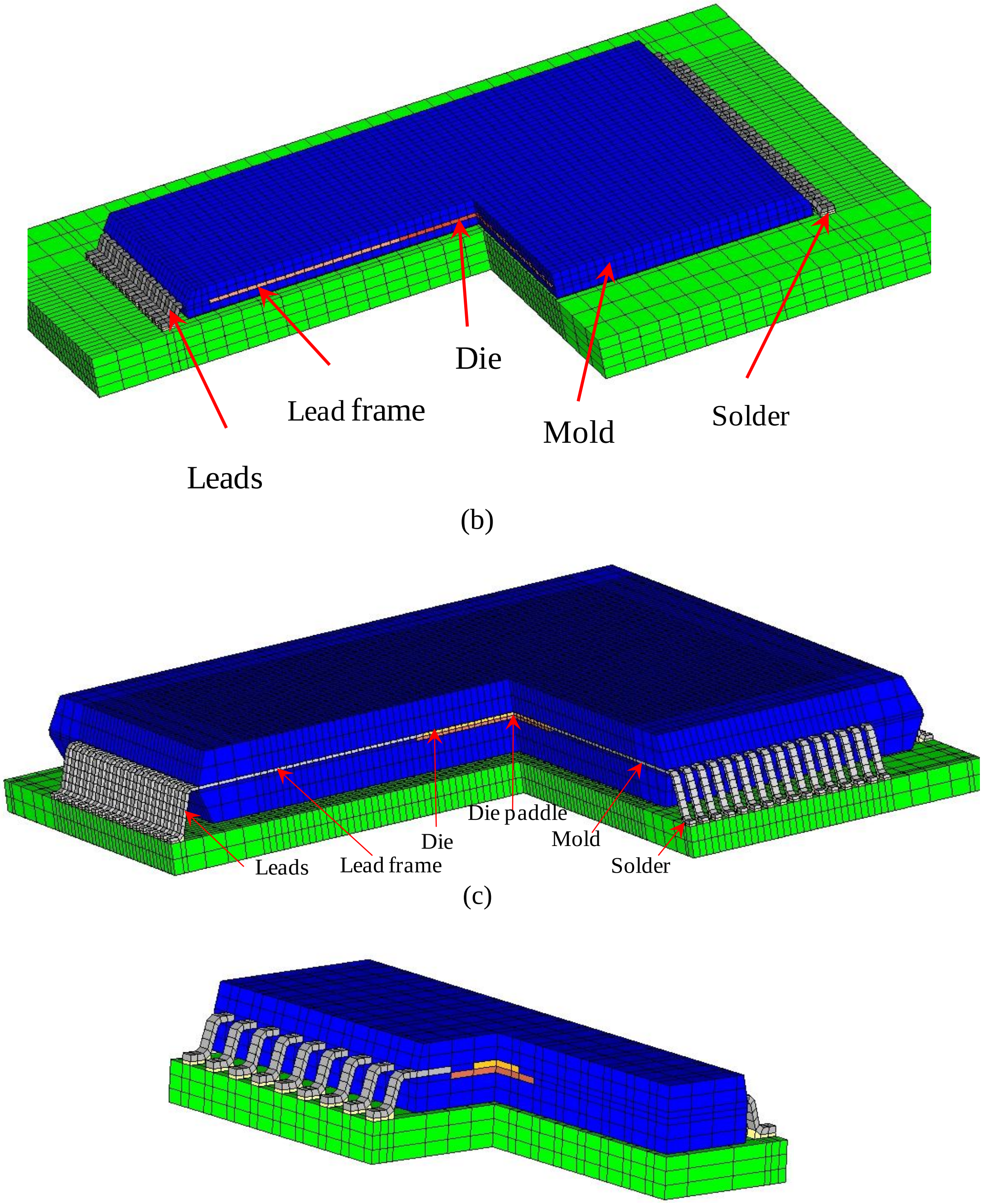

(b)

(c)

(d)

Figure 32: a) **BGA b) TSOP c) QFP d) SOL sub-models**

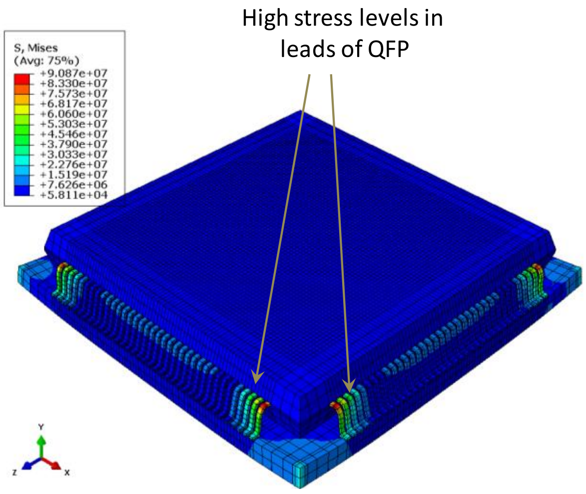

Figure 33: QFP high stresses in corner leads

Solder stress levels for BGA and TSOP reduce with increase in temperature. High stresses are observed in corner solder ball at the PCB side. Similarly, high stresses are observed in corner leads and solder underneath these leads in TSOPs. The failure mode in BGA and TSOP obtained during tests is captured well in the simulation. [Figure 35, Figure 36].

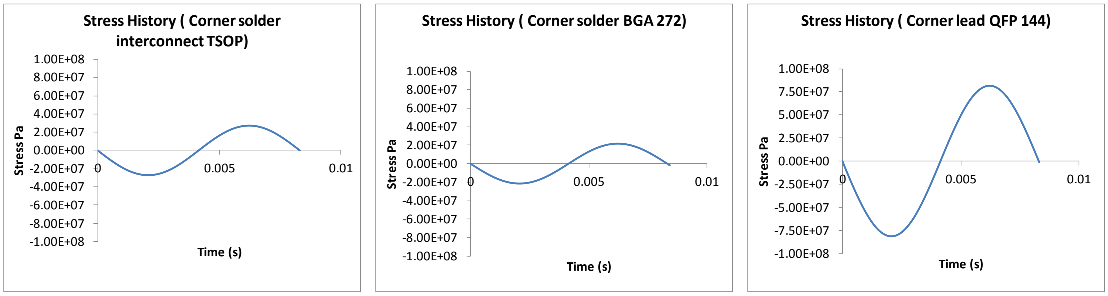

(a) (b) (c)

(b) Figure 34: Stress histories at 125C on a) TSOP corner solder b) BGA corner solder c) QFP corner lead

High cycle fatigue failure is characterized by Basquin power law relation:

$$\sigma_a = \sigma_f (2N_f)^b \tag{32}$$

where σ_a is the stress amplitude (MPa), σ_f is the fatigue strength coefficient (MPa), b is the fatigue strength exponent and ($2N_f$) are stress cycles to failure. The constants σ_f and b have been determined by substituting σ_a calculated from FE analysis and N_f from average cycles to failure for a component. For the 25C case, a value of σ_f =65.193MPa and b=-0.071 fits the data points with the R^2 value of 0.997. Prior researchers have published a value of σ_f =64.80622±50.16874 MPa and b=-0.14425±0.05501 [Yu 2011] for SAC305. These researchers have used a specially designed test vehicle with two daisy chained, symmetrically placed Amkor ball grid array (CTBGA 288) packages using SAC305 solder. The test vehicle is a 100mm by 50mm rectangle with two thicknesses of 0.6mm and 1mm. The test vehicle is subjected to sinusoidal vibration over a limited frequency band centered at the 1st natural frequency and Von-Mises stresses from FEA. The scope of this study is limited to room temperature tests.

Table 9 lists the fatigue coefficients published in literature for various solder alloys.

S-N curve obtained in this study is plotted on a log-log scale as shown in Figure 37. The procedure is repeated for all test temperatures to obtain two additional S-N curves. While the cycles to failure reduce with increase in temperature, the failure threshold also decreases with increase in temperature due to degradation of material properties [Figure 40].

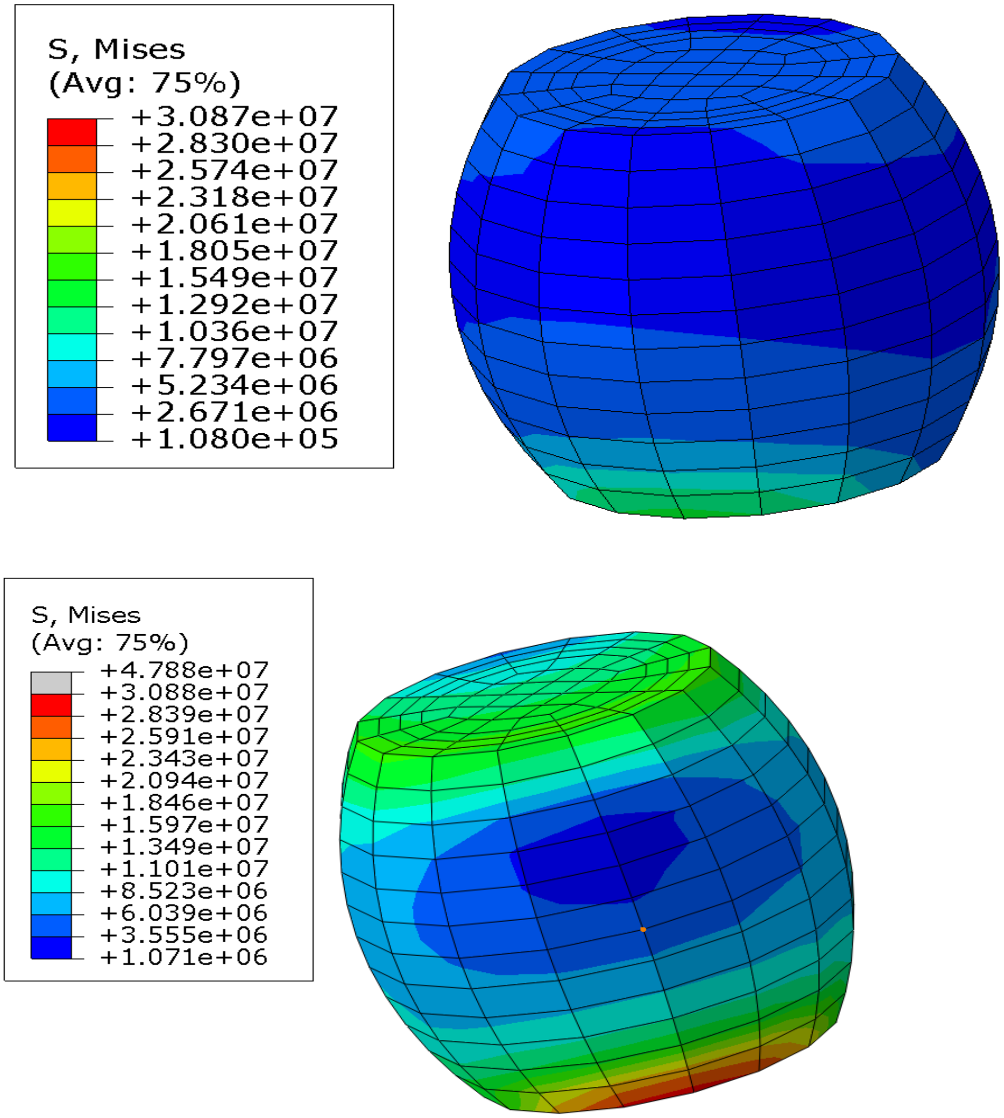

Figure 35: a) U19 Corner solder ball Mises stress distribution at 125C b)U19 corner solder stress distribution at 25C

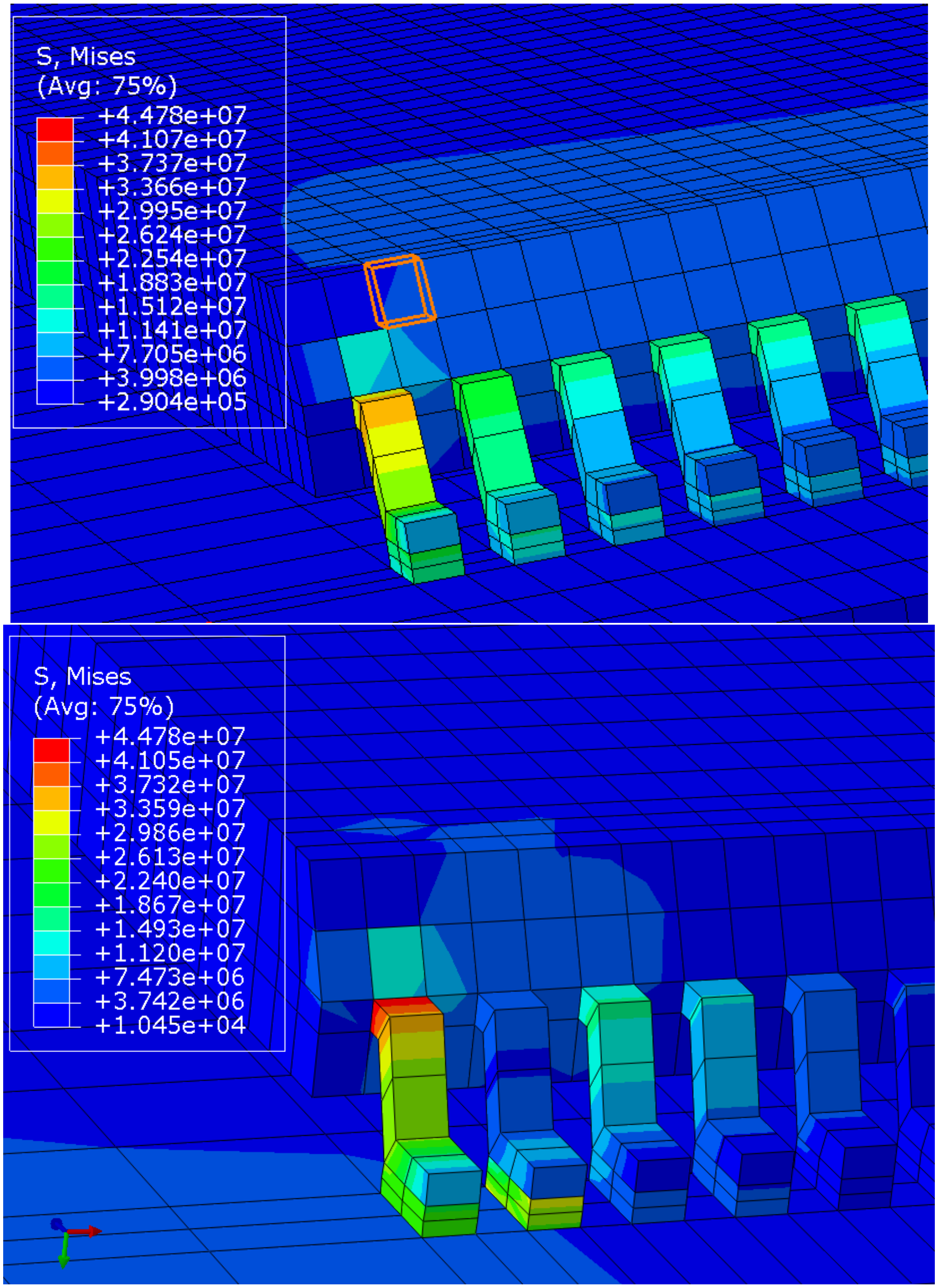

Figure 36: a) U5 Corner solder Von Mises stress distribution 125C b) U5 corner stress distribution at 25C

Table 9: Published values of Solder Fatigue constants

Author	Alloy	σ_f (MPa)	b	R^2
Yu 2011	SAC305	64.8	-0.1443	0.77
Yu 2011	SAC405	152.2	-0.2079	0.97
Mason 1964	63Sn37Pb	66.3	-0.12	-
Yao 1999	63Sn37Pb	177.15	-0.2427	-
Steinberg 2001	63Sn37Pb	109.6	-0.1	-

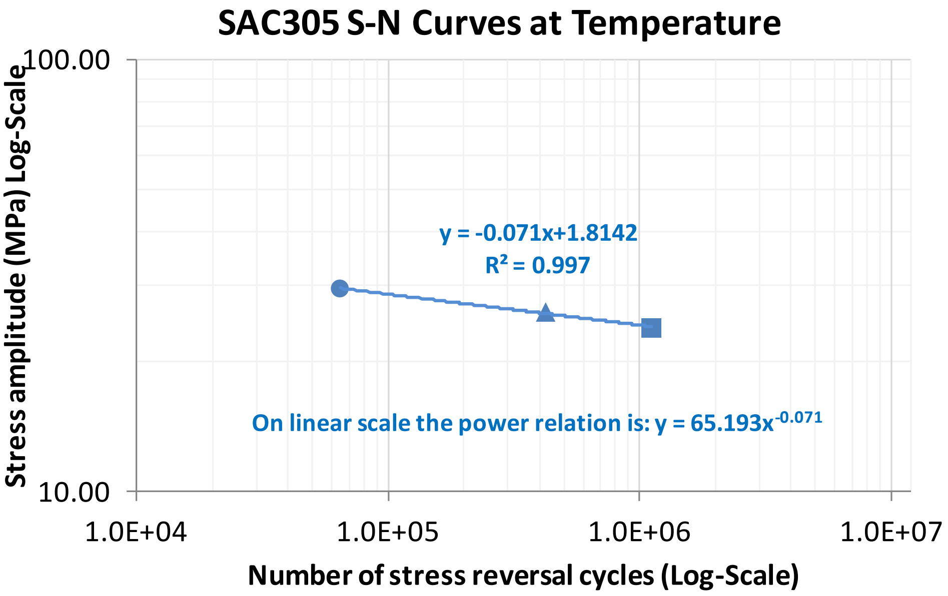

Figure 37: Curve fitting through S-N data at 25C

Table 10: Fatigue strength coefficient and exponent at temperature

Temperature (Celsius)	σ_f (MPa)	b
25	65.193	-0.071
75	47.797	-0.1
125	36.02	-0.113

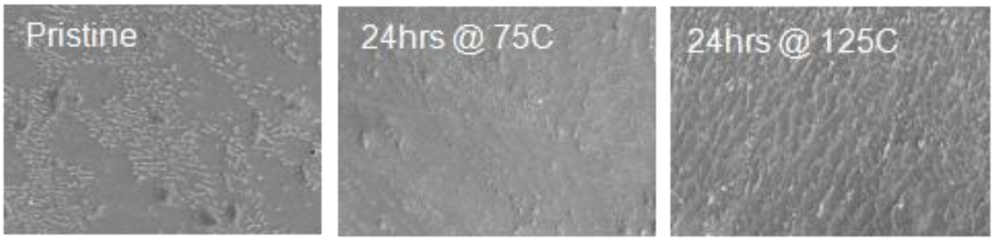

Figure 38: SAC305 phase growth [Lall 2012]

The coefficients σ_f and b evolve with temperature as shown in the table above. The fatigue coefficient and the fatigue exponent decrease with increase in temperature. The reduction in σ_f and b causes a shift in the S-N curves with increase in temperature as shown in Figure 40. This change can be attributed to the evolution of microstructure of SAC305. Figure 38 shows the evolution of phase structure as seen in SEM within just one day of aging at 75C and 125C [Lall 2004[a-d], 2005[a-b], 2006[a-f], 2007[a-e], 2008[a-f], 2009[a-d], 2010[a-j], 2011, 2012]. Based on Arrhenius theory, the relation between the fatigue strength coefficient and temperature is assumed to be of the form given by Eq. (33)

$$\sigma_{f,T} = \sigma_{f,0} \times e^{E_{A,\sigma f}/KT} \tag{33}$$

where $\sigma_{f,T}$ is the fatigue strength coefficient at temperature T Kelvin, K is the Boltzmann's constant and Ea, σ_f is the activation energy in eV. Taking natural log of both sides of Eq. (33) and then substituting the slope and intercept values from Figure 39 a:

$$\ln \sigma_{f,T} = \ln \sigma_{f,0} + \frac{E_{A,\sigma_f}}{KT} \qquad (34)$$

$$\ln \sigma_{f,T} = 1.8352 + \frac{700.39}{T} \qquad (35)$$

Taking antilog:

$$\sigma_{f,T} = 1.8352 \times e^{700.39/T} \qquad (36)$$

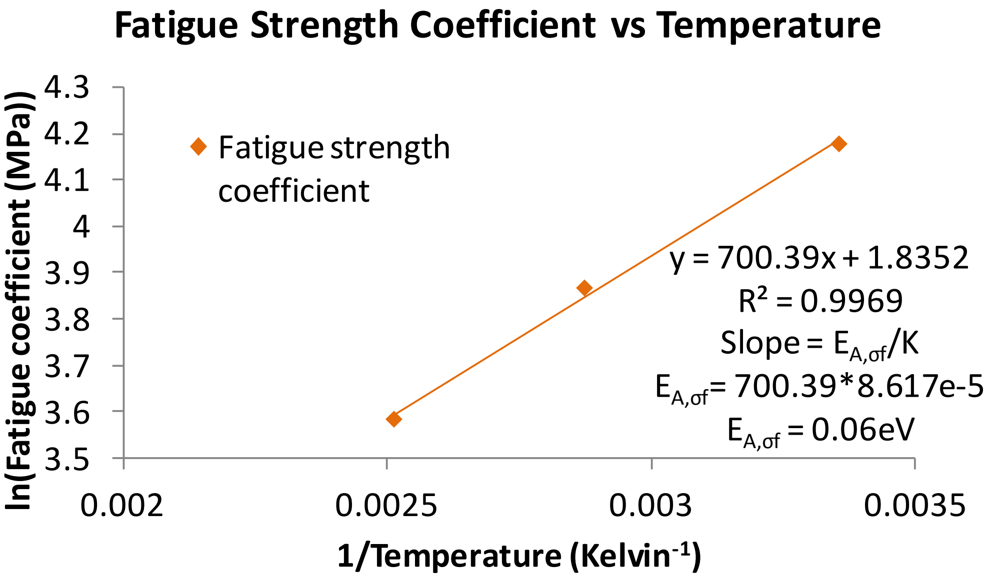

(a)

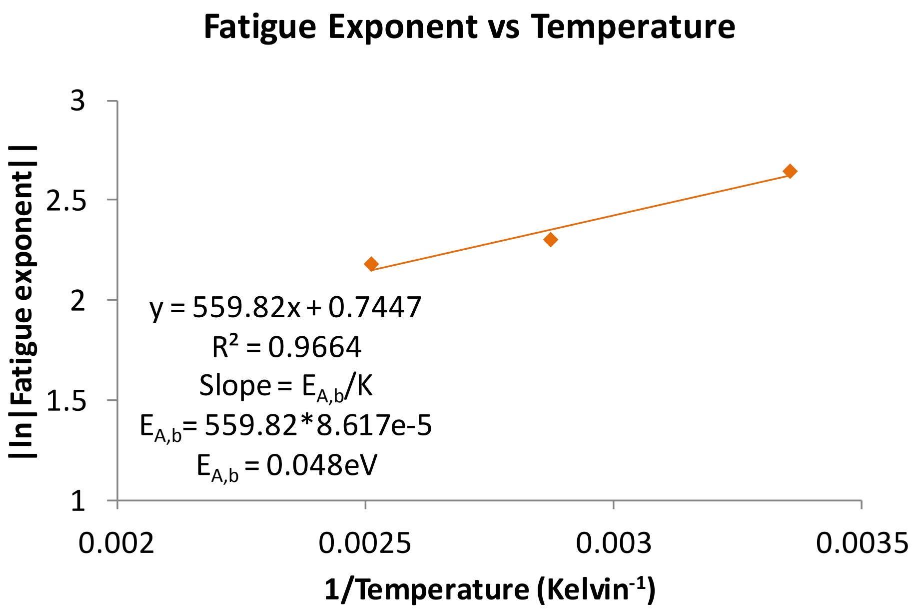

(b)

Figure 39: a)Fatigue coefficient as a function of temperature b)Fatigue exponent as a function of temperature

Similarly, considering the magnitude of fatigue coefficient b as a function of absolute temperature:

$$b_T = b_0 \times e^{E_{A,b}/KT} \tag{37}$$

Taking natural logarithm of both the sides,

$$\ln b_T = \ln b_0 + \frac{E_{A,b}}{KT} \tag{38}$$

Substituting slope and intercept from Figure 39b:

$$\ln b_T = -\left[0.7447 + \frac{559.82}{T}\right] \tag{39}$$

Taking into account the negative sign of the exponent,

$$b_T = -\left[0.475 \times e^{-559.82/T}\right] \tag{40}$$

Activation energy for the fatigue coefficient is 0.06eV. The activation energy for Sn-Pb solder creep found in literature is about 0.5eV for grain boundary creep and 0.84 eV for matrix creep [Knecht 1990]. To account for the effect of temperature in predicting the fatigue life of SAC305, Eq.(36) and Eq.(40) that give the temperature dependence of these parameters can be substituted in the Basquin power law relation given by Eq.(32)

$$\sigma_a = \left[\sigma_{f,T}\right] \cdot (2N_f)^{b_T} \tag{41}$$

Thus the high cycle fatigue life of SAC305 as a function of temperature can be expressed in terms of Basquin power relation as follows:

$$\sigma_a = \left[1.8352 \times e^{\frac{700.39}{T}}\right] \cdot (2N_f)^{-\left[0.475 \times e^{-559.82/T}\right]} \tag{42}$$

where σ_a is the stress amplitude in MPa, T is the test temperature in Kelvin and $2N_f$ is cycles to failure.

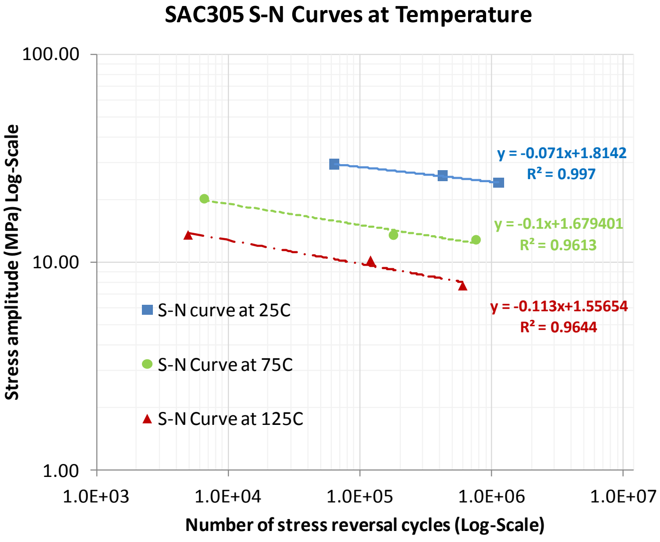

Figure 40: SAC305 S-N Curves at elevated temperature

3.8 Summary and Conclusions

First natural frequency of the test vehicle has been determined at three temperatures: 25C, 75C and 125C. It is observed to reduce linearly with increase in temperature. The material properties of the PCB have been investigated by tensile tests and DMA at elevated temperatures for FE simulation of global model. The FE based natural frequencies are compared with EMA. PCBs are tested to failure by subjecting to harmonic vibration, dwelling at the natural frequency for each test temperature. Cycles to failure are derived from the experiments for BGAs and TSOPs that fail at the solder. A reduction in mean cycles to failure is observed with increase in temperature for each component. The global FE model is correlated with the test vehicle using natural frequencies, mode shapes and out of plane displacement fields. Global model drives the detailed explicit sub-model of the components to output solder Von Mises stresses with material property degradation at temperature. Volume averaged solder stresses at high stress location of every component is plotted against its experimentally obtained cycles to failure. S-N curves for SAC305 are obtained based on Basquin power law relation between stress amplitude and stress reversal cycles. S-N curves at 25C, 75C and 125C are thus obtained for SAC305. The temperature dependence of the fatigue strength coefficient and fatigue exponent have been implemented in the SAC305 S-N curve relation using Arrhenius theory. The temperature dependent fatigue coefficient and fatigue exponent are implemented in Basquin power relation. This study assumes that the effect of change of strain rate due to different temperature dependent test frequency (difference of 12Hz) does not have any effect on the fatigue life of the solder.

CHAPTER 4

EFFECT OF HIGH STRAIN RATE AND AGING ON MATERIAL CHARACTERIZATION OF INNOLOT

4.1 Introduction

With the ROHS initiative on lead-free solder taking effect, the electronics industry has been presented with a wide array of lead-free options. Most of the Pb-free alloys in the industry today are plagued by aging and creep issues. Prior researchers have shown a deterioration of the material properties of SAC alloys with constant temperature aging (Lall 2012, Ma 2009, Zhang 2009, Darveaux 2005). New developments in the Pb-free options have introduced small proportions of Ni, Zn, Co, Bi, Sb in the SAC alloys to increase resistance to aging and creep while maintaining the melting temperature and strength of the alloy comparable to SAC. Many researchers have shown enhanced material properties, microstructures and resistance to failures in thermal cycling due to the addition of rare earth elements in SAC alloys [Zhang 2009, Liu 2007, Wu 2004, Kim 2003, Huang 2000]. InnoRelTM have introduced a new Pb-free alloy- Innolot, which consists of Ni, Sb and Bi in its composition (Table 2). This alloy has a melting range between 206C to 218C. Increased creep strength is a result of solid solution hardening and dispersion hardening mechanisms achieved by Bi, Sb dissolution in Sn crystal matrix and intermetallic phases by Ni. Prior studies have shown that Innolot is more reliable in thermal cycling as compared to SAC alloys [Miric 2010].

The effects of aging on the microstructure and material properties of Pb-free alloys have been investigated at low strain rates less than 1/s [Chuang 2002, Coyle 2000, Darveaux 2005, Lee 2002, Pang 2004, Tsui 2002, Zhang 2009]. For high strain rate constitutive behavior investigation, researchers have relied on Split Hopkinson Pressure bar tests [Chan 2009, Siviour 2005]. The strain rates achievable with this equipment, range from 500/s to 3000/s. In practice, the typical strain rates observed on second level interconnects in consumer electronics drop impacts are within 1/s to 100/s. Neither the Split Hopkinson Pressure bars nor conventional pull tester can be easily used to obtain these strain rates. Very few researchers have characterized Pb-free solder properties at strain rates of 1/s to 100/s [Lall 2011, 12, Meier 2009, Wong 2008]. The authors of this paper have explicitly demonstrated the capability of an innovative tensile tester to repeatably obtain constant strain rates of 10/s, 35/s and 50/s. The effect of strain rate and aging on the material properties of SAC105 and SAC305 has been established through this work [Lall 2012]. In this paper, the same equipment and aging conditions have been used for two strain rates of 10/s and 35/s to characterize the constitutive behavior of Innolot. A comparison of the effects of strain rate and aging on Innolot and SAC alloys (SAC105 and SAC305) has been presented.

Non-linear Ramberg-Osgood model [Lall 2012, Nguyen 2011, Ohguchi 2006, Chen 2006, Muller 2005, Pang 2004, Park 2002, Lee 1997, Knechet 1990] and Anand’s viscoplastic model [Mysore 2009, Bhate 2008, Yeo 2006, Pei 2005, Rodgers 2005, Wang 2005, Pand 2004, Wang 2001, Wilde 2000] are amongst the most popular models to describe solder stress-strain behavior. Prior researchers have used finite element analysis for modeling tensile tests [Lall 2012, Joun 2007, Niordson 2004, Cabezas 2004, Peng 2004, Koc 2004, Mirone 2004, Tang 2003, Inal 2002, Komori 2002, Nilsson 2001]. This research, uses Ramberg-Osgood model for its relatively simple implementation in Abaqus based FE codes.

In the past, Digital Image Correlation (DIC) has been used for material characterization at low strain rate testing of conposites [Gershon 2010, Srinivasan 2005, Grytten 2009] and high strain rates for lead-free solder characterization [Lall 2012, 2011, 2010, Tiwari 2005] to investigate full-field displacement and strain contours as the test specimen deforms and fractures. DIC has been implemented in this work to correlate Ramberg-Osgood FE models with the experimental data.

Table 11: Innolot Composition [Miric et. al. 2010]

Element	**Min %**	**Max %**
Sn	Balance (90.1-91.6)	
Ag	3.6	4.0
Cu	0.6	0.8
Ni	0.1	0.2
Sb	1.3	1.7
Bi	2.8	3.2

4.2 Test specimen preparation

The test specimens used for the high strain rate tensile tests are thin rectangular bars 40mm (length) X 5mm (width) X 0.5mm (thickness). The cross-sectional thickness of 0.5mm is selected to corresponding to the height of second level solder interconnects specifically in BGAs. To prepare the test specimen, small pieces of bulk solder are molten in a glass crucible kept in a soldering pot. Rectangular, hollow glass tubes with very high dimensional precision are fabricated in advanced glass-shops to form the solder specimens. One end of the glass tubes is dipped in the molten solder and a suction pressure upto 600mm Hg is applied at the other end. As a result of capillary action and suction pressure, the molten solder from the crucible rises in the glass tube. Once the solder rises upto the desired level, the control valve of the pump is cut off and the glass-tube is quenched in water to allow the specimen to solidify [Figure 41]. The specimens in the glass tube are reflowed using the profile shown is Figure 44. Thermocouples attached to the glass tubes mapped this reflow temperature profile using a radio-frequency KIC temperature profiling system. This profile is typical for commercial lead-free solders across the industry. Figure 42 and Figure 43 show a typical tensile specimen and its X-ray image. X-ray and optical microscopic images of every sample have been taken to ensure the absence of voids and premature cracks in the gage length of specimens. After reflow, the specimens are stored in isothermal chamber ovens for a desired length of aging time. Prior to the test, the glass tube is gently broken using a vice to take out the solder specimen. A thin white coat of paint is applied to the solder specimen and a random black speckle pattern is created to enable Digital Image Correlation. For pristine cases, tests are conducted within five hours after reflow to minimize the effects of room temperature aging.

Figure 41: Setup for Innolot tensile specimen preparation [Lall et. al. 2012]

Figure 42: Innolot tensile specimen

Figure 43: X-ray image of specimen

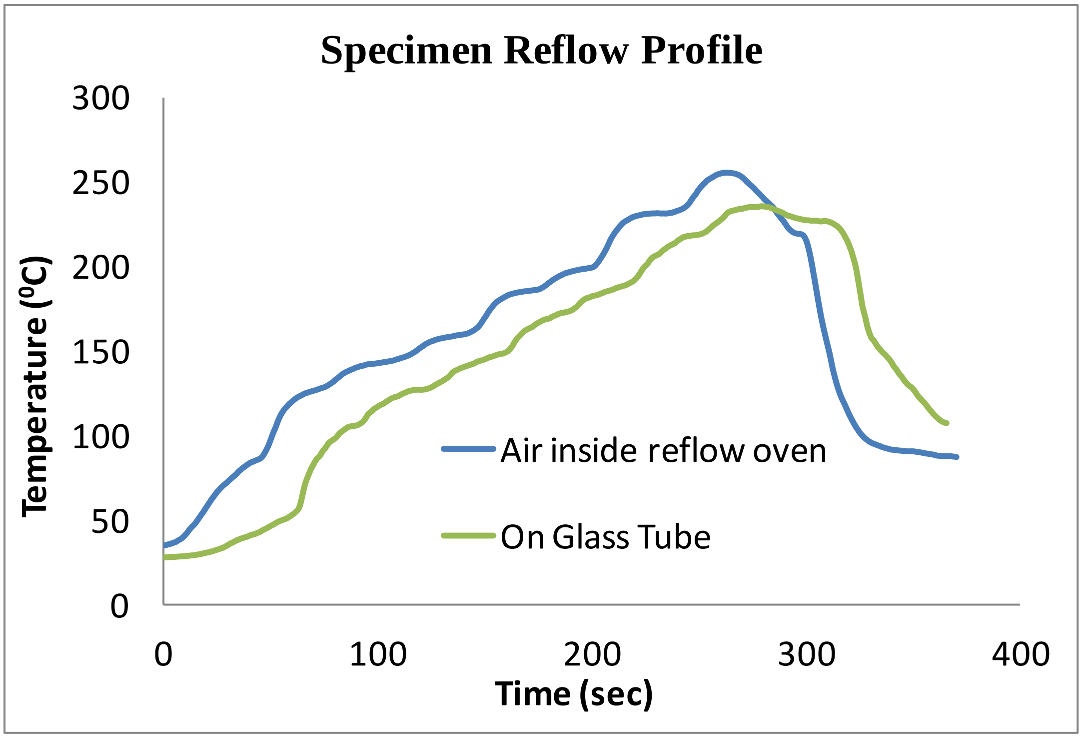

Figure 44: Reflow profile for specimen preparation [Lall et. al. 2012]

4.3 Test setup

An innovative tensile tester manufactured in-house has been used to facilitate cross-head strain rates in the range of 1/s to 100/s. It incorporates an impact hammer-like action where the hammer can have variable mass and drop height to achieve the desired cross-head strain rate. The specimen is mounted between two cross-heads. The top cross-head is rigidly fixed and houses the piezoelectric load sensor. The bottom crosshead is mounted on a slip-joint.

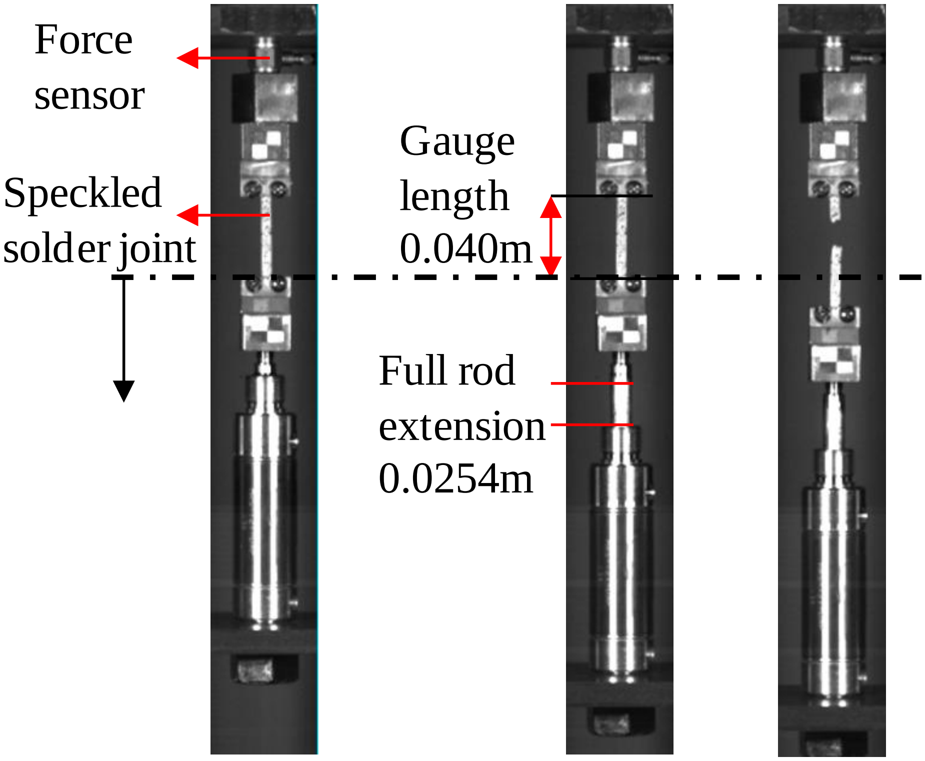

$T_0 = 0$ sec (At rest)

$T_1 > T_0$ (zero specimen elongation up to complete slip joint extension)

$T_2 > T_1$ (specimen pulled at constant high velocity)

Figure 45: Implementation of slip joint mechanism to achieve constant cross-head velocity after impact [Lall, P., Shantaram, S., Suhling, J., Locker, D., ECTC, 2012]

The slip joints extends non-linearly due to the impact of the hammer and subsequently causes a linear (constant velocity and constant strain rate) extension of the bottom cross-head. The solder specimen thus experiences a constant strain rate extension. High speed cameras capture the specimen deformation upto failure to obtain full field strain contours using DIC. Very high speed oscilloscope records the force data from the load sensor during the specimen failure. Figure 45 illustrates the initial configuration of the tester. In the second image of Figure 45 the impact hammer has hit the intermediate plate. This impact initiates the extension of the slip join as shown. Note that the bottom crosshead is still at the initial position and there is no deformation of the specimen. After the complete extension of this slip joint of 25.4mm, the bottom cross-head moves downwards pulling the solder specimen attached on top of it [Figure 45].

Figure 46 illustrates the initiation of slip-joint motion due to the impact hammer. Point 1 is a point on the fixed reference datum. Point 2 is on the impact hammer that drops and hits the intermediate plate labeled ‘Contact’. Point 3 is on the base of the slip joint.

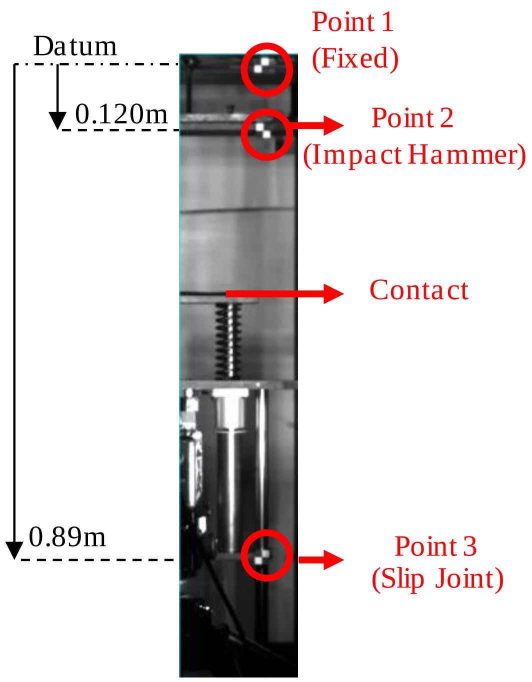

Figure 46: Impact mechanism [Lall et. al. 2012]

To illustrate that constant strain rate is obtained at the slip joint repeatedly, the motion of the targets is captured and analyzed for the 35/s case. The plot in Figure 47 is obtained using high speed imaging in conjunction with motion tracking software to obtain the displacement histories of these target points on the tensile tester. The continuous green line plot in Figure 47, corresponds to the relative position of the impact hammer. As expected, the initial section of this is parabolic due to the near-free-fall of the impact hammer. As the hammer hits the intermediate plate, the motion of the slip-joint below the bottom cross-head is initiated. The dotted line denotes the motion of the slip joint. Figure 48a, shows that though the initial section of slip joint extension was non-linear, the cross-head displacement, which initiates only after the complete (0.0254m) extension of slip joint, is very linear. Figure 48b gives the cross-head strain as a function of time. It can be seen that a constant strain rate of 35/s is achieved at the cross-head. For every test, the specimen gets pulled at the same desired strain rate. Similar plots and repeatability is observed for 10/s strain rate achieved by altering the mass and drop height of impact hammer.

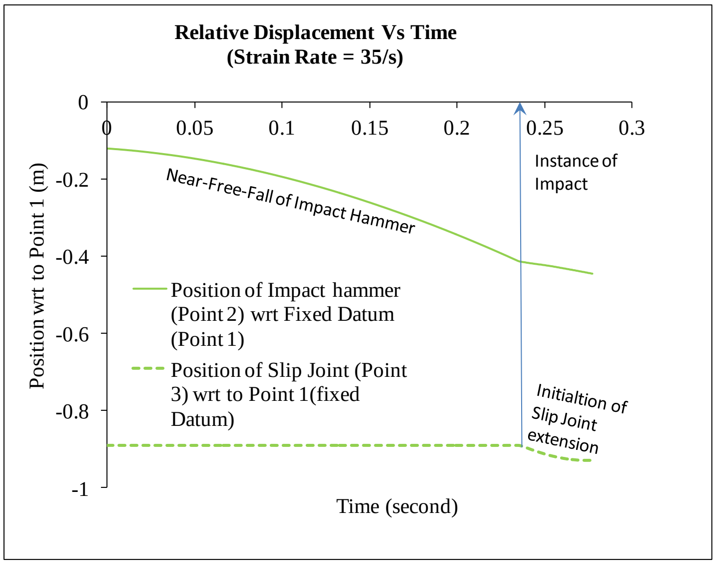

Figure 47: Position vs time plots of target points on the tester [Lall et. al. 2012]

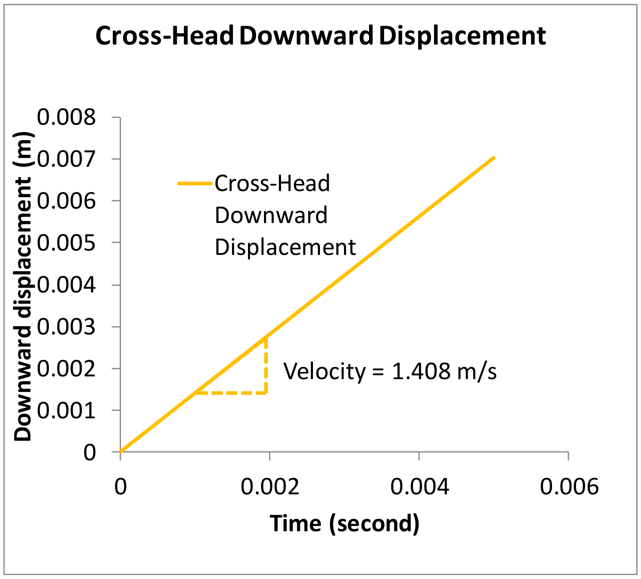

(a)

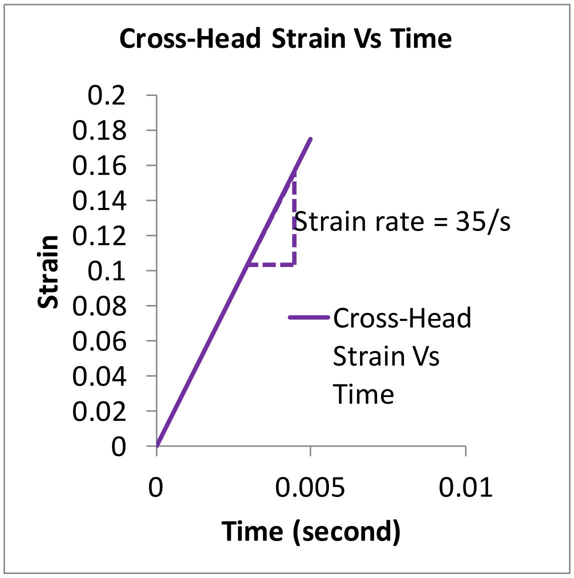

(b)

Figure 48: Cross-Head: a) Displacement b) Strain [Lall, et. al. 2011]

4.4 Test matrix

Table 12 shows the test matrix. Two strain rates 10/s and 35/s have been used for the tensile tests. Along with this isothermal aging at 50C for three durations has been employed – 1day, 30days and 60day. Table 12 illustrates the test cases. All the tests were conducted at room temperature which is maintained at 25C. The test temperature and strain rates are selected to facilitate comparisons with SAC105 and SAC 305 alloys conducted previously by these authors.

Table 12: Test Matrix for Innolot

Aging duration at 50C	**Strain rate 10/s**	**Strain rate 35/s**
1day	X	X
30 days	X	X
60 days	X	X
Pristine (no aging, within 5 hours after reflow)	X	X

4.5 Results and Discussion

4.5.1. High Strain Rate Tensile Testing

Thin rectangular bars of 40mm (length), 5mm (width), 0.5mm (thickness) are prepared from Innolot by the procedure described earlier in this paper. Reflow profile is maintained similar to commercial reflow profile used for Pb-free components. Data measured from multiple samples for every case is averaged to obtain the material response under every condition.

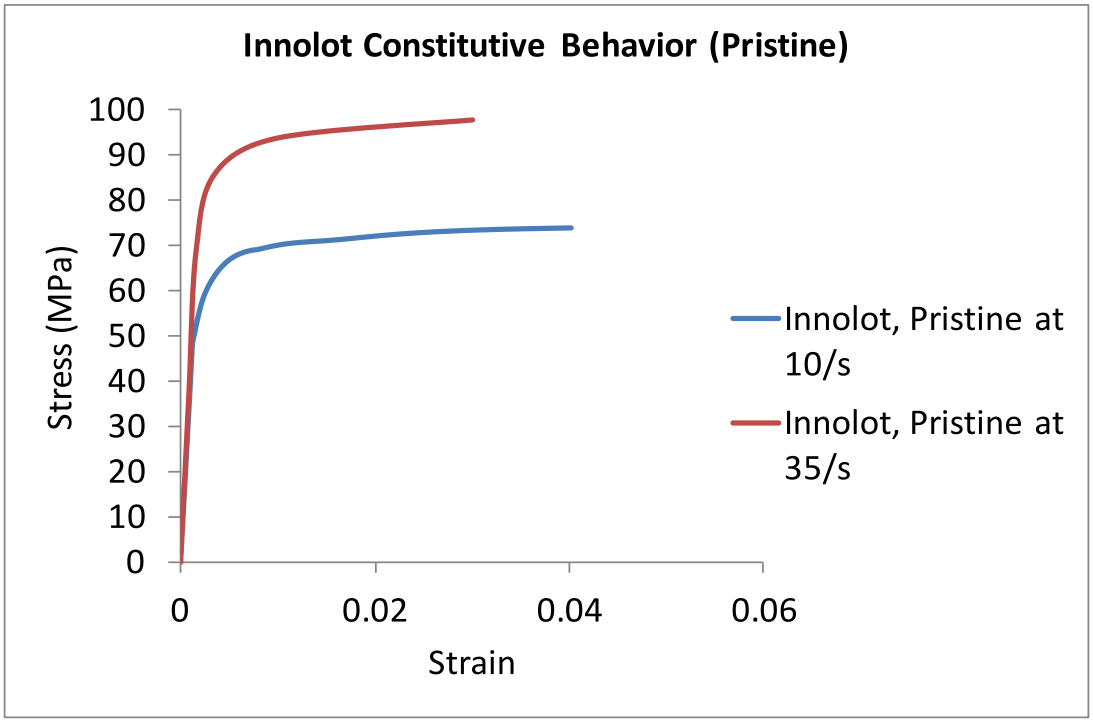

Figure 49: Stress-strain curves for Pristine Innolot

Table 13: Material Properties for Innolot, Pristine

Strain Rate (per second)	**E (GPa)**	**UTS (MPa)**
10	39.3	73.8
35	43.5	98

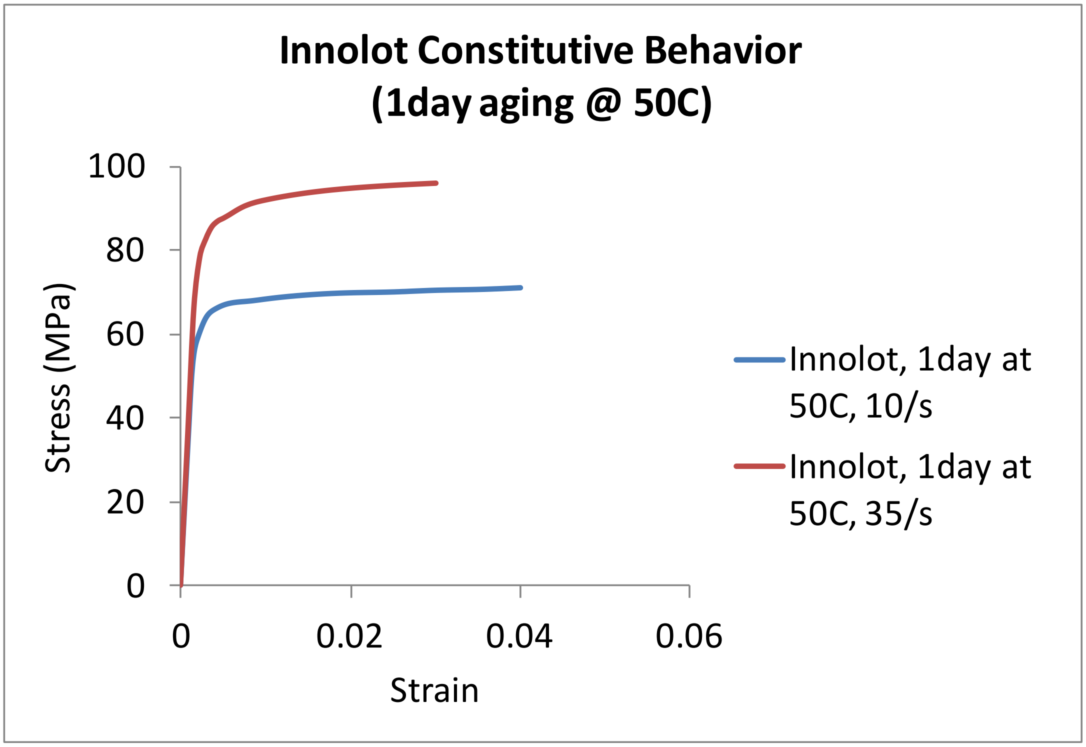

Figure 50: Stress-strain curves for Innolot aged at 50C for 1 day

Table 14: Material Properties for Innolot, 1day aging at 50C

Strain Rate (per second)	**E (GPa)**	**UTS (MPa)**
10	38.4	71.2
35	42.1	96

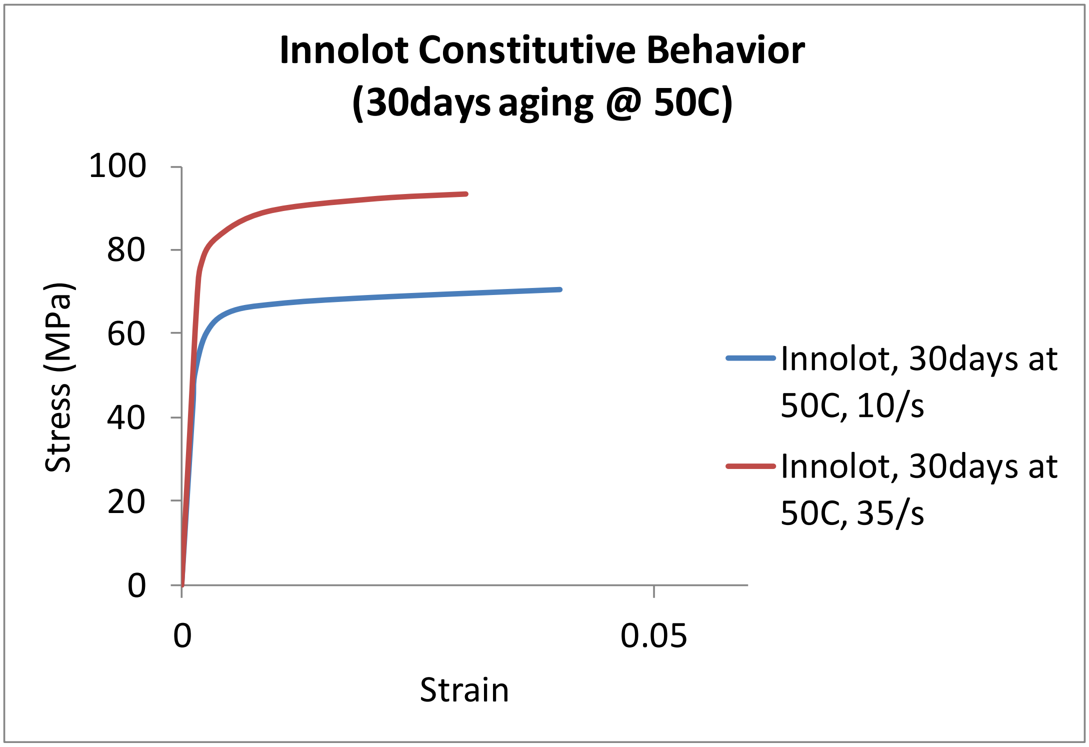

Figure 51: Stress-strain curves for Innolot aged at 50C for 30 days

Table 15: Material Properties for Innolot, 30 days aging at 50C

Strain Rate (per second)	E (GPa)	UTS (MPa)
10	36.01	70.4
35	41.7	93.2

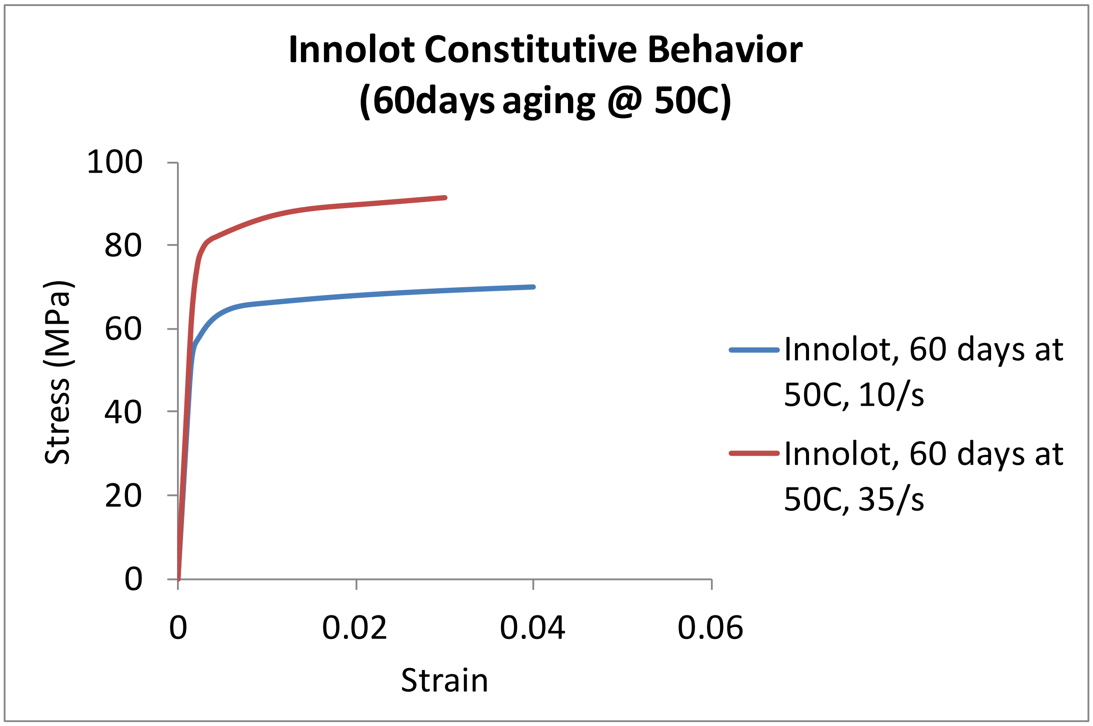

Figure 52: Stress-strain curves for Innolot aged at 50C for 60 days

Table 16: Material Properties for Innolot, 60 days aging at 50C

Strain Rate (per second)	**E (GPa)**	**UTS (MPa)**
10	35.63	70.02
35	41	91.7

4.5.2. Effect of 1 day Aging at 50C

The specimens are prepared and reflowed as discussed previously. After reflow, the specimens are aged by storing in an isothermal chamber set at 50C. Randomly selected specimens are taken out of the isothermal chamber after 1 day and tested at strain rates of 10/s and 35/s. Figure 50 shows the stress-strain curves of Innolot aged at 50C for 1 day. It can be seen that the mean elastic modulus and ultimate tensile strength of the specimens reduce from pristine values tabulated in Table 13. However, at 10/s, the elastic modulus reduces by 0.9GPa and the UTS reduces by 2.6MPa. Likewise at 35/s the elastic modulus reduces by 1.4GPa and UTS by 2MPa. The small reductions in both elastic modulus and UTS may be attributed to reduced stiffness of the material due to 1 day exposure to 50C. Table 19 compares the reduction of elastic modulus due to 1 day aging at 50C in Innolot, SAC105 and SAC305. Considering the elastic modulus in the pristine cases as baseline, it can be noted that the percent reduction in the elastic modulus of Innolot is 2.29% and 3.22% for the two strain rates which is much less than SAC305 (11.44% and 13.28%) and SAC105 (6.15% and 3.88%) for the same pre-conditions.

4.5.3. Effect of 30 days Aging at 50C

Figure 51 shows the stress-strain curve of Innolot after 30 days exposure to isothermal aging at 50C. Comparing the properties in Table 15 with the pristine properties in Table 13 and 1 day aged properties from Table 14, it can be inferred that aging continues to degrade the properties of Innolot after 30 days at 50C for both the strain rates. The pristine elastic modulus at 10/s is 39.3GPa and reduces to 36.01 GPa while the pristine elastic modulus at 35/s is 43.5GPa and reduces to 41.7GPa after 30 days at 50C. The pristine UTS at 10/s is 73.8MPa and reduces to 70.4MPa while the pristine UTS at 35/s is 98MPa and reduces to 93.2MPa after 30 days at 50C. Although there is considerable degradation in the material properties of Innolot under these conditions, a comparison with SAC alloys shows that the effect of isothermal aging on Innolot is much less pronounced. Table 19 shows that the elastic modulus of Innolot reduces by 8.37% and 4.14% at the two strain rates after 30 days at 50C. For the same aging, the reduction in elastic modulus of SAC105 is 35.4% and 31.94% and for SAC305 is all the way up to 40.3% and 39.41%. Table 20 shows that the UTS of Innolot reduces by 4.6% and 4.9% at the two strain rates after 30days at 50C. For the same aging, the reduction in UTS of SAC105 is 11.71% and 17.47% and for SAC305 is 8.51% and 12.5%

4.5.4. Effect of 60 days Aging at 50C

Figure 52 shows the stress-strain curves of Innolot after 60 days of isothermal aging at 50C. Table 16 lists the elastic modulus and UTS corresponding to the two curves in Figure 52. Comparing Table 15 and Table 16, there is only a small reduction in the elastic modulus and UTS for both strain rates. This implies that there is not much difference in the material properties of Innolot after 30 days of aging at 50C and 60 days of aging at 50C. Comparing with SAC alloys (Table 19), after 60 days of aging the elastic modulus of Innolot reduces by 9.34% and 5.75% for 10/s and 35/s respectively. For the same conditions, the elastic modulus of SAC105 reduces by 37.5% and 36.42% and SAC305 reduces by 43.28% and 41.08%. Table 20 shows that the UTS of Innolot reduces by 5.12% and 6.43% at the two strain rates after 60 days at 50C. For the same aging, the reduction in UTS of SAC105 is 14.99% and 20.39% and for SAC305 is 9.7% and 13.9%

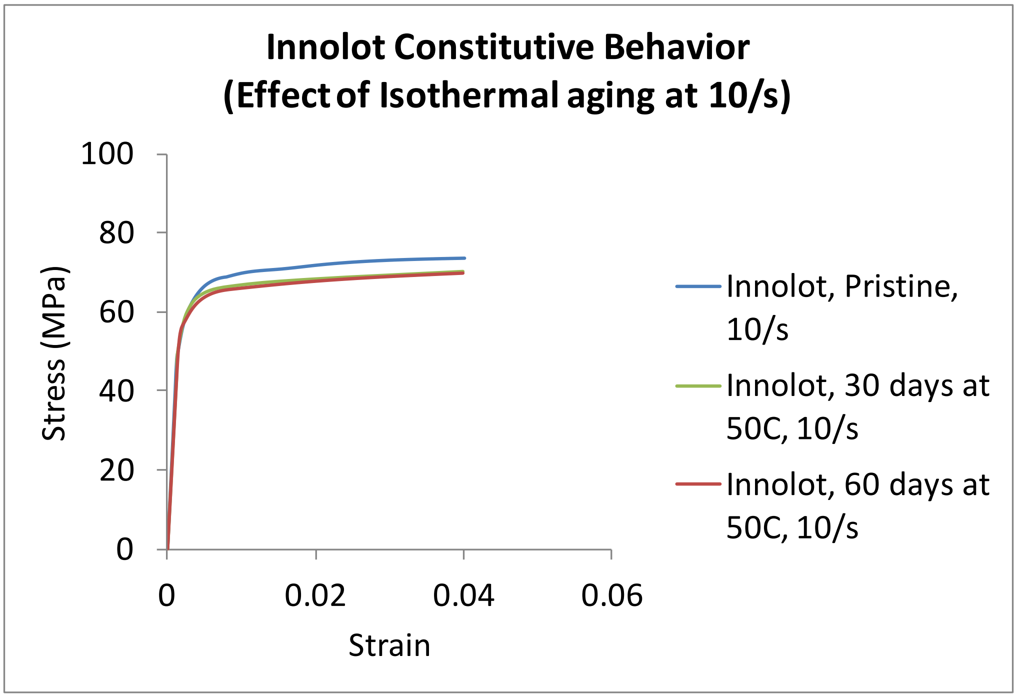

Figure 53: Influence of aging on stress strain curves of Innolot at 10/s

Table 17: Aging effects on material properties of Innolot at 10/s

Aging	**E (GPa)**	**UTS (MPa)**
Pristine	39.3	73.8
30 days at 50C	36.01	70.4
60 days at 50C	35.63	70.02

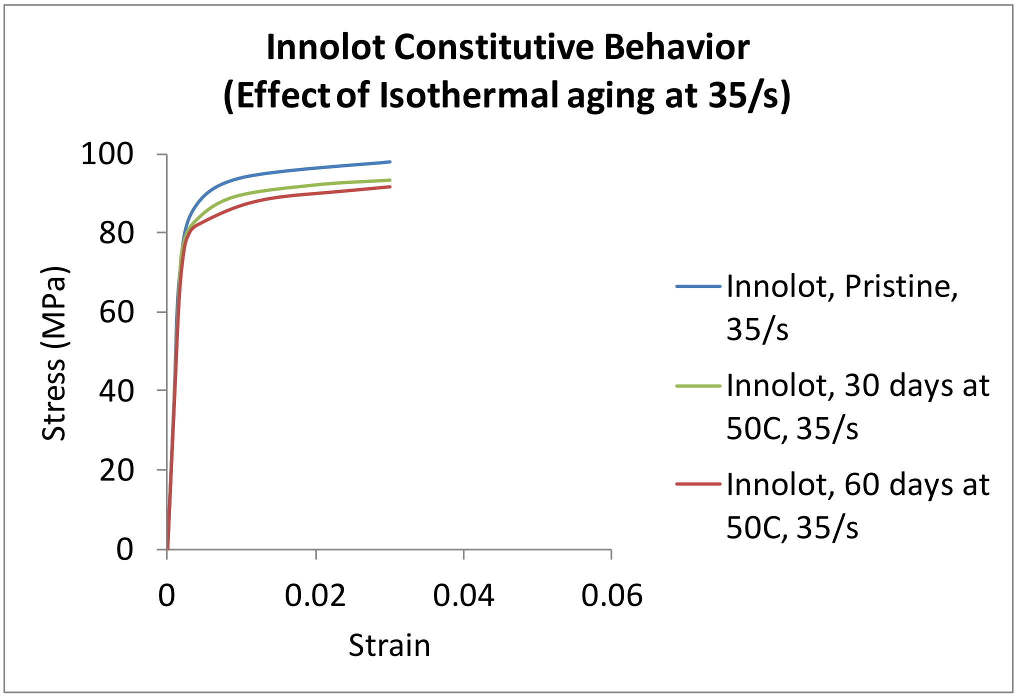

Figure 54: Influence of aging on stress strain curves of Innolot at 35/s

Table 18: Aging effects on material properties of Innolot at 35/s

Aging	**E (GPa)**	**UTS (MPa)**
Pristine	43.5	98
30 days at 50C	41.7	93.2
60 days at 50C	41	91.7

4.5.5. *Effect of strain rate on material properties of Innolot*

Figure 49 through Figure 52 show the response of Innolot for each of the test case. Each of these plots contain two stress-strain curves one of which is obtained at a constant strain rate of 10/s and the other at a constant strain rate of 35/s. It can be seen that at every precondition, the stress-strain curve at 10/s lies below the stress-strain curve at 35/s. Correspondingly, the elastic modulus and the UTS have lower values at the lower strain rate. Table 13 through Table 16 contain the numerical values of the effective elastic modulus and ultimate tensile strength. This response can be attributed to the fact that Innolot is a highly strain rate dependent material. The higher the strain rate, the more stiff the material behaves thus yielding a higher value of elastic modulus and UTS.

4.5.6. Comparison with SAC alloys

These authors have previously published data on SAC105 and SAC305 using the same test setup, strain rates and aging conditions [Lall 2012]. Figure 55 compares the constitutive behavior of the three alloys in all the test cases. It can be seen that while the elastic modulus of Innolot is comparable with SAC305, the UTS of Innolot is much higher than both SAC105 and SAC305. Table 19 and Table 20 compares the percent decrease in the material properties of the three alloys due to aging at the strain rate of 10/s. The elastic modulus of Innolot reduces by 9.34% where as that of SAC105 and SAC305 reduces by 37.5% and 43.28% respectively. Likewise, the UTS of Innolot reduces by 5.12% where as that of SAC105 and SAC305 reduces by 14.99% and 9.7% respectively.

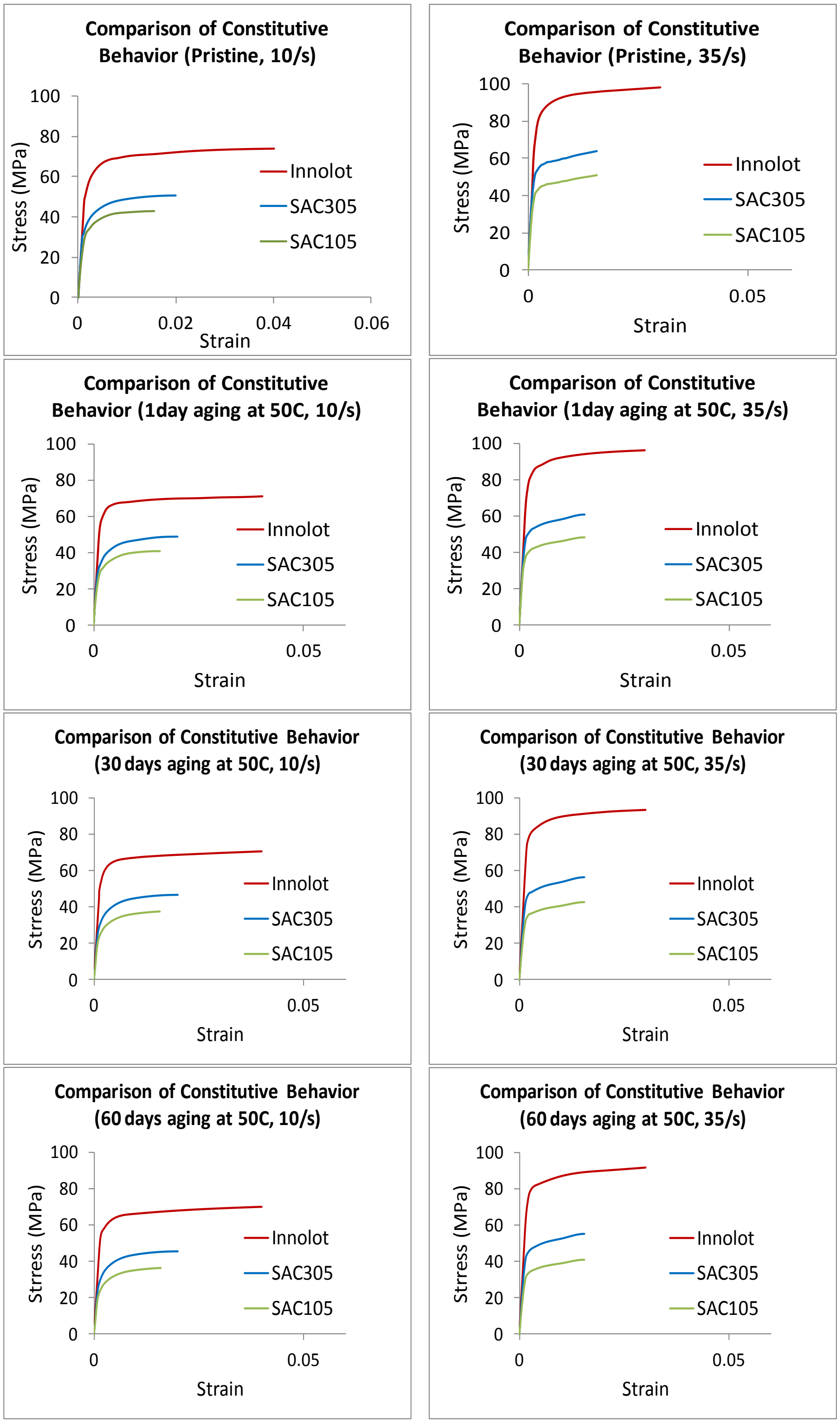

Figure 55: Visual comparison of constitutive behavior of Innolot with SAC105 [Lall et. al. 2012] and SAC305 [Lall et. al. 2012]

Table 19: Comparison of Elastic Modulus degradation in Innolot, SAC105 and SAC305 due to aging

Pre-condition	% Reduction in elastic modulus with Pristine as baseline					
	Innolot E(GPa)		SAC105 E(GPa) [Lall et. al. 2012]		SAC305 E(GPa) [Lall et. al. 2012]	
	10/s	35/s	10/s	35/s	10/s	35/s
Pristine	0	0	0	0	0	0
1day at 50C	2.29	3.22	6.15	3.88	11.44	13.28
30 days at 50C	8.37	4.14	35.4	31.94	40.3	39.41
60 days at 50C	9.34	5.75	37.5	36.42	43.28	41.08

Table 20: Comparison of UTS degradation in Innolot, SAC105 and SAC305 due to aging

Pre-condition	% Reduction in UTS with Pristine as baseline					
	Innolot UTS (MPa)		SAC105 UTS (MPa) [Lall et. al. 2012]		SAC305 UTS (MPa) [Lall et. al. 2012]	
	10/s	35/s	10/s	35/s	10/s	35/s
Pristine	0	0	0	0	0	0
1day at 50C	3.52	2.04	4.17	6.02	4.95	4.69
30 days at 50C	4.6	4.9	11.71	17.47	8.51	12.5
60 days at 50C	5.12	6.43	14.99	20.39	9.70	13.9

Innolot thus exhibits much higher resistance to aging that these SAC alloys. Compared with SAC105 and SAC305 alloys, Innolot material properties exhibit a higher strain rate dependence. On the other hand, the influence of aging at a given strain rate in Innolot, is much less pronounced. The microstructure of a pristine sample of Innolot is shown in

Figure 56. Although some evolution in the microstructure is observed after 30 days aging (Figure 57), between 30 days and 60 days (Figure 58) there is very little change in the microstructure. This is in line with the small changes in the elastic modulus and UTS values of 30 days aged samples and 60 days aged samples tabulated in Table 19 and Table 20.

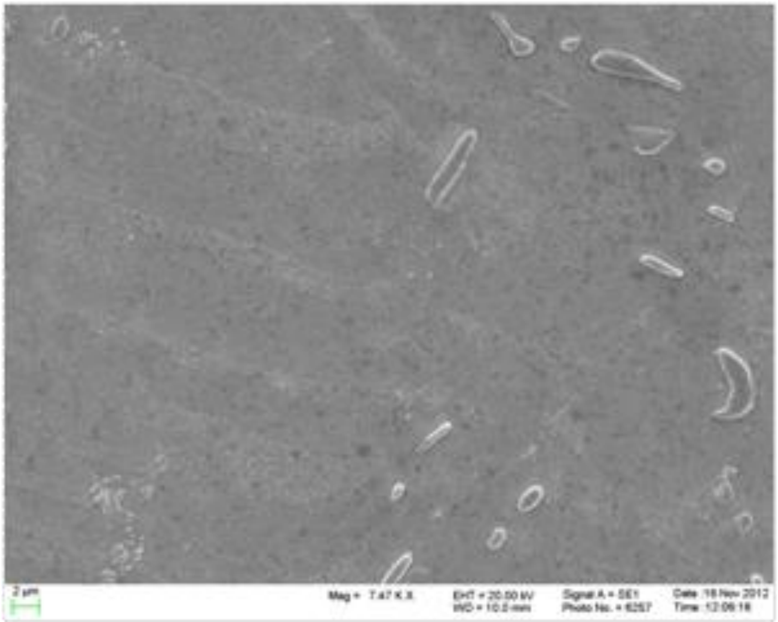

Figure 56: Innolot, Pristine

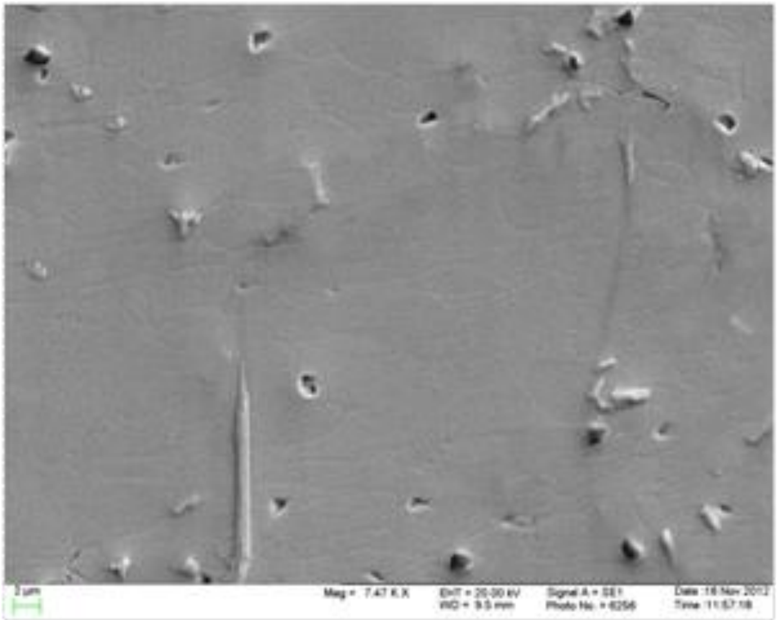

Figure 57: Innolot, 30 days at 50C

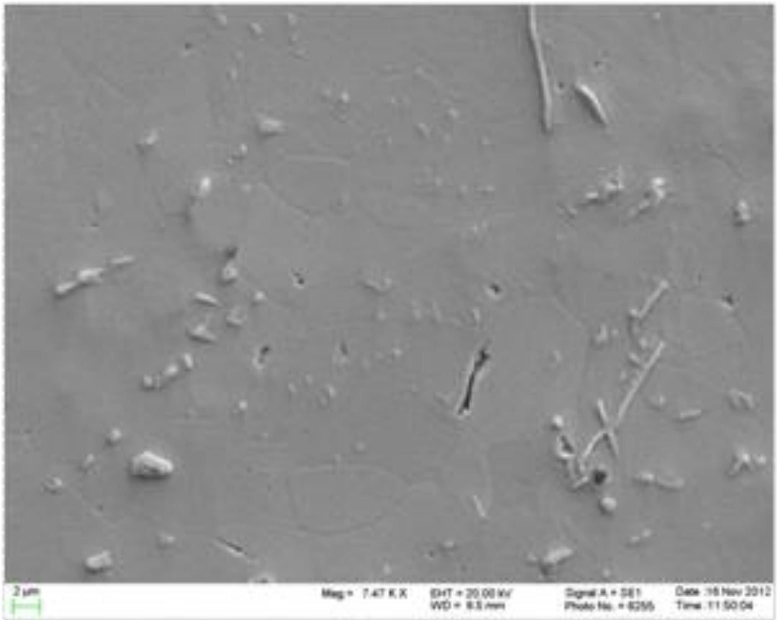

Figure 58: Innolot, 60 days at 50C

Table 19, Table 20compare the percent decrease in the material properties of the three alloys due to aging at the strain rate of 10/s. The elastic modulus of Innolot reduces by 9.34% where as that of SAC105 and SAC305 reduces by 37.5% and 43.28% respectively. Likewise, the UTS of Innolot reduces by 5.12% where as that of SAC105 and SAC305 reduces by 14.99% and 9.7% respectively. Innolot thus exhibits much higher resistance to aging that these SAC alloys.

4.5.7. Ramberg-Osgood Non-linear models for Innolot

Non-linear relationship between stress-strain curves of solder are often described using Ramberg-Osgood model. The model can represent strain hardening effects well, is simple to implement in Abaqus based FE codes and the parameters required for the model can be estimated easily if the constitutive behavior is available. In this model, the axial strain in a tensile sample strain at a stress level is considered to consist of elastic (e) and plastic (p) parts given by the equation below: [Ranberg et. al. 1943, Lall et. al. 2012]

$$\varepsilon = \left(\frac{\sigma}{E}\right)_e + \left[K\left(\frac{\sigma}{E}\right)^n\right]_p \tag{43}$$

where σ is the stress along the axial direction, E is the elastic modulus and K and n are the shape parameters. To estimate K and n, the following closed form approach can be used. Dimensionless variables α and φ are defined as [Lall et. al. 2012]:

$$\alpha = \frac{\varepsilon}{\sigma_1} E \tag{44}$$

$$\phi = \frac{\sigma}{\sigma_1} \tag{45}$$

where σ$_1$ is the secant yield strength. Multiplying both sides of equation (43) by (E/ σ$_1$) [Lall et. al. 2012]

$$\frac{E}{\sigma_1}\varepsilon = \frac{E}{\sigma_1}\left(\frac{\sigma}{E}\right) + \left[K\frac{E}{\sigma_1}\left(\frac{\sigma}{E}\right)^n\right] \tag{46}$$

Substituting Eq. (44) and Eq. (45) in Eq. (46) [Lall et. al. 2012]

$$\alpha = \phi + \left[K\phi\left(\frac{\sigma}{E}\right)^{n-1}\right] \tag{47}$$

Substitute σ$_1$=σ, [Lall et. al. 2012]

$$\alpha = \phi + \left[K\phi^n\left(\frac{\sigma}{E}\right)^{n-1}\right] \tag{48}$$

The abscissa of the secant yield strength for stress strain curve in Figure 59 is given by modifying Eq.(43) and substituting σ$_1$=σ, [Lall et. al. 2012]

$$\varepsilon_1 = \left(\frac{\sigma_1}{m_1 E}\right) = \frac{\sigma_1}{E} + K\left(\frac{\sigma_1}{E}\right)^n \tag{49}$$

where $m_1E=\sigma_1/\varepsilon_1$ as shown in Figure 59. Multiply Eq. (49) by E/σ_1

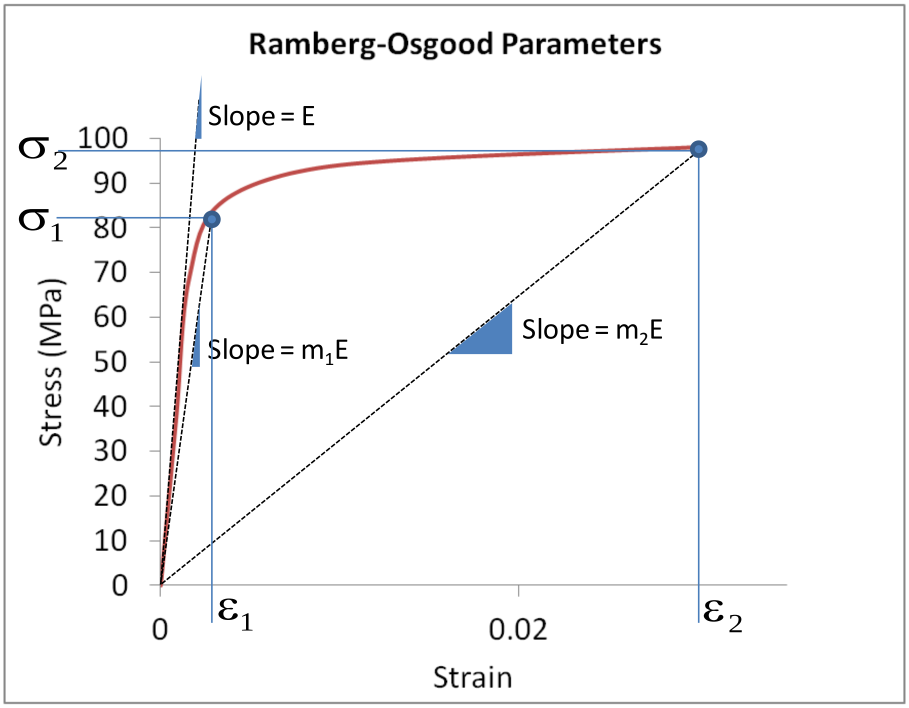

Figure 59: Determination of secant yield strength [Adapted from Lall et. al. 2012]

$$\frac{1}{m_1} = 1 + K\left(\frac{\sigma_1}{E}\right)^{n-1} \tag{50}$$

Rearranging Eq. (50), [Lall et. al. 2012]

$$K = \frac{1-m_1}{m_1}\left(\frac{\sigma_1}{E}\right)^{1-n} \tag{51}$$

$$\alpha = \phi + \left[K\phi^n \left(\frac{\sigma_1}{E} \right)^{n-1} \right] \tag{52}$$

$$\alpha = \phi + \left[\left(\frac{1-m_1}{m_1} \right) \left(\frac{\sigma_1}{E} \right)^{1-n} \phi^n \left(\frac{\sigma_1}{E} \right)^{n-1} \right] \tag{53}$$

$$\alpha = \phi + \left(\frac{1-m_1}{m_1} \right) \phi^n \tag{54}$$

Related stress-strain curves that may be described by equation (54) have the same value of n. Figure 60 shows a family of curves for m1=0.75 and different values of n. The stress deviation curve has been obtained by plotting stress against the difference between the measured strain and elastic strain according to Hooke's law. [Lall et. al. 2012]

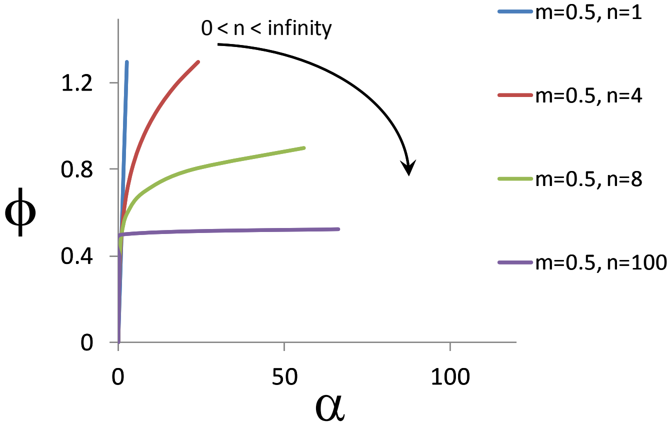

Figure 60: Family of curves for different values of n and m1=0.5 [Adapted from Lall et. al. 2012]

$$d = \varepsilon - \frac{\sigma}{E} = \left(\frac{\sigma}{E}\right) + \left[K\left(\frac{\sigma}{E}\right)^n\right] - \left(\frac{\sigma}{E}\right) = K\left(\frac{\sigma}{E}\right)^n \tag{55}$$

$$\log d = \log K + n\log\left(\frac{\sigma}{E}\right) \tag{56}$$

m$_1$ is chosen such that the secant yield strength 1 would approximately be the yield strength for 0.002 offset strain. Thus Eq. (55) can be written as: [Lall et. al. 2012]

$$0.002 = \varepsilon - \frac{\sigma}{E} = \left(\frac{\sigma_1}{m_1 E}\right) - \frac{\sigma}{E} \tag{57}$$

m$_1$ is solved for using this equation: [Lall et. al. 2012]

$$\frac{1}{\mathrm{m}_1} = \frac{0.002}{\sigma_1/\mathrm{E}} + 1 = \frac{0.002}{\sigma_{0.2}/\mathrm{E}} + 1 \tag{58}$$

The shape parameter is derived using the second secant yield strength σ_2 corresponding to second secant modulus m$_2$E [Lall et. al. 2012]

$$\varepsilon_2 = \left(\frac{\sigma_2}{m_2 E}\right) = \frac{\sigma_2}{E} + K\left(\frac{\sigma_2}{E}\right)^n \tag{59}$$

$$\frac{1}{m_2} = 1 + K\left(\frac{\sigma_2}{E}\right)^{n-1} \tag{60}$$

The equations for K and n gives [Lall et. al. 2012]:

$$K = \frac{1-m_2}{m_2}\left(\frac{\sigma_2}{E}\right)^{1-n} \tag{61}$$

$$n = 1 + \frac{\log_{10}\left(\frac{m_2}{m_1} \bullet \frac{1-m_1}{1-m_2}\right)}{\log_{10}\left(\frac{\sigma_1}{\sigma_2}\right)} \tag{62}$$

shape parameter is derived using the second secant yield strength σ_2 corresponding to second secant modulus m_2E

Figure 61 shows the Ramberg-Osgood model fit through the experimental data on Innolot for the Pristine case. The model fits well through the data for all the cases considered in this study. The values of the parameters n and K obtained for each of the cases is tabulated below. By using these parameters, the response of solder interconnects can be modeled very accurately in component or PCB level drop-shock or vibration simulations using commercial FE codes.

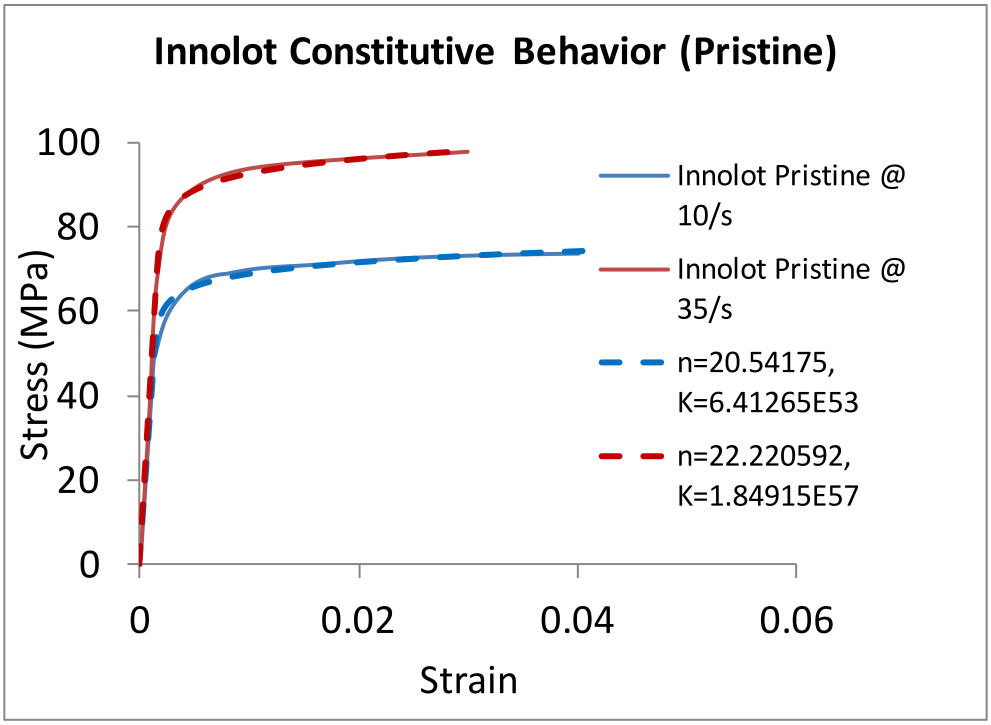

Figure 61: Ramberg-Osgood model parameters and curve fit

Table 21: Ramberg-Osgood Parameters for Innolot

Aging	**Strain rate (/s)**	**E (GPa)**	**n**	**K**
Pristine	10	39.3	20.54175	6.41265E53
1day @ 50C	10	38.4	26.17152	1.21237E+70
30 days @ 50C	10	36.01	33.38179	1.09736E+89
60 days @50C	10	35.63	24.80184	5.11964E+65
Pristine	35	43.5	22.22059	1.84915E57
1day @ 50C	35	42.1	24.47599	1.27544E+63
30 days @ 50C	35	41.7	22.65212	2.8671E+58
60 days @50C	35	41	23.05484	3.56932E+59

Another method for obtaining K, n and E is by using a regression fit through the experimental data. As a sample case, the regression fit for pristine data at strain rate of 35/s has been obtained. Non-linear least-square based regression technique called Levenberg-Marquardt algorithm has been used for regression. Equation (43) is solved for K, n and E such that the error between the actual and regressed value of the response variable (i.e. strain) is minimized. The R^2 of regression fit is 0.9575 and the sum of squared errors is 0.0001404. The values of the three parameters obtained after regression are tabulated in Table 22. It can be observed that the closed form 2-point solution method given by Equation **(61)** and Equation **(62)** predicts the Ramberg-Osgood model parameters n, K and E almost as accurately as a regression fit through the entire stress-strain data. This method also has the advantage of being computationally efficient.

Table 22: Comparison of Ramberg-Osgood parameters obtained using regression fit and closed form 2-point solution methods (Pristine, 35/s)

Parameter	**Regression** **R^2=0.9575** **rmse = 0.01185**	**2-point solution** **R^2=0.8814** **rmse = 13.3516**
E (Pa)	43e+9	43.5e+9
n	22.31	22.22059
K	1.8e57	1.84915E+57

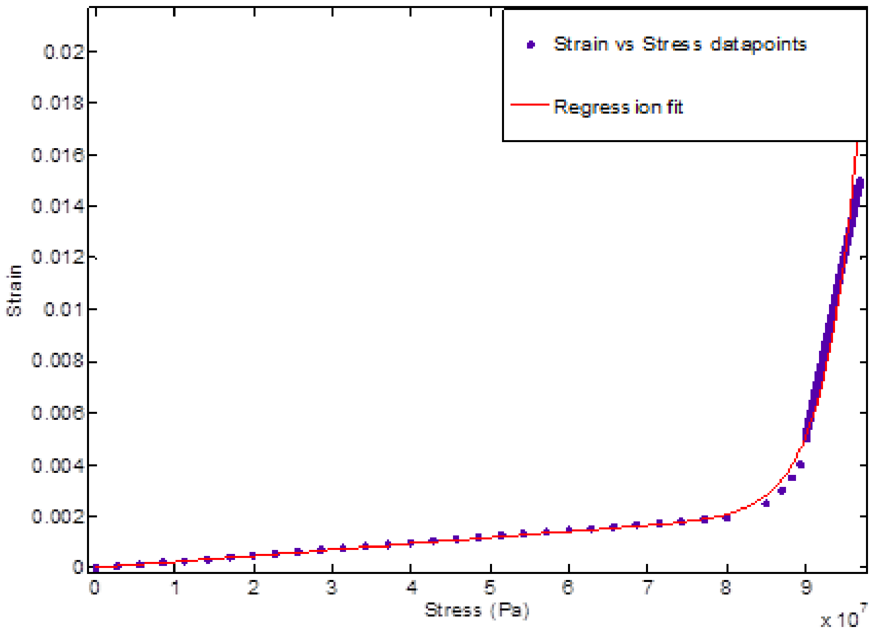

Figure 62: Regression fit through strain-stress data of pristine Innolot at 35/s

4.5.8. Digital Image Correlation

Digital image correlation (DIC) is an optical method to measure full-field deformation and the derivatives of deformation on the surface of a loaded structure. For 2D DIC analysis of the specimens, a thin layer of white pain is coated on the surface of the specimen. Random black speckle pattern is created on the white background. As the specimen deforms due to loading, the geometric positions of the speckles change with respect to the initial position when the specimen is un-deformed. High speed cameras capture the deformation of the specimen to failure at about 80000 frames per second. The motion of every speckle in all the frames is tracked using sum of squared difference correlation. This gives the full field displacement contour. Gradients of the displacement contour are calculated to obtain the full field strains. In this study, Digital image correlation has been used to correlate the FE model of the tensile specimen with Ramberg-Osgood material model. A representative case of this correlation is presented here. DIC analysis has been conducted for a Pristine specimen tested at 35/s. From the red curve in Figure 61, plastic deformation corresponds to strains exceeding 1.97e-3. Since the strain rate is constant, this should occur after (1.97e-3/35)s i.e after 0.00005629s, the strain should be 1.97e-3. Likewise UTS occurs at strain = 0.003 which would occur in 0.008571s. This is demonstrated in Figure 63.

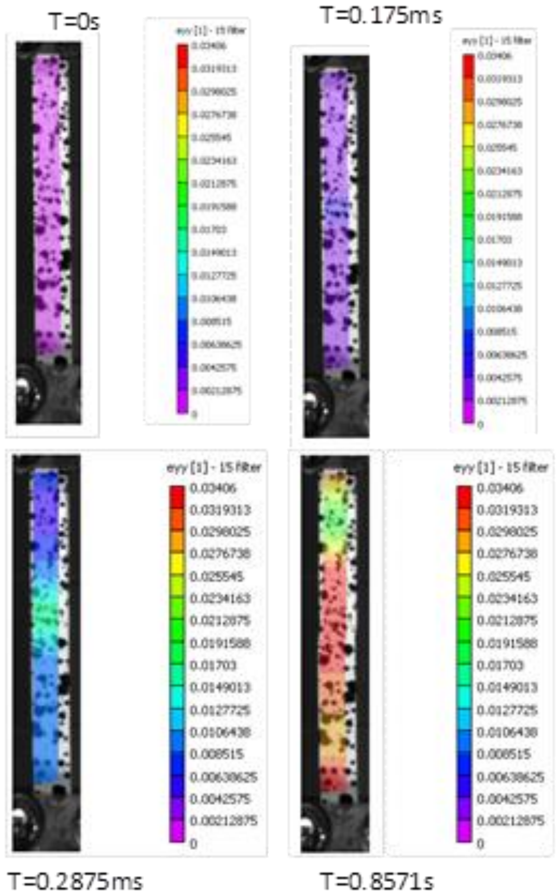

Figure 63: DIC analysis of Innolot, Pristine case at 35/s

4.5.9. FE model for tensile specimen

A FE model of the tensile specimen is shown in Figure 63. This model uses 3D solid 8-noded continuum elements (C3D8I). Displacement BC corresponding to a strain rate of

35/s is applied in the negative y direction at the bottom end of the specimen. The top end is fully constrained. The Ramberg-Osgood material model derived for this case is implemented for simulation in Abaqus. The stress-strain response of this model correlates well with the experimental behavior. This is demonstrated in

Figure **64** and

Figure **65**. Strain time histories of the model are close to the expected strain time histories given the constant strain rate of 35/s used for the tensile test. The full field strain contours also correlate with DIC to a good extent.

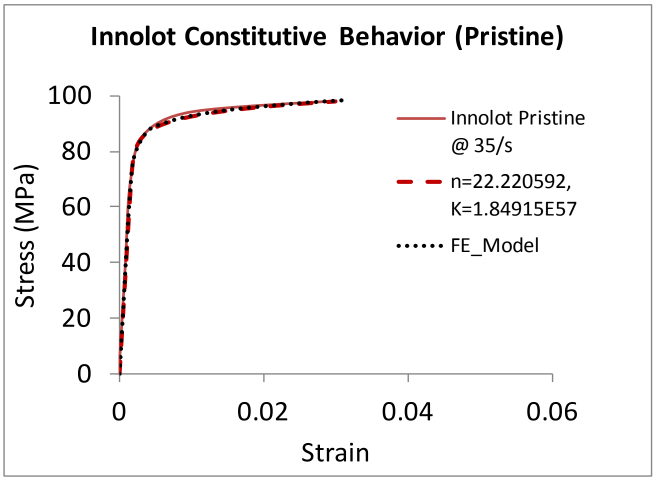

Figure 64: Stress-strain response of a point at the center on FE model of tensile specimen

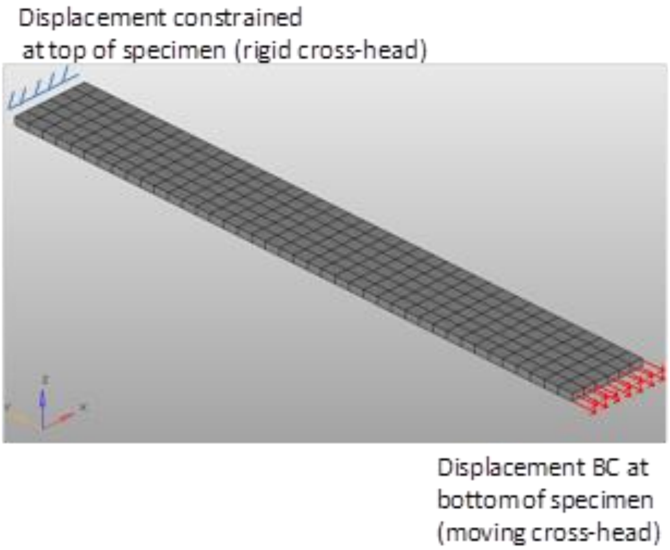

Displacement constrained at top of specimen (rigid cross-head)

Displacement BC at bottom of specimen (moving cross-head)

Figure 65: FE model of tensile specimen

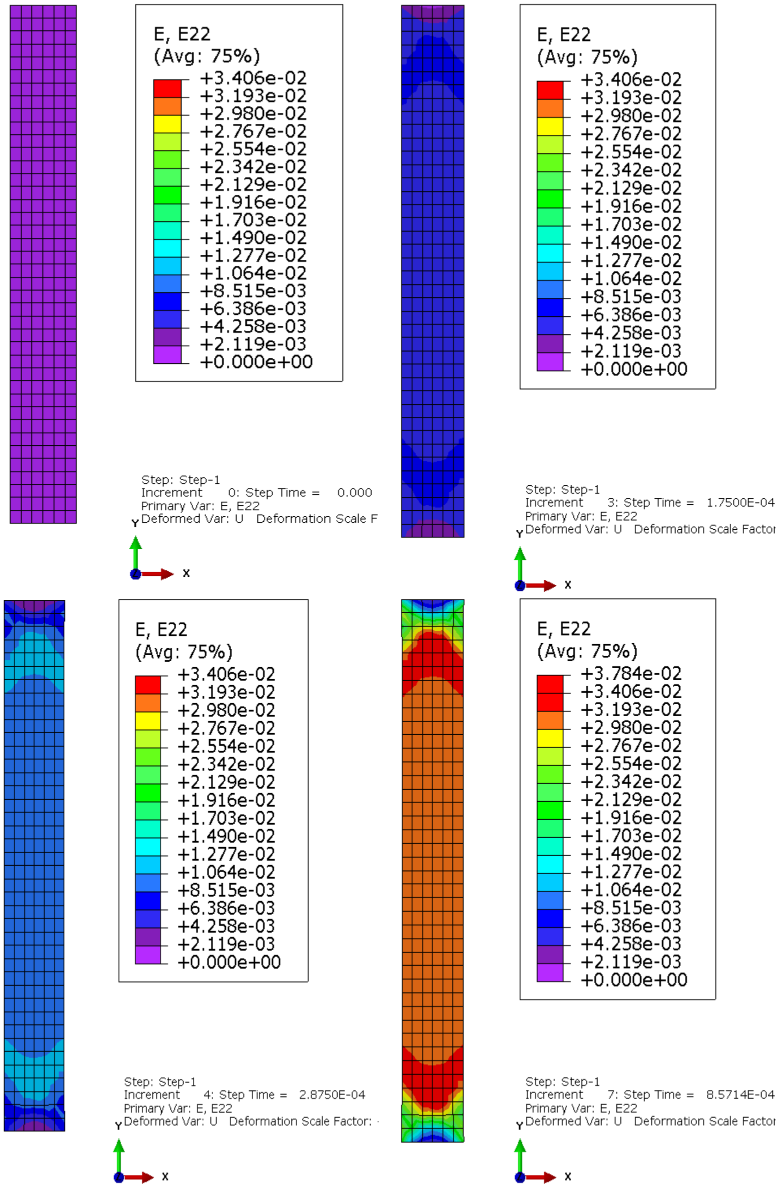

Figure 66: Strain contours of tensile specimen at time steps of 0s, 1.75e-4s, 2.875e-4s and 8.5714e-4s

4.6 Summary and Conclusions

Stress-strain curves for Innolot were experimentally obtained for strain rates of 10/s and 35/s. Effect of isothermal aging on the material properties of Innolot was studied by aging specimens at 50C for three durations of 1day, 30days and 60days. The constitutive behavior of Innolot and material property degradation due to aging was compared with SAC105 and SAC305 data collected previously by these authors. While Innolot is more strain rate dependent than the two SAC alloys, it is much better at resisting material property degradation due to aging. There is very little degradation in the material properties and the microstructure of Innolot as it ages from 30 days to 60 days at 50C. Ramberg-Osgood model is used to fit the experimental data. A two point closed form solution method to predict the Ramberg-Osgood parameters, is compared with regression fit. The three parameters required for implementing this model have been derived for all the test cases. FE simulation of the tensile test correlates well with the tensile test in terms of the specimen stress-strain response. The full field strain contours occurring at various points in time match well with the experimentally obtained contours using Digital Image Correlation.

CHAPTER 6

SUMMARY, CONCLUSIONS AND FUTURE SCOPE

The initial part of this study is to develop a methodology for creating a model for high cycle fatigue life reliability of Pb-free solders subjected to the combined environment of high temperature and vibration has been proposed. A combination of experimental and numeric techniques have been employed for creating this model. The simultaneous harsh environment of high temperature and vibration is observed to have wide application for automotive electronics. To simulate this environment in the lab, the existing shaker system was updated by coupling it with an isothermal chamber, so that the PCB under test would simultaneously experience elevated temperature and vibration levels. Following is a brief discussion of the underlying assumptions.

This model fits the failure data on the test vehicle under consideration to a good extent. The model assumes that the high cycle fatigue failures in SAC305 occur due to repeated loading less than the elastic limit. The Basquin power law relating the stress amplitude level to fatigue life in terms of stress reversal cycles to failure is assumed to hold true. It is assumed that the S-N relations hold true even at elevated temperatures lest with evolved fatigue strength coefficients and fatigue exponents. Further, the evolution of these two parameters with temperature is considered to be governed by the adaptated form of Arrhenius equation used to predict the influence of steady state temperature on electronic device reliability. In this study, a test vehicle representative of an engine control unit containing SAC305 components has been tested to failure subjecting it to its first natural frequency. The first natural frequency is chosen to accelerate the lab tests. However, it was observed that there is a significant shift in the first natural frequency with increase in the temperature. Therefore the PCB is subjected to slightly different frequencies depending on the selected test temperature. It is assumed that within this range of frequencies (~15Hz) the solder high cycle fatigue life remains constant. First natural frequency of the test vehicle has been determined at three temperatures: 25C, 75C and 125C. It is observed to reduce linearly with increase in temperature. The test vehicles are tested to failure by subjecting to harmonic vibration, dwelling at the natural frequency for each test temperature. Cycles to failure are derived from the experiments for BGAs and TSOPs that fail at the solder. A reduction in mean cycles to failure is observed with increase in temperature for each component. Tensile tests, DMA and DSC analyses are conducted to determine the actual material properties of the PCB experimentally. These have been used as inputs to the PCB in the global model. Smeared properties for components are calculated for components in the global model. The global FE model is then correlated with the test vehicle using natural frequencies, mode shapes and out of plane displacement fields. Global model drives the detailed explicit sub-model of the components to output solder Von Mises stresses with material property degradation at temperature. Volume averaged solder stresses at high stress location of every component is plotted against its experimentally obtained cycles to failure. Curve-fitting based on Basquin power law relation between stress amplitude and stress reversal cycles yields the S-N curve at that temperature. S-N curves at 25C, 75C and 125C are thus obtained for SAC305. The temperature dependence of the fatigue strength coefficient and fatigue exponent have been implemented in the SAC305 S-N curve relation. It can be observed that for the same stress level, this model predicts lesser cycles to failure at higher test temperatures.

In the later part of this research work, a newly developed solder alloy called Innolot, targeting the automotive industry is characterized to obtain its uniaxial tensile stress-strain characteristic stress-strain curves at high strain rates and elevated temperature aging. Stress strain curves for Innolot were experimentally obtained for strain rates of 10/s and 35/s. Effect of isothermal aging on the material properties of Innolot was studied by aging specimens at 50C for three durations of 1day, 30days and 60days. The constitutive behavior of Innolot and material property degradation due to aging was compared with SAC105 and SAC305 data collected previously by these authors. While Innolot is more strain rate dependent than the two SAC alloys, it is much better at resisting material property degradation due to aging. There is very little degradation in the material properties and the microstructure of Innolot as it ages from 30 days to 60 days at 50C. Ramberg-Osgood model is used to fit the experimental data. A two point closed form solution method to predict the Ramberg-Osgood parameters, is compared with regression fit. The three parameters required for implementing this model have been derived for all the test cases. FE simulation of the tensile test correlates well with the tensile test in terms of the specimen stress-strain response. The full field strain contours occurring at various points in time match well with the experimentally obtained contours using Digital Image Correlation.

In the future, the high cycle fatigue model for SAC305 needs to be tested and improvised if needed for a larger dataset preferably conforming to Weibull failure distribution. Similar predictive models can be created for other solder alloys. In the high strain rate material characterization, Innolot needs to be tested under additional strain rates in the range of 1-100 per second. The effect of additional aging temperatures and duration on the material properties of Innolot can also be studied.

BIBLIOGRAPHY

Al-Yafawi, A., Patil, S., Yu, D., Park, S., Pitarresi, J., and Goo, N., Random Vibration Test for Electronic Assemblies Fatigue Life Estimation, Thermal and Thermomechanical Phenomenon in Electronic Systems ITherm, pp. 1-7, June 2010.

Amodio, D., Broggiato, G., Campana, F., Newaz, G., Digital Speckle Correlation for Strain Measurement by Image Analysis, Experimental Mechanics, Vol. 43, No. 4, pp. 396- 402, 2003.

Barker, D., Vodzak, J., Dasgupta A., Pecht, M., Combined vibrational and thermal solder joint fatigue: A generalized strain versus life approach, Transactions ASME Journal of Electron. Packaging, Vol. 112, pp. 129–134, June 1990.

Barker, D., Vodzak, J., Dasgupta A., Pecht, M., PWB solder joint life calculations under thermal and vibrational loading, Journal of Institute of Environmental Science, Volume 35, No. 1, pp. 17–25, Feb. 1992.

Basaran, C., Chandaroy, R., Thermomechanical analysis of solder joints under thermal and vibrational loading, Transactions of ASME, Volume 124, pp. 60–66, Mar. 2002.

Bhate, D., Chan, D., Subbarayan, G., Chiu, T., C., Gupta, V., Edwards, D., R., Constitutive Behavior of Sn3.8Ag0.7Cu and Sn1.0Ag0.5Cu Alloys at Creep and Low Strain Rate Regimes, IEEE Transactions on Components and Packaging Technologies, Vol. 31, No. 3, Sep 2008.

Cabezas, E., E., Celentano, D, J., Finite Elements in Analysis and Design 40, pp.555–575, 2004.

Chan, D., Nie, X., Bhate, C., Subbarayan, G., Dutta, I., High Strain Rate Behavior of Sn3.8Ag0.7Cu Solder Alloys and Its Influence on the Fracture Location Within Solder Joints, 3rd International Conference on Energy Sustainability, ASME InterPACK, San Francisco, California, USA, pp 989-995, July 19–23, 2009.

Chen, X., Song, J., Kim, K., S., Fatigue life of 63Sn–37Pb solder related to load drop under uniaxial and torsional loading, International Journal of Fatigue 28, pp.767–776, 2006.

Chuang, C. M., Liu, T. S., Chen, L. H., Effect of Aluminum Addition on Tensile Properties of Naturally Aged Sn-9Zn Eutectic Solder, Journal of Materials Science, Vol. 37(1), pp. 191-195, 2002.

Clech J., Solder Reliability Solutions: A PC-Based Design-for-Reliability Tool, Proceedings of Surface Mount International, pp. 136-151, San Jose, CA, Sept. 8-12, 1996

Coyle, R. J., Solan, P. P., Serafino, A. J., and Gahr, S. A., The Influence of Room Temperature Aging on Ball Shear Strength and Microstructure of Area Array Solder Balls, Proceedings of the 50th Electronic Components and Technology Conference, pp. 160-169, 2000.

Darveaux R., Reichman C., Islam N., Interface Failure in Lead Free Solder Joints, Proceedings of 56th ECTC, pp. 152-156, 2006.

Darveaux, R., Shear Deformation of Lead Free Solder Joints, Proceedings of the 55th Electronic Components and Technology Conference, pp. 882-893, 2005.

Dehbi, A., Ousten, Y., Danto, Y., Wondrak, W., Microelectronics Reliability 45 (2005) 1658-1661.

Ding, Y., Wang, C., Tian, Y., and Li, M., Influence of Aging on Deformation Behavior of 96.5Sn3.5Ag Lead Free Solder Alloy During In Situ Tensile Tests, Journal of Alloys and Compounds, Vo. 428, pp. 274-285, 2007.

Dumoulin, S., Tabourot, L., Chappuis, C., VacherP., Arrieux, R., Journal of Materials Processing Technology 133, pp 79–83, 2003.

Gershon, A., L., Bruck, H., A., Xu, S., Sutton, M., A., Tiwari, V., Multiscale mechanical and structural characterizations of Palmetto wood for bio-inspired hierarchically structured polymer composites, Materials Science and Engineering 30, pp. 235–244, 2010.

Grytten, F., Daiyan, H., Polanco-Loria M., Dumoulin, S., Use of digital image correlation to measure large-strain tensile properties of ductile thermoplastics, Polymer Testing 28, pp 653–660, 2009.

Hargather, M., J., Settles, G., S., Laboratory-scale techniques for the measurement of a material response to an explosive blast, International Journal of Impact Engineering 36, pp 940–947, 2009.

Henderson, G., Piersol, A., Fatigue Damage Related Descriptor for Random Vibration Test Environments, Sound and Vibration, Volume 29, No. 10, pp. 20–24, Oct. 1995.

Hu, J., Life Prediction and Damage Acceleration Based on the Power Spectral Density of Random Vibration, Journal of IES, Volume 38, No. 1, pp. 34–40. Jan/Feb. 1995.

Hsuan, T. C., and Lin, K. L., Effects of Aging Treatment of Mechanical Properties and Microstructure of Sn-8.5Zn- 0.5Ag-0.01Al-0.1Ga Solder, Materials Science and Engineering, A 456, pp. 202-209, 2007.

Inal, K., Wu, P., D., Neale, K., W., International Journal of Solids and Structures, 39, pp.982–1002, 2002.

Johnson, R., Evans, J., Jacobsen, P., Thompson, J., Christopher, M., The Changing Automotive Environment: High-Temperature Electronics, IEEE Transactions on Electronics Packaging Manufacturing, Vol.27, NO. 3, July 2004.

Joun, M., Choi, I., Eom, J., Lee, M., Finite element analysis of tensile testing with emphasis on necking, Computational Materials Science 41, pp 63–69, 2007.

Kehoe, L., Lynch, P., Guénebaut, V., Measurement of Deformation and Strain in First Level C4 Interconnect and Stacked Die using Optical Digital Image Correlation, Proceedings of the 56th ECTC, pp. 1874-1881, May 2006.

Kim, K., S., Huh, S., H., Suganuma, K., Effects of cooling speed on microstructure and tensile properties of Sn–Ag– Cu alloys, Materials Science and Engineering A333, pp 106–114, 2002.

Kirkpatrick, S. W., MacNeill, R., & Bocchieri, R. T., Development of an LS-DYNA occupant model for use in crash analyses of roadside safety features, TRB 2003 Annual Meeting, January 2003.

Knecht, S., Fox, L., R., Constitutive Relation and Creep- Fatigue Life Model for Eutectic Tin-Lead Solder, IEEE Transctions on Components, Hybrids and Manufacturing Technology, Vol 13, No. 2, June 1990.

Koc, P., Stok, B., Computational Materials Science 31, pp.155–168, 2004.

Komori, K., Journal of Materials Processing Technology 125–126, pp.608–612, 2002

Lall, P., Panchagade, D., Liu, Y., Johnson, W., Suhling, J., Models for Reliability Prediction of Fine-Pitch BGAs and CSPs in Shock and Drop-Impact, Proceedings of the 54th ECTC, pp. 1296-1303, 2004.

Lall, P., Panchagade, D., Choudhary, P., Suhling, J., Gupte, S., Failure Envelope Approach to Modeling Shock and Vibration Survivability of Electronic and MEMS Packaging, Proceedings of the 55th ECTC, pp. 480-490, 2005.

Lall, P., Gupte, S., Choudhary, P., Suhling, J. Solder-Joint Reliability in Electronics Under Shock and Vibration using Explicit Finite Element Sub-modeling, IEEE

Transactions on Electronic Packaging Manufacturing, Volume 30, no. 1, pp. 74-83, January 2007a.

Lall, P., Choudhary, P., Gupte, S., Suhling, J., Hofmeister, J., Statistical Pattern Recognition and Built-In Reliability Test for Feature Extraction and Health Monitoring of Electronics under Shock Loads, 57th Electronics Components and Technology Conference, Reno, Nevada, pp. 1161-1178, May 30-June 1, 2007b.

Lall, P., Panchagade, D., Iyengar, D., Shantaram, S., Suhling, J., Schrier, H., High Speed Digital Image Correlation for Transient-Shock Reliability of Electronics, Proceedings of the 57th ECTC, Reno, Nevada, pp. 924-939, May 29 – June 1, 2007c.

Lall, P. Panchagade, D., Liu, Y., Johnson, W., Suhling, J., Smeared Property Models for Shock-Impact Reliability of Area-Array Packages, ASME Journal of Electronic Packaging, Volume 129, pp. 373-381, December 2007d.

Lall, P., Hande, M., Bhat, C., Islam, N., Suhling, J., Lee, J., Feature Extraction and Damage-Precursors for Prognostication of Lead-Free Electronics, Microelectronics Reliability, Volume 47, pp. 1907–1920, December 2007e.

Lall, P., Choudhary, P., Gupte, S., Suhling, J., Health Monitoring for Damage Initiation and Progression during Mechanical Shock in Electronic Assemblies, IEEE Transactions on Components and Packaging Technologies, Vol. 31, No. 1, pp. 173-183, March 2008a.

Lall, P., Panchagade, D., Choudhary, P., Gupte, S., Suhling, J., Failure-Envelope Approach to Modeling Shock and Vibration Survivability of Electronic and MEMS Packaging, IEEE Transactions on Components and Packaging Technologies, Vol. 31, No. 1, pp. 104-113, March 2008b.

Lall, P., Iyengar, D., Shantaram, S., S., Gupta, P., Panchagade, D., Suhling, J., KEYNOTE PRESENTATION: Feature Extraction and Health Monitoring using Image Correlation for Survivability of Leadfree Packaging under Shock and Vibration, Proceedings of the 9th International Conference on Thermal, Mechanical, and Multi-Physics Simulation and Experiments in Micro-Electronics and Micro-Systems (EuroSIME), Freiburg, Germany, pp. 594-608, April 16-18, 2008c.

Lall, P., Iyengar, D., Shantaram, S., Pandher, R., Panchagade, D., Suhling, J., Design Envelopes and Optical Feature Extraction Techniques for Survivability of SnAg Leadfree Packaging Architectures under Shock and Vibration, Proceedings of the 58th Electronic Components and Technology Conference (ECTC), Orlando, Florida, pp. 036- 1047, May 27-30, 2008d.

Lall, P., Shantaram, S., Angral, A., Kulkarni, M., Explicit Submodeling and Digital Image Correlation Based Life- Prediction of Leadfree Electronics under Shock-Impact, 59th ECTC, San Diego, CA, pp. 542-555, May 25-29, 2009.

Lall P., Shantaram S., Panchagade D., Peridynamic-Models Using Finite Elements for Shock and Vibration Reliability of Lead-free Electronics, Proceedings of ITHERM 2010, Las Vegas, NV, June 2-5, 2010.

Lall, P., Shantaram, S., Kulkarni, K., Limaye, G., Suhling, J., Constitutive Behavior of SAC LeadFree Alloys at High Strain Rates, Proceedings of the ASME 2011 Pacific Rim Technical Conference & Exposition on Packaging and Integration of Electronic and Photonic Systems InterPACK201, July 6-8, 2011.

Lall, P., Limaye, G., Suhling, J., Murtuza, M., Palmer, B., Cooper, W., Reliability of lead-free SAC electronics under simultaneous exposure to high temperature and vibration, , 13th IEEE Intersociety Conference on Thermal and Thermomechanical Phenomena in Electronic Systems ITherm, pp. 753-761, May 2012.

Lall, P., Shantaram, S., Suhling, J., Locker, D., Effect of High Strain Rate on Mechanical Properties of SAC105 and SAC305 Leadfree Alloys, Electronic Components and Technology Conference, pp. 1312-1326, 2012

Lau, J., Solder Joint Reliability, Theory and Applications, Van Nostrand Reinhold, New York. 1991.

Lee, S. W., Tsui, Y. K., Huang, X., and Yan, C. C., Effects of Room Temperature Storage Time on the Shear Strength of PBGA Solder Balls, Proceedings of the 2002 ASME International Mechanical Engineering Congress and Exposition, Paper IMECE2002-39514, pp. 1-4, 2002.

Lee, S., Kim, J., A Mechanistic Model for Fatigue Life Prediction of Solder Joints for Electronic Packages, Int. J. Fatigue, Vol-19, No.1,pp.85-91, 1997.

Li, R., Failure Analysis and Fatigue Prediction of Microprocessors Under Automotive Vibration Environments, Proceedings, International Systems Packaging Symposium, San Diego, CA. 1999.

Li, R., A Methodology for Fatigue Prediction of Electronic Components Under Random Vibration Load, Journal of Electronic Packaging, Volume 123, pp. 394–400, Dec. 2001.

Meier, K., Roellig', M., Wiese, S., Wolter, K.-J., Characterization of the Mechanical Behavior of SAC solder at High Strain Rates, 11th. Int. Conf. on Thermal, Mechanical and Multiphysics Simulation and Experiments in Micro-Electronics and Micro-Systems, pp 1-6, EuroSimE 2010.

Meyer, M., Dynamic behavior of Materials, John Wiley and sons, Inc, 1994.

Miller, T., Schreier, H., Reu, P, High-speed DIC Data Analysis from a Shaking Camera System, Proceedings of the SEM Conference, Springfield, Massachusetts, June 4-6, 2007.

Miric, A., Z., New Developments in High-Temperature, High-Performance Lead-Free Solder Alloys, SMTA International Conference Proceedings, 2010.

Mirone, G., International Journal of Solids and Structures 41, p.3545–3564, 2004.

Muller, W., H., Worrack, H., Sterthaus, J., Villain, J.,Wilden, J., Juritza, A., How to extract continuum materials properties for (lead-free) solders from tensile tests and nanoindentation experiments, Microsyst Technol, 15:45–55, 2009.

Mysore, K., Subbarayan, G., Gupta, V., Zhang,R., Constitutive and Aging Behavior of Sn3.0Ag0.5Cu Solder Alloy, IEEE Transactions on Electronics Packaging Manufacturing, Vol. 32, No. 4, Oct, 2009.

Nguyen, T., T.,Park, S., Characterization of elasto-plastic behavior of actual SAC solder joints for drop test modeling, Microelectronics Reliability 51, pp.1385–1392, 2011.

Nilsson, K., European Journal of Mechanics A/Solids 20, pp.713–729, 2001.

Niordson, C., F., Redanz, P., Journal of the Mechanics and Physics of Solids 52, pp.2431–2454, 2004.

Ohguchi, K., Sasaki, K., Ishibashi, M., A Quantitative Evaluation of Time-Independent and Time-Dependent Deformations of Lead-Free and Lead-Containing Solder Alloys, Journal of Electronic Materials, Vol. 35, No. 1, 2006.

Pang, J. H. L., Xiong, B. S., and Low, T. H., Low Cycle Fatigue Models for Lead-Free Solders, Thin Solid Films Vol. 462- 463, pp. 408-412, 2004.

Pang, J., H., L., Xiong., B., S., Che, F., X., Modeling Stress Strain Curves for Leadfree 95Sn3.8Ag0.7Cu Solder, 5th Int. Conf. on Thermal and Mechanical Simulation and Experiments in Micro-electronics and Micro-system, EurosimE, 2004.

Papagiannopoulos, G., Hatzigeorgiou, G., On the use of the half-power bandwidth method to estimate damping in building structures, Soil Dynamics and Earthquake Engineering, Vol. 31, pp. 1075-1079, 2011.

Park, S., Shah, C., Kwak, J., Jang, C., Pitarresi, J., Transient Dynamic Simulation and Full-Field Test Validation for A Slim-PCB of Mobile Phone under Drop Impact, Proceedings of the 57th ECTC, Reno, Nevada, pp. 914-923, May 29 –June 1, 2007a.

Park, S., Reichman, A., Kwak, J., Chung, S., Whole Field Analysis of Polymer Film, Proceedings of the SEM Conference, Springfield, Massachusetts, June 4-6, 2007b.

Park, S., Al-Yafawi, A., Yu, D., Kwak, J., Lee, J., Goo, N., Influence of Fastening Methods on the Dynamic Response and Reliability Assessment of PCBS in Cellular Phones Under Free Drop, Proceedings of the ITherm, Intersociety Conference on

Thermal and Thermo-mechanical Phenomena, Orlando, Florida, pp.876-882, May 28-31, 2008

Park, T., Lee, S., Cyclic Stress- Strain Measurments Tests of Sn3.5Ag0.7Cu Solder Joint, Symposium on Electronic Material and Packaging, pp.317-323, 2002.

Pei, M., Qu, J., Constitutive Modeling of Lead-Free Solders, IEEE, 2005.

Peng, X., Balendra, R., Journal of Materials Processing Technology 145, pp.180–188, 2004.

Pierron, F., Sutton, M., A., Tiwari, V., Ultra High Speed DIC and Virtual Fields Method Analysis of a Three Point Bending Impact Test on an Aluminium Bar, Experimental Mechanics , 51, pp. 537–563, 2011.

Pitarresi, J.M., Modeling of Printed Circuit Cards Subject to Vibration, IEEE Proceedings of the Circuits and Systems Conference, New Orleans, LA, pp. 2104-2107, May 1990.

Pitarresi, J.M., et al, The Smeared Properties Approach to FE Vibration Modeling of Printed Circuit Cards, ASME Journal of Electronics Packaging, Volume 113, pp. 250-257, September 1991.

Pitarresi, J.M., Akanda, A., Random Vibration Response of a Surface Mounted Lead/Solder Joint, Proceedings of ASME International Electronics Packaging Conference, Volume 1, Binghamton, NY, pp. 207-217, Sept. 1993.

Plumbridge,W., J., Gagg, C., R., Effects of strain rate and temperature on the stress strain response of solder alloys, Journal of Materials Science: Materials in Electronics, 10, pp 4 6 1- 4 6 8, 1999.

Qi, H., Ganesan, A., Osterman, M., Pecht, M., Accelerated testing and finite element analysis of PBGA under multiple environmental loadings, Proceedings of IEEE International Conference of Business Electronics Product Reliability, pp. 99–106, Apr. 2004.

Qin, F., An, T., Chen, N., Strain Rate Effects and Rate-Dependent Constitutive Models of Lead-Based and Lead- Free Solders, Journal of Applied Mechanics, Vol. 77 / 011008-1, Jan, 2010.

Ramberg, W., Osgood, W., Description of Stress-Strain curves by three parameters, NACA Technical Note No. 902, 1943.

Rodgers, B., Flood., Punch, J., Waldron, F., Experimental Determination and Finite Model Validation of the Anand Viscoplasticity Model Constants for SnAgCu, 6th Int. Conf. on the thermal, Mechanical and Ohysics Simulation and Experiments in Micro-Electronics and Micro- Systems, EuroSimE, 2005.

Siviour, C., R., Walley, S., M., Proud, W., G., Field, J., E., Mechanical properties of Sn-Pb and Lead-free Solder at High Rates of Strain, Journal of Physics D: Applied Physics 38, 4131-4139, 2005.

Srinivasan, V., Radhakrishnan, S., Zhang1, X., Subbarayan, G., Baughn, T., Nguyen, L., High Resolution Characterization of Material used in Packages through Digital Image Correlation, Proceedings of IPACK2005, ASME InterPACK 2005, June 17-22, 2005.

Srinivasan, V., Radhakrishnan, S., Zhang, X., Subbarayan, G., Baughn, T., Nguyen, L., High Resolution Characterization of Materials Used In Packages through Digital Image Correlation, ASME InterPACK, July 17-22, 2005.

Steinberg, D., Vibration Analysis for Electronic Equipment, Wiley (New York, 1988).

Suh, D., Kim, D., Liu, P., Kim, H., Weninger, J., A., Kumar, C., M., Prasad, a., Grimsley, B., W., Tejada., H., B., Effects of Ag content on fracture resistance of Sn–Ag– Cu lead-free solders under high-strain rate conditions, Materials Science and Engineering A 460–461, pp.595–603, 2007.

Tang, C., Y., Fan, J., P., Lee, T., C., Journal of Materials Processing Technology 139, pp. 510–513, 2003.

Tavernelli, J., Coffin, Jr. L., Experimental Support for Generalized Equation Predicting Low Cycle Fatigue, ASME Journal of Basic Engineering, Volume 84, pp. 533–541, Dec 1962.

Tee, T. Y. , Hun Shen Ng, Chwee Teck Lim, Eric Pek, Zhaowei Zhong, Board Level Drop Test and Simulation of TFBGA Packages for Telecommunication Applications, Proceedings of the 53rd ECTC, pp. 121-129, 2003.

Tiwari, V., Williams, S., Sutton, M., McNeill, S. Application of Digital Image Correlation in ImpactTesting, Proceedings of the 2005 SEM Annual Conference and Exposition on Experimental and Applied Mechanics, June 7-9, 2005.

Upadhyayula, V.,K.,K., and Dasgupta, A., An Incremental Damage Superposition Approach for Reliability of Electronic Interconnects Under Combined Acceleration Stresses, ASME International Mechanical Engineering Congress & Exposition, Dallas, Texas, Nov., 1997.

Villain, J., Mueller, W., Saeed, U., Weippert, C., Corradi, U., Svetly, A., Mechanical Behavior of SAC-Lead Free Solder Alloys with Regard to the Size Effect and the Crystal Orientation, 10th European Microelectronics Packaging Conference, , pp. 587-590, June 2009

Wang., T. H., Lai, Y., Submodeling analysis for path dependent thermomechanical problems Tiwari, V., Williams, S., Sutton, M., McNeill, S. Application of Digital Image Correlation in Impact Testing, Proceedings of the 2005 SEM Annual Conference and Exposition on Experimental and Applied Mechanics, June 7-9, 2005.

Wilde, J., Becker, K., Thoben, M., Blum, W., Jupitz, T., Guozhong, W., Cheng, Z., N., Applying Anand Model to Represent the Viscoplastic Deformation Behavior of Solder Alloys, IEEE Transaction on Advanced Packaging, Vol.23, No.3,Aug 2000.
Wong, E. H., Lim, C. T., Field, J. E., Tan, V. B. C., Shim, V. P.M., Lim, K. T., Seah, S. K. W., Tackling the Drop Impact Reliability of Electronic Packaging, ASME InterPAK, July 6 -11, Maui, pp. 1 – 9, 2003.

Wong, S., Malatkar, P., Rick, C., Kulkarni, V., Chin, I., 2007, Vibration Testing and Analysis of Ball Grid Array Package Solder Joints, Proceedings of the 57th ECTC, Reno, Nevada, pp. 914-923, May 29 –June 1, 2007a.

Wong, E., H., Selvanayagam, C., S., She, S., K, W., Van Driel, W., D., Caers, J., Zhao, X., J., owens, N., Tan, L., C., Frear, D., R., Leoni, M., Lai, Y., Stress Strain Characteristics of Tin-Based Solder Alloys for Drop-Impact Modeling, Journal of Electronic Materials, Vol. 37, No. 6, 2008.

Wong, T., Kachatorian, A., Cohen, M., 1997, J-Lead Solder Thermal Fatigue Life Model, ASME International Mechanical Engineering Congress & Exposition, Dallas, Texas, Nov. 1997.

Xiao, Q., Nguyen, L., and Armstrong, W. D., Aging and Creep Behavior of Sn3.9Ag0.6Cu Solder Alloy, Proceedings of 54th Electronic Components and Technology Conference, pp. 1325-1332, 2004.

Yeo, A., Lee, C., Pang, J., H., L., Flip Chip Solder Joint Reliability Analysis Using Viscoplastic and Elastic-Plastic-Creep Constitutive Models, IEEE Transactions on Components and Packaging Technologies, Vol. 29, No. 2, June 2006.

Yu D., Al-Yafawi A., Nguyen T., Park S., Chung S., High-cycle fatigue life prediction for Pb-free BGA under random vibration loading, Microelectronics Reliability 51 (2011) 649-656

Zhang, B., Liu, P., Ding, H., Cao, W., Modeling of board-level package by Finite Element Analysis and laser interferometer measurements, Microelectronics Reliability 50 (2010) 1021-1027

Zhao, Y., Basaran, C., Cartwright, A., Dishongh, T., An experimental observation of thermomechanical behavior of BGA solder joints by Moir’e Interferometry, Journal of Mechanical Behavior of Materials, Volume 10, No.3, pp. 135-146, 1999.

Zhou, P., Goodson, K. E., Sub-pixel Displacement and Deformation Gradient Measurement Using Digital Image- Speckle Correlation (DISC), Optical Engineering, Vol. 40, No. 8, pp 1613-1620, August 2001.